The Pennsylvania State University

The Graduate School

Department of Mechanical & Nuclear Engineering

FUNDAMENTAL MODELING THE PERFORMANCE AND DEGRADATION OF HEV LI-ION BATTERY

A Dissertation in

Mechanical Engineering

by

Weifeng Fang

Submitted in Partial Fulfillment
of the Requirements
for the Degree of

Doctor of Philosophy

August 2010

The dissertation of Weifeng Fang was reviewed and approved* by the following:

Chao-Yang Wang
Professor of Mechanical Engineering
Professor of Material Science & Engineering
Dissertation Advisor
Chair of Committee

Long-Qing Chen
Professor of Material Science & Engineering

Fan-Bill Cheung
Professor of Mechanical & Nuclear Engineering

Christopher D. Rahn
Professor of Mechanical & Nuclear Engineering

Karen Thole
Professor of Mechanical & Nuclear Engineering
Head of the Department of Mechanical and Nuclear Engineering

*Signatures are on file in the Graduate School

ABSTRACT

Li-ion battery is now replacing nickel-metal hydride (NiMH) for hybrid electric vehicles (HEV). The advantages of Li-ion battery over NiMH are that it can provide longer life, higher cell voltage and higher energy density, etc. However, there are still some issues unsolved for Li-ion battery to fully satisfy the HEV requirement. At high temperature, thermal runaway may cause safety issues. At low temperature, however, its performance is dramatically reduced and also Li deposition may occur. Furthermore, degradation due to side reactions in the electrodes during cycling and storage results in capacity loss and impedance rise.

An electrochemical-thermal coupled model is first used to predict performance of individual electrodes of Li-ion cells under HEV conditions that encompass a wide range of ambient temperatures. The model is validated against experimental data of not only the full cell but also individual electrodes and then used to study lithium deposition on the negative electrode during charging Li-ion battery at subzero temperature. The simulated property evolution, e.g. Li concentrations in electrode and electrolyte, shows that either low temperature or high charge rate may force Li insertion (into the negative carbon electrode) to occur in a narrow region near the separator. Therefore, Li deposition is mostly like to happen in this location. Modeling simulation shows that reduction of the negative electrode particle size can reduce Li deposition, which has same effect as improvement of the Li diffusion coefficient in the negative electrode. The model is also used to study charge protocols at subzero temperature. Model simulation shows that employing pulse current can improve cell temperature by the heat generated inside the

cell, thus this designed charge protocol is able to reduce Li deposition and improve the charge efficiency as well.

Individual aging mechanism is then implemented into each electrode to study Li-ion battery degradation during accelerated aging tests. The experimentally observed aging phenomena are interpreted using the degradation model. The simulated results show that the positive electrode active material loss is the main cause of capacity loss and impedance growth. And this is the key step for a model to well catch the experimentally observed aging phenomena in the two electrodes.

In the future work, the degradation model will further help to prolong battery life through engineering and optimization in HEV applications.

TABLE OF CONTENTS

LIST OF FIGURES

LIST OF TABLES

ACKNOWLEDGEMENTS

I would like to express my deepest gratitude to my advisor, Dr. Chao-Yang Wang, for his excellent guidance, caring, patience and providing me with an excellent atmosphere for doing research. I would also like to thank my other committee members, Dr. Long-Qing Chen, Dr. Fan-Bill Cheung and Dr. Christopher D. Rahn for their service on my doctoral committee and for their suggestions and insightful comments on my dissertation work.

My thanks go out to my co-worker at ECEC, Ou Jung Kwon and Dr. Yancheng Zhang for providing numerous experimental data for this dissertation. I also thank all the other members at ECEC for their help.

Finally, I would like to thank my family and all others who were not mentioned above and have given me all kinds of support and help during my time here at Penn State.

Chapter 1

Introduction

Since it was commercialized in 1991 by Sony, the Li-ion battery has been widely accepted and developed in many application areas: cell phones, laptops and other portable electric instruments. The key to its success lies in the fact that it has higher energy density and higher power density compared to other batteries such as Lead-Acid and nickel-metal hydride (NiMH) batteries (see Table **1.1**).

There are several reasons to seek more clean energy to partly replace combustion-engine vehicles. HEV, using batteries in conjunction with a small, fuel-efficient engine is already commercialized. Whereas consumer electronics may require the batteries to last for only several years, HEV batteries are required to keep high capacity and power for 15 years—which are just the weakness of current Li-ion batteries (See Fig. **1.1**). Nevertheless, Li-ion batteries are now replacing NiMH batteries to be used in the HEVs, for Li-ion battery technology is expected to offer a 40-50% battery weight reduction and a 20-30% battery volume reduction as well as some margin of efficiency improvement [**2**]. It is thus very urgent that the Li-ion battery aging problems are soon resolved; this requires both experimental and computer modeling efforts to understand the degradation mechanisms and to establish a life prediction so that the calendar life of Li-ion battery can be improved.

In this chapter, we will briefly introduce the working principles of a Li-ion battery and the materials currently most used and studied, followed by more detailed discussion

of aging mechanisms and computer modeling efforts. Based on which, a Li-ion battery degradation model will be introduced later in this present work.

1.1 Basic Principle of a Li-Ion Battery

A basic Li-ion battery consists of negative electrode and positive electrode (or anode and cathode, respectively, although by a more strict definition, this convention is only correct during discharge, where the anode is the electrode where electrons leave the cell and an oxidation-reaction occurs while the cathode is where a reduction-reaction takes place.), which are separated by a separator. The electrolyte acts as an electronic insulator but a good ionic conductor which provides a transport-medium for Li-ions to travel from one electrode to another while keeps the electrons in the external circuit.

Take a cell with a graphite anode and a $LiCoO_2$ cathode for example, during a charge process, Li-ions de-insert from $Li_{1-x}CoO_2$ solid particles, and travel through the electrolyte solution to intercalate[1] into Li_xC_6. Electrons are forced to follow an opposite path through an external circuit. During a discharge process, Li-ions and electrons then travel in reverse. These kinds of batteries are thus called Li-ion (rechargeable) batteries—with lithium ion shuttling between the cathode and the anode hosts during the charge-discharge processes, which can be described by the electrode reactions:

Eq. **1.1** for cathode

---

[1] In Chemistry, intercalation is used to describe the process of inserting a guest atom or ion into a planar crystalline host without losing the structural integrity of the host like graphite, any other Li storage process without significant layered structure is considered as insertion.[3]

$$LiCoO_2 \underset{\text{discharge}}{\overset{\text{charge}}{\rightleftharpoons}} Li_{1-x}CoO_2 + xLi^+ + xe^- \quad (1.1)$$

and Eq. **1.2** for anode

$$C_6 + xLi^+ + xe^- \underset{\text{discharge}}{\overset{\text{charge}}{\rightleftharpoons}} Li_xC_6 \quad (1.2)$$

Carbon (such as graphite and coke) having light weight and low electrode potential of less than 1 V versus Li/Li^+ has become an attractive anode material. It has a theoretical capacity of 372Ah/kg, which corresponds to an insertion of one lithium per 6 carbon atoms ($x = 1$ in Li_xC_6). On the cathode side, $LiCoO_2$, $LiNiO_2$ and $LiMn_2O_4$ oxides having a high electrode potential of 4V versus Li/Li^+, have become the materials of choice for cathode in the present generation of Li-ion cells. See extensive review of insertion electrode materials for Li-ion batteries in Ref. [**4**].

Besides the insertion electrode materials, the electrolyte is also important in designing a good Li-ion battery that can offer high performance with long cycle life. The working voltage for Li-ion cells (in the range of 2.5-4.5 V) requires an electrolyte having a wide electrochemical stability window. Only a few non-aqueous alternatives (including solid, liquid and polymeric electrolytes) are among the choices; liquid electrolytes are most commonly exploited so far because of their superior ionic conductivity at ambient temperature [**5**].

The commonly used electrolytes in Li-ion batteries are solvent mixtures of alkyl carbonates together with a lithium salt. Ethylene carbonate (EC) [**6**], dimethy carbonate (DMC) [**7**], diethyl carbonate (DEC) [**8**], ethylmethyl carbonate (EMC) [**9**] and methyl propylene carbonate (MPC) [**10**] are among the choices of solvents. EC is the preferred

solvent but is solid at room temperature, therefore EC is often mixed with other solvents such as DMC and DEC to obtain a working electrolyte over a wider temperature interval.

Lithium hexafuorophosphate, $LiPF_6$, is the most commonly used salt in studies and in commercial cells. It has good anodic stability and high ionic conductivities in alky carbonates solutions. It shows excellent cycling properties at room temperature, but poor cycling behavior for some electrode materials at elevated temperature. A pronounced disadvantage of $LiPF_6$ solutions is that when $LiPF_6$ decomposes into LiF, high resistive LiF surface films form on the electrode, increasing the electrode's impedance [11].

To find a replacement for the currently used alkyl carbonate solvents and $LiPF_6$ is difficult, and it is much easier to use functional additives that improve the electrodes' interfaces and enhance conductivity. Alkyl nitrates, sulfates and phosphonates were suggested as passivation-improving additives whose presence reduces the irreversible capacity of Li-C anodes [3].

1.2 Literature Review of Li-Ion Battery Degradation: Experimental Efforts

The Li-ion cell model describing degradation processes is undoubtedly a powerful tool for battery design and engineering for HEV applications. In addition, degradation battery models help to evaluate aging mechanisms under normal driving and accelerated test conditions as well as to identify key parameters controlling battery cycle life and viable solutions through fast and cost-effective computer simulations.

According to Ref.[12], the major processes causing capacity fade and impedance growth in Li-ion cells are very complicated and may include passive film formation over electrode surfaces, lithium deposition under overcharge conditions, electrolyte decomposition, etc. To design a Li-ion battery that is both efficient and economical while running under optimized and safe conditions relies on these degradation processes being understood quantitatively. To date, most existing Li-ion models consider only the BOL behavior of systems which are unable to address safety and cycle life issues critical for HEV applications.

For batteries to be applied in hybrid and pure electric vehicles, a goal of 15 years has been set for automakers. As commercial Li-ion batteries are only 16 years old, and are still evolving rapidly, there are no data available on the capacity and power fade of Li-ion batteries over such an extended period. Nor is it practical to carry out real-time testing of batteries to qualify them for automotive applications. Thus, there is interest in developing accelerated test methods as well as computer models based on a physicochemical understanding of the causes of aging. At the same time, the long actual aging process also requires such models to simulate an entire life cycle, however in a much shorter time. This means the basic model should be very robust, fast, and accurate while incorporating requisite degradation events. These goals promote establishing a Li-ion cycle life predictor that considers the effects of long-term operation and predicts the capacity and power fade over cycling. Such a model can then be used to reveal viable engineering and optimization solutions to prolong battery life. For practical application, the models should be fast enough to show an advantage over experiments.

1.2.1 Li-Ion Battery Degradation Processes

To study and identify major degradation processes is the first and key step to develop a Li-ion battery degradation model. An early significant review of Li-ion battery degradation processes was presented by Arora and co-workers [12]. Side reactions, as the major causes of capacity fade and impedance growth, were discussed in detail therein. Based on this review and other work [13,14,15], a selection of degradation processes at both electrodes is shown in Table 1.2 with the details to be discussed in the following subsections. Here, unless pointed out otherwise, carbon (such as graphite and coke) is used as the anode material and typical lithium metal oxide (such as $LiCoO_2$, $LiNiO_2$ and $LiMn_2O_4$) is used as the cathode material.

Capacity loss, reversible or irreversible, is often due to the loss of active materials either by consumption or isolation from cycle. Impedance growth, causing power fade, is often the result of resistive surface layer growing on the electrodes.

1.2.2 Degradation at Negative Electrode

SEI film- During the first charge of a fresh Li-ion cell, a passivated SEI film forms due to the irreversible reaction between lithium ions and solvent at the surface of the carbon electrode. The fundamental process involved has been explained by Peled et al. [17-21] and discussed by many others. Most of the capacity loss in the early stage results from active lithium consumption during this process; however, ideally, if a stable,

protective SEI film is formed, the electrode is then isolated from the electrolyte, reducing the chance of further electrolyte components reduction.

A good SEI film must: (i) permit free Li^+ transport, i.e. t_{Li}=1; (ii) prohibit electron transport, i.e. t_e=0, in order to avoid SEI thickening; and (iii) withstand the volume change due to Li^+ intercalation-deintercalation between the graphene layers. The other properties such as high conductivity (to reduce overpotential) and good adhesion to the anode are also favored [22]. Good electrolyte systems, according to some experiments, for SEI film formation include electrolyte solutions based on EC-DMC and EC-DEC [13,21-24].

Practically, the transference number for unsolvated Li-ion may not be the unity ($t_{Li}\neq1$) and it may also allow other charged (anions, electrons, solvated cations) and neutral (solvents, impurities) species to diffuse/migrate through. Upon prolonged charge-discharge cycling, the slight volume changes in graphite during Li intercalation leads to the breakdown and repair of the surface films, causing capacity loss (due to lithium consumption) and increasing the electrode impedance (due to SEI film thickening) [23,24]. Fig. 1.2 (adopted from Ref.[14]) shows the complex SEI film formation and development at the carbonaceous electrode.

Several steps may be involved in the formation and development of SEI film. The film formed in the first cycle has a thickness of several tens of nanometers [24,25] and increases to several micrometers of thickness during cycling or storage [26-30]. A complex two-layer multicomponent structure of SEI film was proposed by Peled et al. [22] where the inner layer is rich in Li_2O and LiF and low in Li_2CO_3 and the outer layer

consists of 13% Li_2CO_3 and other semicarbonates, 10% LiF, with the remainder being polyolefins.

Elevated or low temperatures impact SEI film in different ways. The morphology and composition of SEI film is believed to change under elevated temperatures [31-34]. As a result, the SEI film starts to break or dissolve while the degradation rate of the SEI film rises. It is also possible that the metastable organic components of SEI may be converted to more stable inorganic products, reducing its ionic conductivity for lithium [35-36]. Low temperatures, however, may enhance metallic lithium plating and lithium dendrite growth during charge, incurring reactions of the lithium metal with the electrolyte that accelerate aging and may also deteriorate safety [14].

Lithium deposition under overcharged condition- When the negative electrode is overcharged, another form of lithium deposition may occur which causes the consumption of active lithium when the highly reactive metallic lithium covering the active surface of negative electrode reacts with the solvent or salt molecules producing Li_2CO_3, LiF or others [24,37,38].

1.2.3 Degradation at Positive Electrode

Degradation processes at the positive electrode vary with different cathode materials used. Hence they may be very specific to cathode materials and the results or developed models should be used with extra caution. Generally, there are three basic

principles causing capacity fade of the cathode: (*i*) structural changes during cycling, (*ii*) chemical decomposition/dissolution reaction, and (*iii*) surface film modification [14].

Positive electrode structure changes during the insertion/de-insertion of lithium ions may induce mechanical stress and strain to the oxide particles. Phase transitions can also occur, leading to distortion of the crystal lattice and further mechanical stress.

Surface film is also observed in positive electrode, which may have a different structure with the surface film formed on graphite; Li ions have to take extra effort to migrate through this film during insertion/deinsertion of the electrode compounds [39]. The initial major component of this film is Li_2CO_3 and is replaced by solution-related surface species such as ROLi, $ROCO_2Li$, polycarbonates, and salt-reduction products, upon storage in solutions [40].

As nickel-based oxide is the cathode material for the degradation model developed in this research, the following sub-section is focused on the related surface phenomena on the electrode made of this material.

1.2.4 Surface Film on Nickel Oxide- Based Cathode

As a promising substitute for commercialized $LiCoO_2$, lithium nickel oxide-based materials meet the low-impedance criteria required to meet the high-power requirements for HEV applications, and their high capacity and medium cost make them more attractive, however, their cycle performance and thermal stability need to be further improved [30,41,42].

The lithium nickel-based oxide particles are known to have a thin surface $Li_xNi_{1-x}O$ or NiO-type layer, which has different electronic and ionic properties from the bulk oxide [**43**]. Abraham et al. showed that a thickening of NiO-type layer forming on the lithium nickel cobalt oxide electrode surface during cell aging could significantly hamper Li-ion charge transfer characteristics of the oxide particles and cause power fade [**44**,**45**]. Fig. **1.3** (adopted from Ref. [**44**]) nicely shows the different structures of this surface layer with the bulk oxide.

Dees et al. further observed on the top of this NiO-type layer, an ill-defined mixture of organic and inorganic material surface film, which is formed by interaction of the oxide particle with the electrolyte and combined with the polymer binder; lithium ions from the electrolyte must either diffuse or migrate, or both through this film to react electrochemically at the surface of the oxide [**46**].

This hypothesis was further explained by Dubarry et al. in their recent studies on a $LiNi_{0.8}Co_{0.15}Al_{0.05}O_2$-based 18650 cell. They stated that both capacity fade and peak power capability fade of the cell are related to the cathode associated with two phenomena: (i) the growth of very thin NiO-type surface composition on cathode active material, and (ii) the formation of a film layer on the surface of active material particles causing the lost contact with some carbon black [**47**]. A discussion of the relation and interaction of these two phenomena was also provided therein.

Recently, Zhang et al. found that the decomposition products of electrolytes (EC and/or DMC) on the $LiNi_{0.8}Co_{0.2}O_2$ electrode surface are mainly carboxylate salts RCO^{2-} [**48**]. They hypothesized that at a high potential, Ni^{4+} is formed significantly on a bare,

highly deinserted state $Li_xNi_{0.8}Co_{0.2}O_2$ surface and these Ni4+ must oxidize the electrolyte.

In addition, thermal stability and heat generation of lithium nickel oxide-based electrode has also been extensively studied [49-58]. Typically, structure change of $LiNi_{0.8}Co_{0.15}Al_{0.05}O_2$ composite positive electrode under elevated temperatures may cause deterioration of its electrochemical performance and increase its thermal instability. A study on laboratory-size $LiNi_{0.8}Co_{0.15}Al_{0.05}O_2$/graphite Li-ion pouch cells cycled over 100% DOD (depth of discharge, the level to which the battery is discharged in reference to the initial discharge capacity—20% DOD means 20% of battery capacity has been removed) showed that about 65% of the initial capacity was lost after 140 cycles at 60°C while cycling capacity at 25°C was essentially constant and most of the capacity loss was due to a low-ionic-conductivity surface film layer forming on the cathode at the high temperature [57].

1.2.5 Other Degradation Processes

Other degradation processes include electrolyte decomposition, self discharge, and degradation at the current collectors.

Common electrolytes in use today decompose at high voltages (>4.5 V). Gas generation and insoluble product (Li_2CO_3, etc.) formation during electrolyte decomposition not only cause capacity loss but also can be an extreme safety hazard by blocking the pores of the electrodes [24,38]. More discussion can be found in Ref. [59].

Upon storage, the spontaneous cell voltage drop under open-circuit is known as self discharge. Most capacity loss from self discharge can be recovered during the subsequent cycling. Irreversible losses are mostly caused by the consumption of active lithium (to form products such as LiF and Li_2CO_3 [60,61]) or the physical blockage of active electrode surface [12].

The most commonly used current collectors for negative and positive electrodes are copper and aluminum, respectively. Passive film formation, adhesion, and localized corrosion are the main issues related to current collectors during cycling, and increase the internal impedance of the cell, possibly causing capacity and power fade [12].

1.3 Literature Review of Li-Ion Battery Degradation: Modeling Efforts

1.3.1 Overview of Li-Ion Degradation Models

The first attempt was made by Darling and Newman, who incorporated a side reaction—solvent oxidation at the positive electrode—into a Li-ion battery model [62]. The parasitic reaction was simplified with Tafel kinetics and the model then was used to simulate the self-discharge process and charge-discharge cycles; the results were analyzed by comparing with experimental data.

Arora *et al*. then proposed a mathematical model to study the lithium deposition on carbon-based anode under overcharge condition [37].

Later, a simulation was carried out by Christensen and Newman [63] to study the influence of the anode film on the cell charge/discharge performance. They concluded that the use of cutoff potential—with the intention of preventing adverse side reactions (such as lithium deposition)—did not achieve the purpose. They also found incomplete cell charge and discharge occurred resulting from the increased anode film resistance and charge/discharge rate, with the charge process suffering more. Subsequently, they identified that film growth at the negative electrode is faster for charged batteries than for uncharged batteries and that higher electron mobility in the film leads to faster film growth [64]. In a recent paper they pointed out that preforming the negative electrode (by forming an SEI on the active material before assembling the cell), adding cycable lithium to the positive electrode and introducing lithium powders into the negative electrode appear to be the most attractive methods to preserve the battery's specific energy [65].

Recently, a fundamental model was developed by Ramadass, et al. to be used as a basis for predicting the cycle life and analyzing the discharge characteristics of Li-ion cells after any given cycle number [66]. The model is based on the main assumption that the entire capacity loss was due to the parasitic reaction of solvent reduction over the surface of negative electrode during charge. Following that, capacity fade models based on similar assumptions were developed by Ning et al. [67,68] to complete the work by adding the discharge process and carrying out further parametric studies.

Other modeling work includes those of Spotnitz's model [69] and Sikha et al. [70]. The Spotniz model includes an expression for SEI growth to predict effect of capacity loss at the negative electrode and the Sikha model considers the effect of porosity on the capacity fade, which was ignored in other degradation models.

In addition, there are also empirical or semi-empirical approaches developed for predicting capacity and/or power fade [71-78]. By fitting the experimental data into Li-ion insertion models or some expressions, empirical correlations were then identified for some key parameters such as state of charge (SOC), film resistance, and their changes—with which the total capacity and/or power fade could be estimated. It should be noted that all empirical models have a range of validity as limited by the experimental data used.

Compared to the empirical approaches, incorporating parasitic reactions into a fundamental Li-ion battery model is more advantageous and offers more insight for battery design and application to HEVs. Among these, the models in Ref. [66-70] simulating the SEI formation and continuous electrolyte decomposition for normal voltage range (the first two degradation processes in Table 1.2). The models developed by Christensen et al. [63-65] studied SEI film properties in detail. The model in Ref. [37] focused on lithium deposition under overcharge condition, and the work in Ref. [62] investigated the influence on current-potential behavior of the electrodes due to positive electrode side reactions. In the following subsections, we will focus on a degradation model falling in the category of "Electrochemistry-Transport Models" which utilize a general Li-ion battery model with incorporation of side reactions [37,62-70]. These models are able to validate, evaluate and predict the cell aging problems through parametric studies. The object of this research is to understand the intrinsic aging mechanisms of Li-ion batteries as well as to efficiently predict the battery's cycle life, which can only be achieved by a fundamental electrochemistry-transport model.

1.3.2 An Electrochemistry-Transport Model for Degradation

Base model selection- The majority of electrochemistry-transport models published in the literature are variants of Newman's macro-homogeneous model [79,80] or Wang's micro-macroscopic model based on the theory of volume averaging [81-83]; these models are general enough to describe a wide range of porous electrode and electrolyte materials. Moreover, the Wang group's model, as implemented by a general computational fluid dynamics (CFD) technique, is not limited to one dimension and can account automatically for thermal effects. Therefore, this micro-macroscopic modeling framework is chosen as the base model for extension to describe degradation processes in Li-ion cells.

Side reactions- Almost all of the existing electrochemistry-transport coupled models for degradation consider side reactions taking place only at one electrode and attributed all the capacity loss and impedance growth to surface film formed on this electrode; in most cases, surface phenomena on the positive electrode, were ignored for simplicity and other reasons such as the lack of separate experimental data necessary for each electrode.

Steps of incorporating side reactions- A common method of incorporating side reactions is to calculate the active lithium consumed by the side reactions, which is often done by integrating the local side reaction rates over the reaction time. The resistance of the insoluble side reaction product is often calculated in proportion to the film thickness which increases due to deposit of side reaction product. And at the beginning of each discharge/charge cycle, several parameters such as lithium concentration, film resistance,

and SOC of the considered electrode are updated. The model in Ref. [66] further recalculated the SOC of the other electrode, considering that the active lithium loss affects each electrode by the same amount. Additional parameters, i.e. the active surface area, porosity and diffusion coefficient, are also updated in the Sikha model [70].

In some models [66,70], the solvent reduction reaction is assumed to occur at the anode and only during charge—by assuming that breaking of the limited flexible surface film and thus exposing more of the underlying carbon to the electrolyte is more prominent for Li-ion insertion [13].

To simplify the rate of side reactions, either a Tafel or linear approximation to the Butler-Volmer rate expression may be used, while the former assumes the side reactions are highly irreversible (as in Ref. [66,67,68]), and the later assumes that the surface overpotentials are sufficiently low [37].

Identification of key material parameters- The open-circuit potential or equilibrium potential for a side reaction is among the key parameters that need to be carefully identified. Based on experimental results [13,84,85], the value, 0.4 V vs. Li/Li^+, is widely adopted for the side reactions of electrolyte reduction at the anode [66,67,70] and 3.8V vs. Li/Li^+ is used for electrolyte oxidation at the cathode [62].

If possible, important material parameters should be obtained directly through separate experiments, otherwise the best values can be fitted based on other experimental data as many degradation models did.

Parametric studies- The effects of EOCV (end of charge voltage) and DOD (depth of discharge) have been studied in Ref. [66,67,68]. The conclusion was that high EOCV (high DOD, as well) causes more capacity loss and results in higher film resistance

because capacity loss and film resistance rise are proportional to side reaction time in those models.

Lithium deposition during overcharge was studied in Ref. [37]. The simulated results indicate that by increasing anode capacity and decreasing cutoff voltage, lithium deposition can be greatly reduced.

Comparison of simulated and experimental results- The majority of the existing electrochemistry-transport models for Li-ion battery degradation may predict general trends of capacity and power fade, however, few of the simulated results have been compared to experimental data quantitatively [62,68]. For better understanding the aging mechanisms as well as improving the modeling reliability, more quantitative and extensive comparisons with experimental data are needed.

In addition, degradation models have not been applied to study accelerated aging mechanisms under elevated temperatures.

1.4 Object of Our Degradation Model

Extensive experimental research has been carried out to understand the aging mechanisms of Li-ion batteries. It is generally thought—but not necessary correct everywhere—that capacity loss is mostly attributed to loss of active lithium at the negative due to the formation of SEI film, and impedance growth is attributed to both electrodes, but predominantly to the positive electrode due to the highly resistive surface film.

Computer modeling has already been employed to help understand the aging mechanisms for about 10 years, nevertheless, there are only few degradation models in the open literature, mainly due to the complicated nature of aging mechanisms, and especially due to a limited understanding of aging at the cathode with various materials used. Among these few degradation models, some are empirical or semi-empirical which may be useful for predicting the capacity/power fade for specific batteries, but provide little understanding of intrinsic aging mechanisms. On the contrary, most of the electrochemistry-transport coupled models lack rigorous validation by experimental data or specific studies of cell aging in HEV applications. Additionally, accelerated aging protocols under elevated temperatures and/or high charge/discharge rates, while effective and widely used in experimental studies of aging mechanisms, have yet to be scrutinized and interpreted in the context of degradation models.

Based on the micro-macroscopic modeling framework developed by Wang et al. [**81**], a host of battery models has been developed by our group for various HEV applications [**82**,**83**,**86**,**87**,**88**]. In particular, the recently developed Li-ion model [**89**,**90**] is well suited for HEV batteries that often work under high-rate transient power cycled about a relatively fixed SOC. Hence, we propose to expand the current Li-ion charge/discharge thermal-electrochemical coupled model to include degradation processes. The objectives of our degradation model include:

- To model degradation processes in each electrode based on the current experimental understanding under both ambient temperature and elevated temperature. To our knowledge, none of the existing degradation models

includes degradation processes in both electrodes or distinguishes each electrode's contribution to capacity loss or impedance growth.

- To determine the parameters with and to validate the model against the parallel experimental data collected.
- To perform complete and detailed parametric studies to identify key parameters that control Li-ion battery cycle life in HEV applications.
- To develop ultrafast algorithms to enable sufficiently rapid computations of cycle life prediction, showing the advantage of computer simulation over experiments.

Eventually, such an extended model will form a cycle-life predictor for capacity and power fade and enable prolonged battery life through engineering and optimization.

1.5 Overview of the Present Work

In particular, electrochemical-thermal coupled phenomena in Li-ion batteries must be captured, as they control major technological hurdles of current interest, such as thermal runaway at high temperatures, much reduced performance at subzero temperatures, and Li deposition in the anode and capacity loss under high-rate, low-temperature charging. To date, both experimental and modeling research on thermal and electrochemical characteristics is mostly limited to full Li-ion cells. For example, early models of Li-ion cells were developed by Newman and co-workers using porous electrode and concentrated solution theories [79,80,91] under isothermal and one-

dimensional assumptions. Subsequently Wang and coworkers have focused on electrochemical-thermal coupled modeling for Li-ion batteries, especially for automotive applications[**81**,**82**,**89**,**90**,**92**]. Model validation was performed against experimental data of full cells only.

Stringent automotive application, however, calls for detailed diagnostics and modeling of not only the full cell, but also individual electrodes such that anode and cathode contributions to both performance and degradation can be separately delineated and predicted. For example, lithium deposition on the negative electrode in overcharge or low temperature situations and degradation of a Li-ion battery due to surface film formation on both electrodes all require a good understanding of individual electrode behaviors in addition to a full cell.

So that in this present dissertation,

A general, electrochemical-thermal coupled model is introduced in Chapter 2. This model is then validated with experimental data not only the full cell, but also individual electrodes in Chapter 3.

In chapter 4, the validated model is used to study lithium deposition on the negative electrode in overcharge or subzero temperature situations. The possible charge strategy under subzero temperature is also discussed.

In Chapter 5, the performance model is extended to include degradation of a Li-ion battery due to surface film formation on both electrodes. This degradation model is then used to interpret the aging phenomena observed by the accompany experiment. (The experiment was carried out by Kwon.)

In Chapter 6, summary of this present work is made and some future work is discussed.

Table **1.1**: Comparison of primary and secondary battery systems (Adopted from Dr. Wang's lecture for ME597D, the Penn State University)

Battery	***Specific energy (Wh/kg) Theoretical/practical***	***Specific power (W/kg) (80%DOD)***
Alkaline (Zn/MnO)	336/50-80	N/A
Lead-Acid	170/35	220
Ni-Cd	209/50	N/A
Ni-MH	380/60	150
Li-ion	**500-550/150**	**350**

Table 1.2: Main degradation processes of Li-ion cells

Degradation process	*consequences*	*Enhanced by*	*Typical reactions*
Negative electrode:			
SEI forms due to electrolyte reduction during first charge	Irreversible capacity loss; Gas generation		$EC + 2e^- \rightarrow \text{ethylene} + CO_3^{2-}$ [16]
Continuous electrolyte decomposition	Capacity fade (loss of lithium); Impedance growth	High temperature; High SOC	
Lithium deposition	Capacity fade; Impedance growth	Overcharge; High charge rate	$Li^+ + e^- = Li(s)$ [24]
Positive electrode:			
Structural disordering; Phase transitions	Capacity fade		$LiNiO_2 \leftrightarrow \{Li_{1-x}Ni(II)_{x/2}\}Ni(III)_{1-x}\}O_{2-x} + \frac{x}{2}Li_2O + \frac{x}{4}O_2$ [14]
Surface film formation	Capacity fade; Impedance growth		$EC + LiNiO_2 \rightarrow NiO_2 - CH_2CH_2OCO_2Li$ [40]
Others:			
Electrolyte oxidation at positive electrode	Capacity fade; Impedance growth	Overcharge; High temperature	solvent $\rightarrow$ oxidized products (gases, solution, and solid species) + ne^- [12]
Self-discharge on positive oxidized electrode	Reversible and irreversible capacity loss	High temperature	$El \rightarrow e^- + El^+$ $yLi^+ + ye^- + MO_z \rightarrow Li_yMO_z$ * [6]
Current collector degradation	Capacity fade; Impedance growth	Overdischarge	

* El = EC, PC, etc.; M = Ni, Co, Mn, etc.

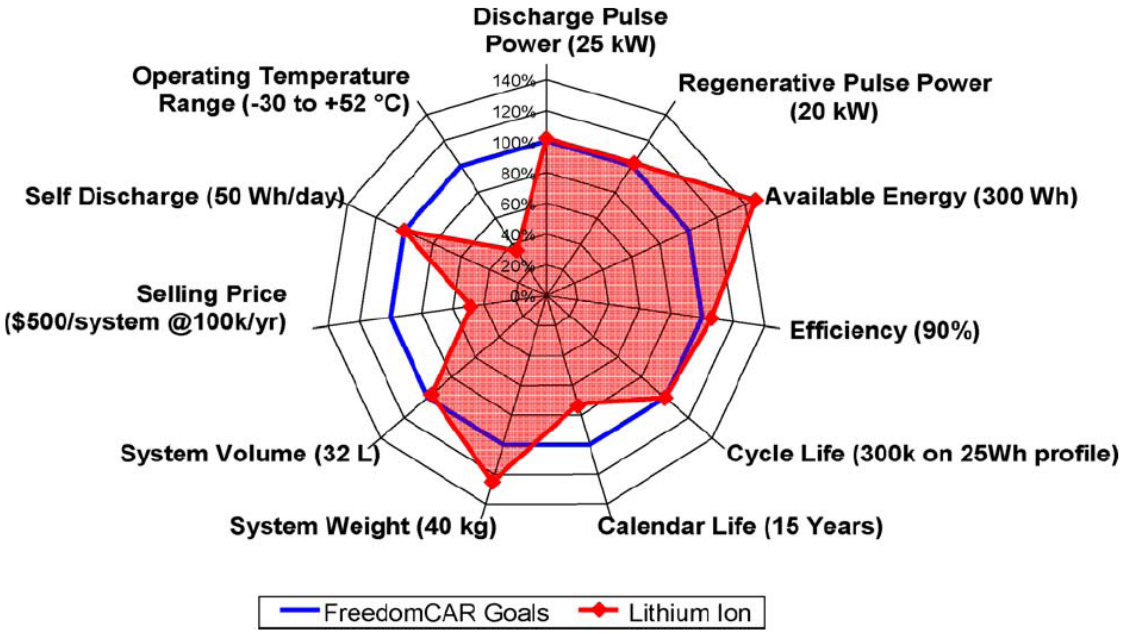

Figure 1.1: Spider chart showing status of advanced Li-ion battery system development compared to the energy storage goals for minimum power-assist HEVs set up by FreedomCAR[2]. It shows, calendar life, operating temperature range, and selling price goals are currently major challenges. [1]

[2] FreedomCAR is a USA national program developing more energy efficient and environmentally friendly highway transportation technologies that will enable America to use less petroleum (cited from Wiki website)

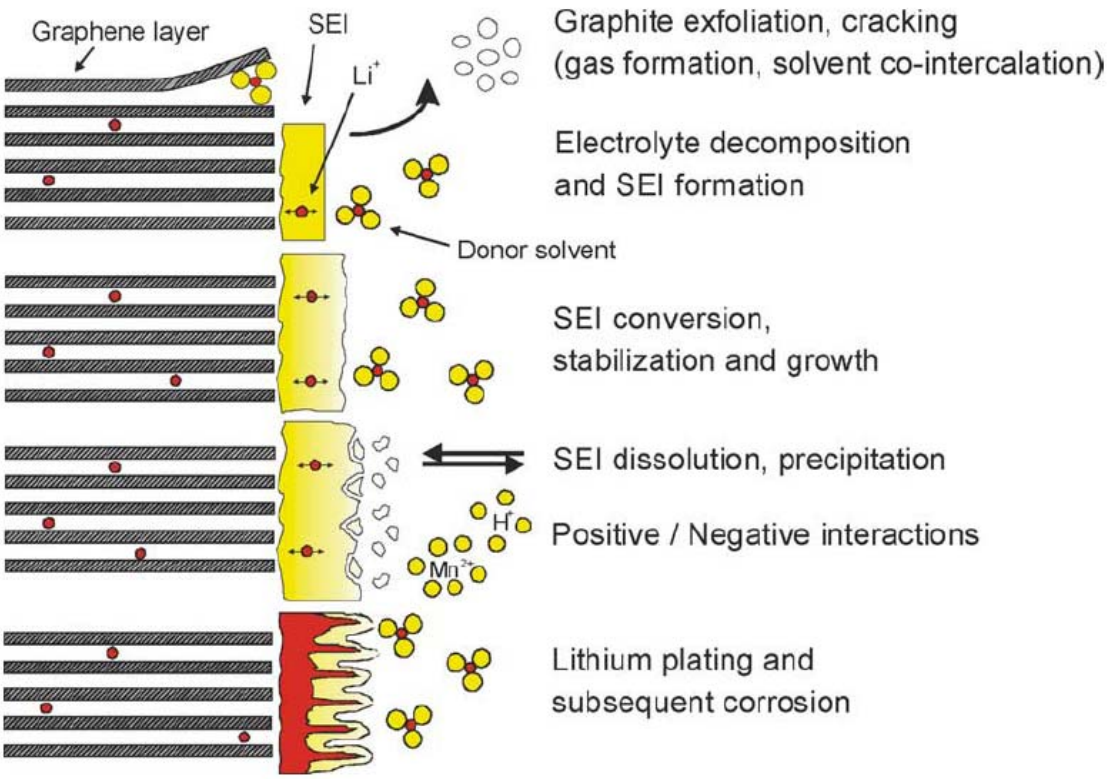

Figure 1.2: The complex intercalation and SEI formation process at anode/electrolyte interface [14].

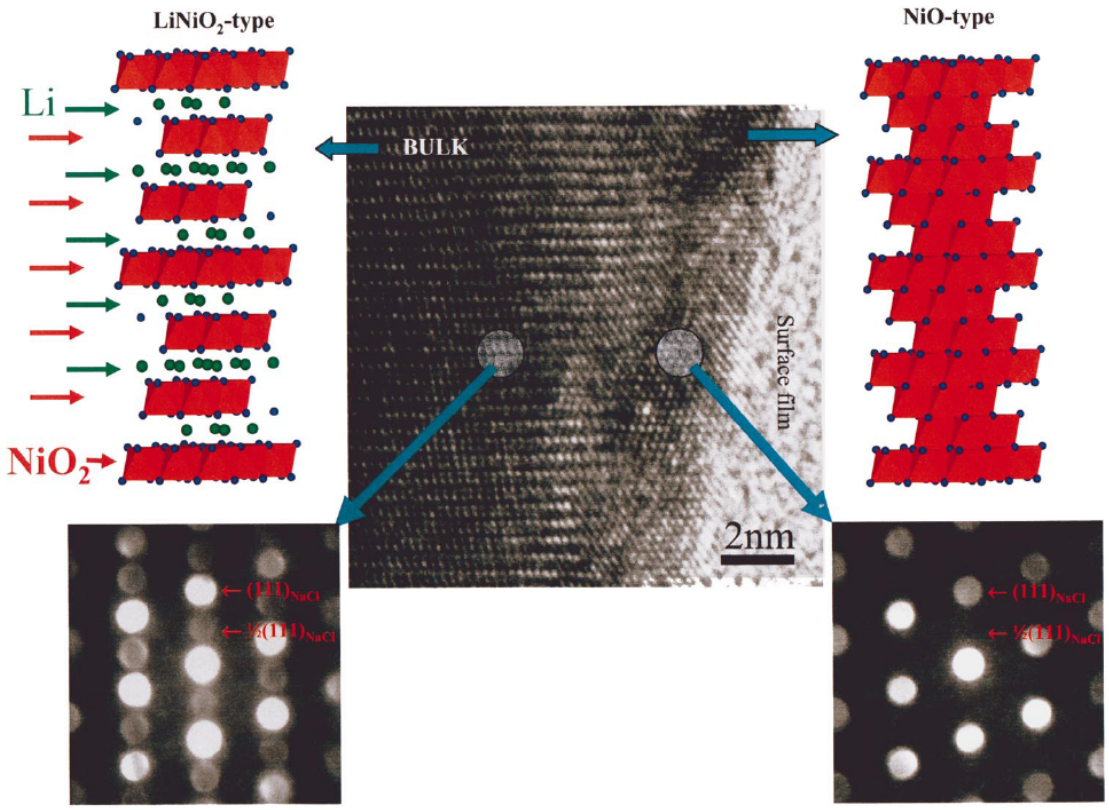

Figure 1.3: The crystal structure difference between the bulk and surface of $LiNi_{0.8}Co_{0.2}O_2$ particles, illustrated by HREM (high resolution electron microscopy) image, convergent beam electron diffraction patterns, and structure schematics [44].

Chapter 2

An Electrochemical-Thermal Performance Model for Automotive Li-Ion Batteries

The electrochemical-thermal (ECT) model for Li-ion cells introduced in this chapter is based on concentrated solution theory [79,80] and volume averaging theory [81,86]. The model was initially developed by Gu and Wang to account for solid-state diffusion, and further expanded by them to include the energy equation [81-83,86-88]. Recently, Smith and Wang [89,90] formulated an approximate solution method for the diffusion of lithium ions within active material particles using the finite element method and implemented it as an explicit difference equation into the model based on the above Gu's model.

As the first step to develop a Li-ion battery degradation model for HEV applications, the Smith's 1D model is implemented into a general-purpose CFD package (such as STAR-CD and Fluent) in order to access complex discharge and charge profiles experienced in automobile application. Furthermore, simulation results are validated against extensive experimental data characteristic of automobile application for cell at the beginning of life (BOL). In this chapter, the governing equations of the Li-ion model will be briefly outlined. The experiment validation using three-electrode cell will be presented in the next chapter.

In Chapter 4, the performance model will be used to study the impact of ECT coupling on subzero temperature performance of automobile Li-ion batteries. And then

the degradation model based on the performance model will be introduced and studies on the cell degradation under accelerated aging test will be carried out in Chapter 5.

2.1 Thermal-Electrochemical Coupled Li-Ion Cell Model

A schematic diagram of a Li-ion cell 1D model is shown in Fig. **2.1**. Three domains are considered: anode (graphite), separator, and cathode (lithium metal oxide).

The basic assumptions of the proposed transient CFD model are listed below:

1. No gas phase is present.
2. Concentrated binary electrolyte is assumed [**79**,**93**].
3. Charge transfer kinetics follows Butler-Volmer equation.
4. Ionic species transport in the electrolyte is by migration and diffusion only.
5. The active electrode materials are made up of spherical particles of uniform size.
6. Volume change during cell operation is neglected, resulting in constant electrode porosities.
7. The transport of lithium inside the solid active material particles is by diffusion with constant diffusion coefficient.
8. The entire cell is assumed to have temperature spatially uniform but varying with time.

Thermal coupling is important because some key degradation processes are temperature-sensitive, such as lithium deposition and electrolyte decomposition in the

negative electrode, electrolyte oxidation and self-discharge in the positive electrode, as shown in Table **1.2** . This is also necessary since we are going to apply the model to examine low performance at low temperature and degradation under accelerated conditions at elevated temperatures.

Porous electrode theory is adopted in modeling the composite electrodes consisting of active material and electrolyte solution. The solid and electrolyte phases are treated as superimposed continua with each phase having its own volume fraction, while the microstructure of each phase is not considered. Therefore, the material balances should be averaged in a volume large enough to treat electrochemical reaction as a homogeneous term but small compared to the overall dimension of the electrode. For tortuosity effect, electrolyte diffusion coefficient and ionic conductivity are corrected using Bruggeman relationships, $D_e^{eff} = D_e \varepsilon_e^{\tau}$ and $\kappa^{eff} = \kappa\, \varepsilon_e^{\tau}$, respectively, where τ is the Bruggeman exponent. And electronic conductivity is corrected as $\sigma^{eff} = \sigma \varepsilon_s^{\tau}$, for each electrode. Here, ε_e and ε_s are electrolyte and solid phase volume fractions, respectively.

An electrochemical and thermal coupled Li-ion battery model can be derived with the above assumptions. The final governing equations are summarized and listed in Table **2.1**, and will be briefly discussed in this section. For more details about general modeling approach, please refer to Ref. [**79**,**81**-**83**].

Among all the governing equations, Eq. **2.2**, Eq. **2.7**, Eq. **2.10**, and Eq. **2.13**, are the processes occurring at a macroscopic level in the *x*-direction, across the negative electrode/separator/positive electrode, while Eq. **2.11** describes the phenomena occurring at a microscopic level in the *r*-direction (See Fig. **2.1**). The macroscopic diffusion and

migration of lithium ions in the electrolyte phase is described by conservation of species in the liquid phase, Eq. **2.10**. The solid phase diffusion of Li, Eq. **2.11**, within spherical Li_xC_6 and metal oxide active material particles (whose radii are on the order of 1 μm) is classified as a microscopic phenomenon. This type of combined micro&macroscopic model is sometimes called a pseudo 2D model.

At the macroscopic level, concentrated solution theory is adopted to present the relationship between driving forces (such as gradients in chemical potential) and mass flux [**94**]. For the charge balance, Ohm's law is applied to describe the potential drop across the electrode, while it is modified in the electrolyte to also include the diffusion potential.

2.1.1 Charge Conservation Equations

From the simple Ohm's law, the current in solid phase, i_s, is related to the potential in solid phase, ϕ_s, as

$$i_s = \sigma^{eff} \frac{\partial}{\partial x} \phi_s \qquad (2.1)$$

Eq. **2.1**

Through the electrode, due to the insertion and de-insertion reactions at the electrode/electrolyte interface, the current in solid phase changes as follows

Eq. **2.2**

$$\frac{\partial}{\partial x}\left(\sigma^{eff}\frac{\partial}{\partial x}\phi_s\right)=j^{Li} \qquad (2.2)$$

Reaction rates for insertion and de-insertion reactions are generally assumed to follow the Butler-Volmer equation [91],

Eq. 2.3

$$\bar{i}_n = i_o\left\{\exp\left[\frac{\alpha_a F}{RT}\left(\eta-\bar{i}_n R_{SEI}\right)\right]-\exp\left[-\frac{\alpha_c F}{RT}\left(\eta-\bar{i}_n R_{SEI}\right)\right]\right\} \qquad (2.3)$$

where α_a and α_c are the anodic and cathodic transfer coefficients of electrode reactions, respectively and R_{SEI} is a constant SEI layer resistance adopted in the performance model. The exchange current density, i_o, is a function of lithium concentrations in both electrolyte and solid active material phases, i.e.

Eq. 2.4

$$i_o = k(c_e)^{\alpha_a}(c_{s,\max}-\bar{c}_{se})^{\alpha_a}(\bar{c}_{se})^{\alpha_c} \qquad (2.4)$$

where c_e and c_s are the volume-averaged lithium concentration in the electrolyte and solid phases respectively; $\bar{c}_{se}$ is the area-averaged solid-state lithium concentration at the electrode/electrolyte interface, and $c_{s,\max}$ is the maximum concentration of lithium in the solid phase. The constant, k, is determined by the initial exchange current density and species concentrations. The local surface overpotential, η, is defined as the difference between the solid and liquid phase potential with respect to the open-circuit potential (OCP), U, or

Eq. 2.5

$$\eta = \phi_s - \phi_e - U \tag{2.5}$$

The OCP is a function of local SOC and temperature. A linear function of temperature, $U = U\big|_{T_{ref}} + (T - T_{ref})\dfrac{\partial U}{\partial T}$ is usually used for approximation. In the present work, the correlations based on experimental data are used.

Thus, the transfer current, j^{Li}, resulting from the lithium insertion or de-insertion reaction at the electrode/electrolyte, can be expressed as

Eq. **2.6**

$$j^{Li} = \begin{cases} a_{s,a}\bar{i}_{n,a} \\ 0 \\ a_{s,c}\bar{i}_{n,c} \end{cases} \tag{2.6}$$

where $a_{s,a}$ and $a_{s,c}$ are the specific interfacial area of an electrode, with subscript *a* and *c* representing the anode and the cathode, respectively.

Conservation of charge in the electrolyte, in a modified form of Ohm's law, is

Eq. **2.7**

$$\frac{\partial}{\partial x}\left(\kappa^{eff}\frac{\partial}{\partial x}\phi_e\right) + \frac{\partial}{\partial x}\left(\kappa_D^{eff}\frac{\partial}{\partial x}\ln c_e\right) = -j^{Li} \tag{2.7}$$

In the equation, the diffusional conductivity, κ_D^{eff}, is described by concentrated solution theory [**80**], as

Eq. **2.8**

$$\kappa_D^{eff} = \frac{2RT\kappa^{eff}}{F}(t_+^o - 1)\left(1 + \frac{d\ln f_{\pm}}{d\ln c_e}\right) \tag{2.8}$$

where $f_{\pm}$ is the mean molar activity coefficient of the electrolyte and a constant value is assumed in this work due to a lack of experimental data. The electrolyte conductivity, κ, strongly depends on the electrolyte composition. For the electrolyte consisting of $LiPF_6$ in a 2:1 v/v mixture of ethylene carbonate (EC) and dimethyl carbonate (DMC), it has value [91],

Eq. 2.9

$$\kappa = 4.1253\times10^{-4} + 5.007c_e - 4.7212\times10^{3}c_e^2 + 1.5094\times10^{6}c_e^3 - 1.6018\times10^{8}c_e^4 \quad (2.9)$$

2.1.2 Species Conservation Equations

The transport processes in the electrolytic phase is treated by the concentrated solution theory. Based on the assumption that the electrolyte is binary with a single organic solvent, a material balance on the lithium ion in the electrolyte is

Eq. 2.10

$$\frac{\partial(\varepsilon_e c_e)}{\partial t} = \frac{\partial}{\partial x}\left(D_e^{eff}\frac{\partial}{\partial x}c_e\right) + \frac{1-t_+^o}{F}j^{Li} \quad (2.10)$$

where t_+^o is the transference number of the Li^+ with respect to the velocity of solvent. Depending on the combination of electrolyte and solvent, it can be a function of the electrolyte concentration. A constant value of the transference number of lithium ion is assumed in this work [91].

At the microscopic level, the active material is assumed to be made up of spherical particles with diffusion being the mechanism of transport of the lithium into the particle. Conservation of lithium in the solid phase of both electrodes is described by

Eq. **2.11**

$$\frac{\partial c_s}{\partial t} = \frac{1}{r^2}\frac{\partial}{\partial r}\left(D_s r^2 \frac{\partial c_s}{\partial r} \right) \tag{2.11}$$

The model can also simulate cylindrical and planar particles; the treatment is analogous. For an electrode composed of spherical particles of radius R_s, the initial specific surface area is given by

Eq. **2.12**

$$a_s = \frac{3\varepsilon_s}{R_s} \tag{2.12}$$

where ε_s is the volume fraction of solid phase. Corresponding formula should be used to calculate this specific surface area if cylindrical or planar particle is assumed. For modeling of irregularly shaped particles however, it is proposed to directly base the micro-macroscopic model on the measured specific surface area because its inverse is a more accurate representation of the length scale of a complex micro-macro structure than the average particle sizes [**81**].

In generally, decreasing the particle size while keeping the porosity results in high surface area which usually gives higher rate capability and higher utilization. However, it should be noted that small particle would make it difficult to bind the particles together and hence may result in greater ohmic drops because of poor contact. In addition, smaller particle size electrodes would increase the use of carbon to coat the particles, resulting in

a decrease in the tape density, therefore the decrease of the cell volumetric energy density. These issues indicate that it should be careful to make a recommendation on the optimum particle size.

While uniform particle size is adopted in most models, the particle sizes may have a distribution in real electrode. The model study in this paper [**95**] shows that the performance of an electrode with two-particle distribution is worse than that of the electrode with uniform particle at the average size because the larger particles will give rise to transport limitations.

2.1.3 Thermal Energy Conservation Equation

For a Li-ion cell with lumped thermal capacity accumulation assumption, the conservation equation is [**90**],

Eq. **2.13**

$$\frac{d\left(\rho c_p T\right)}{dt} = \left[hA_s\left(T_\infty - T\right) + \left(q_r + q_j + q_c\right)\right]/(A \cdot L) \qquad (2.13)$$

where, h is the convective heat transfer coefficient and A_s is the cell surface area exposed to the cooling medium with free steam temperature, T_∞. The total reaction heat, q_r, is calculated by integrating the local volume-specific reaction heat (equals reaction current, j^{Li}, times overpotential, η) across the 1D domain and multiplied by plate area, A, or

Eq. **2.14**

$$q_r = \int_0^L j^{Li}\left(\phi_s - \phi_e - U\right) dx \qquad (2.14)$$

Note that no reaction heat is generated in the separator where there is no reaction, and the joule heat,

Eq. 2.15

$$q_j = A\int_0^L \sigma^{eff}\left(\frac{\partial \phi_s}{\partial x}\right)^2 + \kappa^{eff}\left(\frac{\partial \phi_e}{\partial x}\right)^2 + \kappa_D^{eff}\left(\frac{\partial \ln c_e}{\partial x}\right)\left(\frac{\partial \phi_e}{\partial x}\right) dx \qquad (2.15)$$

results from the joule heating in the solid active material (the first term on RHS) and electrolyte phases (the rest).

Additional joule heat arises from a contact resistance between current collector and electrodes. It is calculated as

Eq. 2.16

$$q_c = I^2 \frac{R_f}{A} \qquad (2.16)$$

2.1.4 Thermal and Electrochemical Coupling

To couple the thermal model with the multiphase mass transport and electrochemical model, temperature-dependent physicochemical properties, such as the diffusion coefficient and ionic conductivity of electrolyte, are needed, and the dependence can be described by the Arrhenius' equation [86,96],

Eq. 2.17

$$\Phi = \Phi_{ref} \exp\left[\frac{E_{act,\Phi}}{R}\left(\frac{1}{T_{ref}} - \frac{1}{T}\right)\right] \quad (2.17)$$

where Φ is a general variable representing the diffusion coefficient of a species, conductivity of the electrolyte, exchange current density of an electrode reaction, etc., with subscript *ref* denoting the value at a reference temperature. $E_{act,\Phi}$, the activation energy of the evolution process of Φ, whose magnitude determines the sensitivity of Φ to temperature.

In simulation, the cell temperature is calculated by thermal energy conservation equation, Eq. **2.13**, based on the heat generation due to electrochemical reactions and joule heating. This temperature information is, in turn, fed back to update the electrochemical calculations through temperature-dependent physicochemical properties. The thermal and electrochemical behaviors of a battery are thus fully coupled.

2.2 Numerical Procedure

2.2.1 Summary of Governing Equations

A total of five governing equations (Eq. **2.2**, Eq. **2.7**, Eq. **2.10**, Eq. **2.11**, and Eq. **2.13**) can be solved for the five unknowns: ϕ_s, ϕ_e, c_e, c_s, and T. Fig. **2.2** shows the flow chat of the numerical procedure. The dependent variables of concentration, potential, reaction rate, and current density each appears in more than one governing equation and

therefore the governing equations should be solved simultaneously. The commercial software StarCD or Fluent is used to solve these equations except for the solid phase conservation equation, Eq. **2.11**, about which is discussed as follows.

Several solution methods, both exact and approximate [**81**,**97**,**98**], are used to calculate the solid surface concentration, c_{se}, as a function of the time history of reaction current, j^{Li}. The method adopted in this work is the approximation developed in Ref. [**89**,**90**] using a finite element discretization consisting of five unevenly spaced elements which provides sufficient resolution for the application in HEV battery simulation. The computational requirements of the method are minimized by discretizing the system of ODEs with respect to time and expressing the solution in explicit form as a difference equation. For each macroscopic (*x*-direction) finite control volume, the algorithm stores in memory the previous values of reaction current density, j^{Li}, and solid phase surface concentration, c_{se}. A new value of c_{se} is calculated explicitly using the previous time step values plus the current value of j^{Li}.

2.2.2 Initial and Boundary Conditions

Initial conditions: Uniform initial conditions are assumed, i.e.

Eq. **2.18**

$$c_e = c_e^o,\ c_s = c_s^o \text{ and } T = T^o \qquad (2.18)$$

Boundary conditions: The electrolyte is confined within the cell and no reaction occurs at the end of the cell, giving rise to (See Fig. **2.1** for definition of L, L_-, L_{sep}, L_+, etc.)

Eq. **2.19**

$$\left.\frac{\partial c_e}{\partial x}\right|_{x=0,L} = 0 \text{ and } \left.\frac{\partial \phi_e}{\partial x}\right|_{x=0,L} = 0 \tag{2.19}$$

Other boundary conditions include

Eq. **2.20**

$$\begin{gathered} -\sigma_-^{eff}\left.\frac{\partial \phi_s}{\partial x}\right|_{x=0} = \sigma_+^{eff}\left.\frac{\partial \phi_s}{\partial x}\right|_{x=L} = \frac{I}{A}, \\ \left.\frac{\partial \phi_s}{\partial x}\right|_{x=L_-} = \left.\frac{\partial \phi_s}{\partial x}\right|_{x=L_-+L_{sep}} = 0 \end{gathered} \tag{2.20}$$

while in simulation, a reference value is assigned to ϕ_s at x = 0 to keep the solution unique. And

Eq. **2.21**

$$\left.\frac{\partial c_s}{\partial r}\right|_{r=0} = 0 \text{ and } -D_s\left.\frac{\partial c_s}{\partial r}\right|_{r=R_s} = \frac{j^{Li}}{a_s F} \tag{2.21}$$

where the first boundary condition stipulates that the solid-phase concentrations are finite at the origin and the second relates the local reaction rate to the flux across the particle surface.

2.2.3 Model Parameters

Commercial 1.2 Ah 18650 cells with a graphite anode and a nickel-manganese-cobalt oxide (NMC) cathode as well as the electrolyte of 1.2M LiPF6 in EC/DMC are used in all experiments of Kwon [101]. Most of the parameters used in the code for the following studies from Chapter 3 to Chapter 5 are listed in Table 2.2, which is for a cell at the BOL. These parameters are either directly measured or best estimates based on the information available.

The geometry of the meshing system is shown in Fig. 2.5. The open-circuit potentials for the electrodes are shown in Fig. 2.3. The cell terminal voltage is determined by the equation:

Eq. 2.22

$$V_{cell} = \phi_s\big|_{x=L} - \phi_s\big|_{x=0} - \frac{R_c}{A} I \qquad (2.22)$$

where R_c is the resistance of electrode/current collector interface. Here, I is positive when discharged and negative when charged. Fig. 2.4 clearly shows the relationship of V_{cell} and the electrode potentials during charge and discharge.

2.3 Conservation Check of the Performance Model

As a first check of the model, conservation of current density, electrolyte and solid concentration, and energy are checked under 1C charge/discharge conditions. The simulated results satisfy all the conservation laws perfectly with errors less than 1%.

C-rate is often used to measure the charge and discharge current of a battery, i.e. 1C denotes a one-hour charge/discharge. For example, a 1.2Ah battery would provide 1.2A for one hour discharge at 1C rate. The same battery discharged at 2C would provide 2.4A for half an hour, theoretically.

2.4 Summary

The performance model introduced in this chapter is based on the framework consisting of porous electrode theory, concentrated solution theory, Ohm's law, kinetic relationships, and material, charge, and energy balances. Macroscopic conservation equations are derived separately for the electrode, separator and electrolyte using the volume averaging technique. Here, the interfacial terms are contained to allow for the incorporation of microscopic physical phenomena such as solid state diffusion and ohmic drop. A finite element scheme is used to link the macroscopic model with microscopic Li^+ transport in active material particles.

A full validation of the performance model will be carried out in the next chapter.

Table **2.1**: Governing equations for an HEV Li-ion cell model

	Conservation Equations:	***Boundary Conditions***:
Charge, Electrode	$\frac{\partial}{\partial x}\left(\sigma^{eff}\frac{\partial}{\partial x}\phi_s\right)=j^{Li}$	$-\sigma_{-}^{eff}\left.\frac{\partial\phi_s}{\partial x}\right\|_{x=0}=\sigma_{+}^{eff}\left.\frac{\partial\phi_s}{\partial x}\right\|_{x=L}=\frac{I}{A},$ $\left.\frac{\partial\phi_s}{\partial x}\right\|_{x=L_-}=\left.\frac{\partial\phi_s}{\partial x}\right\|_{x=L_-+L_{sep}}=0$
Charge, Electrolyte	$\frac{\partial}{\partial x}\left(\kappa^{eff}\frac{\partial}{\partial x}\phi_e\right)+\frac{\partial}{\partial x}\left(\kappa_D^{eff}\frac{\partial}{\partial x}\ln c_e\right)=-j^{Li}$	$\left.\frac{\partial\phi_e}{\partial x}\right\|_{x=0}=\left.\frac{\partial\phi_e}{\partial x}\right\|_{x=L}=0$
Species, Electrolyte	$\frac{\partial(\varepsilon_e c_e)}{\partial t}=\frac{\partial}{\partial x}\left(D_e^{eff}\frac{\partial}{\partial x}c_e\right)+\frac{1-t_+^o}{F}j$	$\left.\frac{\partial c_e}{\partial x}\right\|_{x=0}=\left.\frac{\partial c_e}{\partial x}\right\|_{x=L}=0$
Species, Solid Phase	$\frac{\partial c_s}{\partial t}=\frac{1}{r^2}\frac{\partial}{\partial r}\left(D_s r^2\frac{\partial c_s}{\partial r}\right)$	$\left.\frac{\partial c_s}{\partial r}\right\|_{r=0}=0,$ $-D_s\left.\frac{\partial c_s}{\partial r}\right\|_{r=R_s}=\frac{j^{Li}}{a_s F}$
Heat Generation	$\frac{d(\rho c_p T)}{dt}=hA_s(T-T_\infty)+(q_r+q_j+q_c)A$	

Table 2.2: Model input parameters for an 1.2 Ah Li-ion cell

Quantity	Symbol	Value
Cell Operating Limits		
Lower cut-off voltage, V	V_{min}	3.0
Upper cut-off voltage, V	V_{max}	4.1
Active Material & Electrolyte Chemical Concentrations		
Stoichiometry, x, of Li_xC_6 at full discharge ($x = c_{sa}/c_{sa,max}$)	$x_{0\% soc}$	0.073
Stoichiometry, x, of Li_xC_6 at full charge ($x = c_{sa}/c_{sa,max}$)	$x_{100\% soc}$	0.692
Stoichiometry, x, of Cathode at full discharge ($y = c_{sc}/c_{sc,max}$)	$y_{0\% soc}$	0.9
Stoichiometry, x, of Cathode at full charge ($y = c_{sc}/c_{sc,max}$)	$y_{0\% soc}$	0.328
Maximum concentration of Li in Li_xC_6, mol/cm^3	$c_{sa,\max}$	0.0309
Maximum concentration of Li in Cathode, mol/cm^3	$c_{sc,\max}$	0.0495
Average concentration of Li^+ in electrolyte, mol/cm^3	c_e^0	1.2e-3
Cell Geometry & Volume Fraction Design Specifications		
Thickness of negative electrode, cm	L_-	40e-4
Thickness of separator, cm	L_{sep}	25e-4
Thickness of positive electrode, cm	L_+	35e-4
Porosity of Li_xC_6 electrode	ε_a	0.59
Porosity of separator (plasticized electrolyte)	ε_s	0.42
Porosity of Cathode	ε_c	0.54
Volume fraction of polymer phase in Li_xC_6 electrode	$\varepsilon_{a,p}$	0.0
Volume fractions of conductive filler in Li_xC_6 electrode	$\varepsilon_{a,f}$	0
Volume fraction of polymer phase in the separator	$\varepsilon_{s,p}$	0.58
Volume fraction of polymer phase in Cathode	$\varepsilon_{c,p}$	0.0
Volume fractions of conductive filler in Cathode	$\varepsilon_{c,f}$	0.0
Radius of Li_xC_6 intercalation material, cm	$R_{s,a}$	5.5e-4
Radius of Cathode intercalation material, cm	$R_{s,c}$	4.0e-4
Cell density, Kg/cm^3	$\rho_{s,a}$	5.0e-3

Electrochemical Kinetic and Transport Properties		
Initial exchange current density at Li_xC_6 electrode, A/cm^2	$i_{0,a}$	3.6e-3
Initial exchange current density at Cathode, A/cm^2	$i_{0,c}$	2.6e-3
Transfer coefficients (anodic) at Li_xC_6 electrode	α_{a1}	0.5
Transfer coefficients (cathodic) at Li_xC_6 electrode	α_{c1}	0.5
Transfer coefficients (anodic) at Cathode	α_{a2}	0.5
Transfer coefficients (cathodic) at Cathode	α_{c2}	0.5
Conductivity of Li_xC_6 electrode, S/cm	σ_a	1
Conductivity of Cathode, S/cm	$\sigma_{,c}$	0.1
Diffusion coefficient of Li in Li_xC_6 solid particles, cm^2/s	$D_{s,a}$	2.25e-10 $(1.5\text{-}x)^{3.5}$
Diffusion coefficient of Li^+ in electrolyte solution, cm^2/s	D_e	1.5e-6
Diffusion coefficient of Li in Cathode solid particles, cm^2/s	$D_{s,c}$	2e-10
Bruggeman tortuosity exponent for electrolyte diffusion (anode)	τ_a	1.5
Bruggeman tortuosity exponent for electrolyte diffusion (cathode)	τ_c	1.5
Bruggeman tortuosity exponent for electrolyte diffusion in separator	τ_s	1.5
Electrolyte activity coefficient in anode, separator and cathode	$f_{\pm}$	1.0
Li+ transference number in anode, separator and cathode	t_+^0	0.367
Double layer capacity, F/cm^2	C_{dl}	20e-6
SEI resistance, Ohm cm^2	R_{SEI}	0
Contact resistance, Ohm cm^2	R_f	20
Electrode plate area, cm^2	A	970
Temperature Dependence of Physio-chemical Properties		
Reference cell temperatures, K	T_{ref}	298.15
Activation energy for exchange current densities, J/mol	E_{act,i_0}	30e3
Activation energy for diffusion coefficient of Li in Li_xC_6 solid particles, J/mol	$E_{act,D_{s,a}}$	4e3

Activation energy for diffusion coefficient of Li in Cathode solid particles, J/mol	$E_{act,D_{s,c}}$	2e4
Activation energy for diffusion coefficient of Li^+ in electrolyte solution, J/mol	E_{act,D_e}	1e4
Activation energy for ionic conductivity of electrolyte, J/mol	$E_{act,k}$	2e4
Thermal Model Parameters		
Initial temperature of cell, K	T_0	298.15
Ambient temperature, K	T_{amb}	298.15
Specific heat of cell, J/kgK	$c_{p,sa}$	1e3
dU/dT at Li_xC_6 electrode, V/K		0
dU/dT at Cathodes, V/K		0

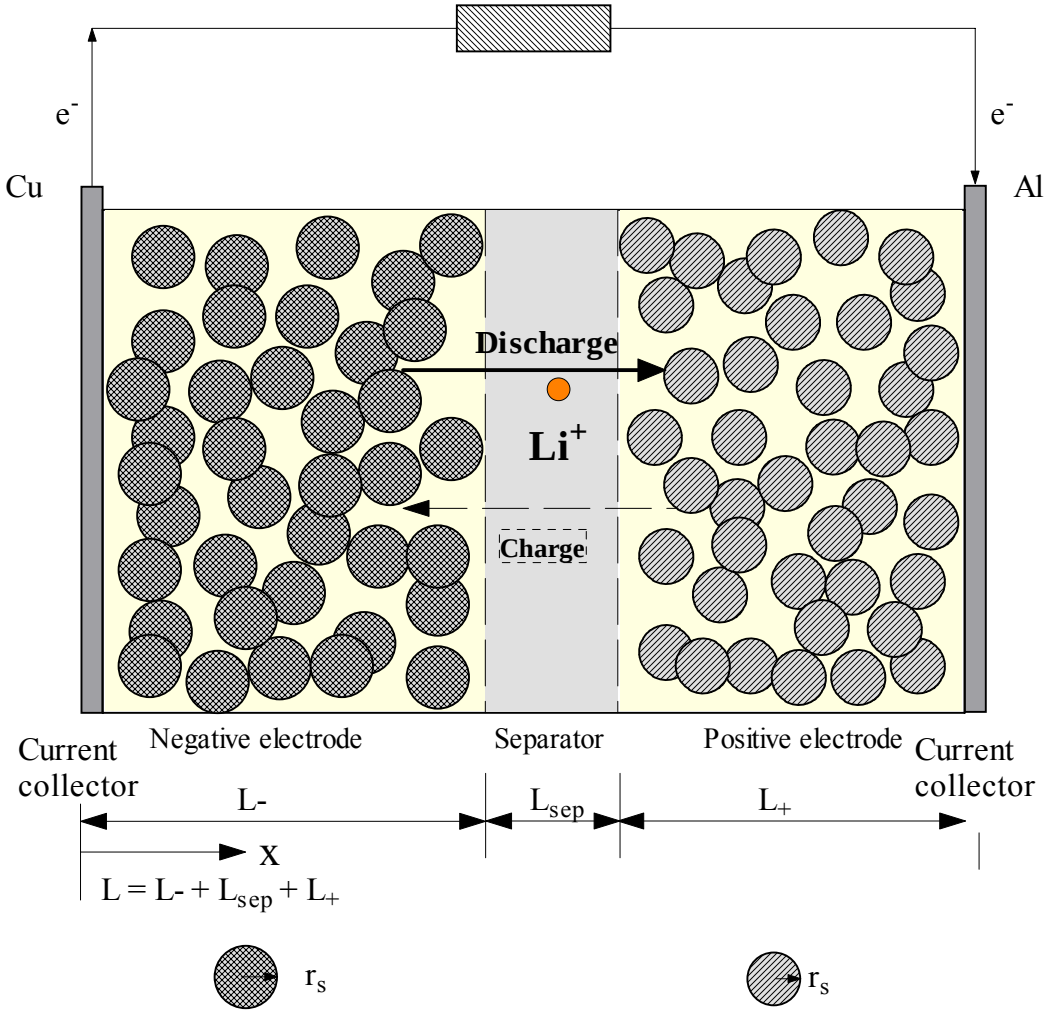

Figure 2.1: Schematic representation of a pseudo 2D Li-ion cell model.

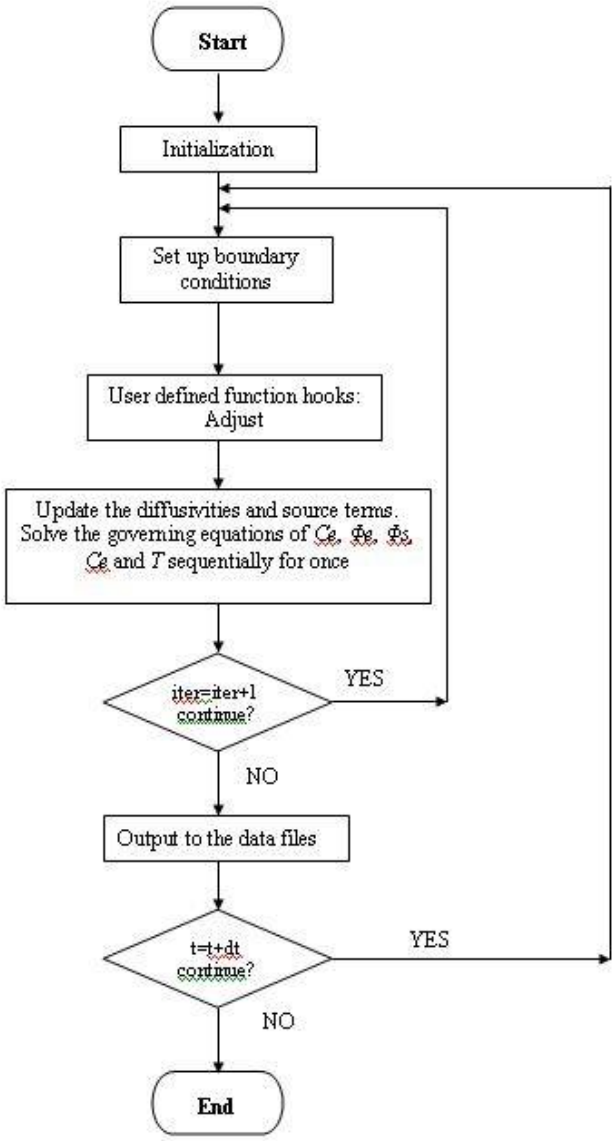

Figure 2.2: Flow chat of the numerical procedure.

Figure 2.3

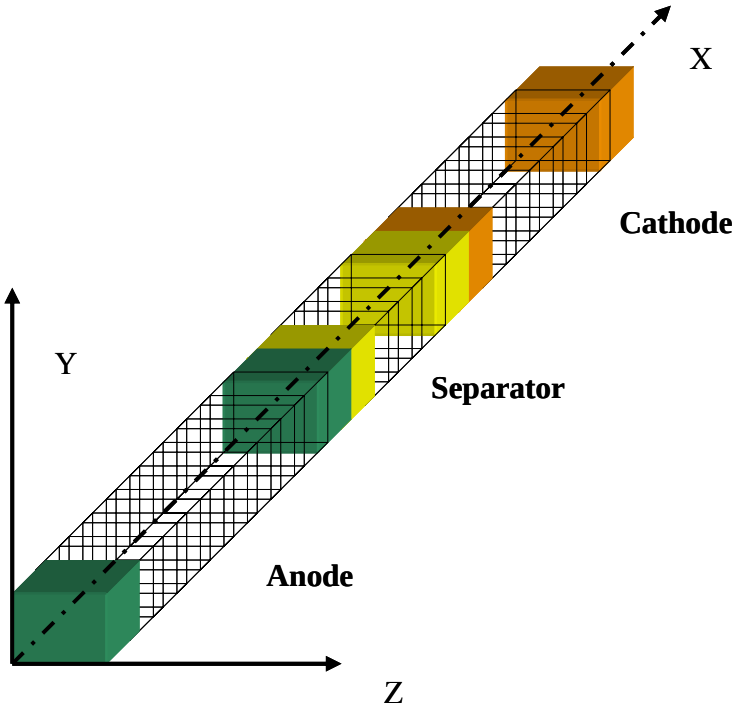

Figure 2.3: Geometry

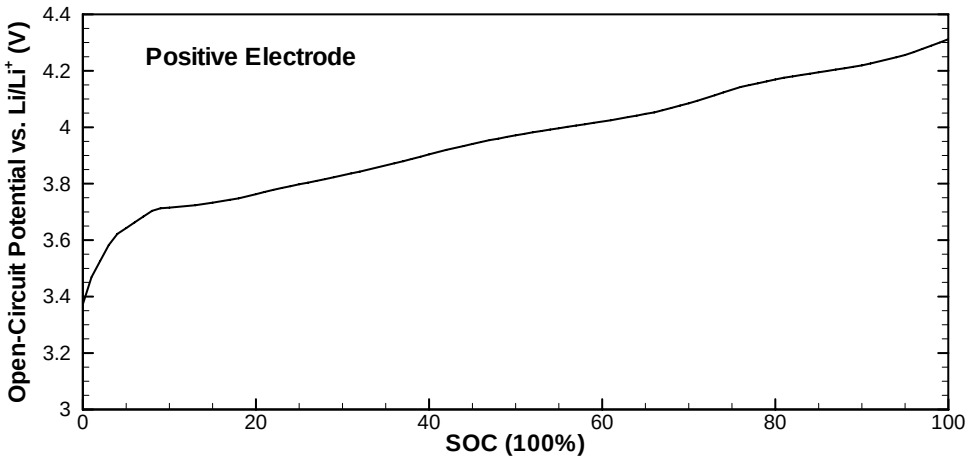

(a)

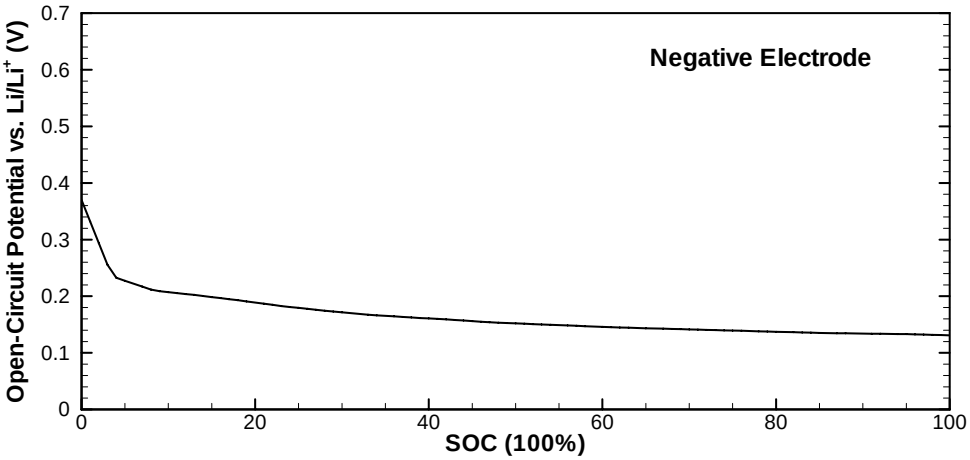

(b)

Figure 2.4: Measured open-circuit potentials vs. Li/Li^+ of: (a) positive electrode and (b) negative electrode using a three-electrode cell at 25°C.

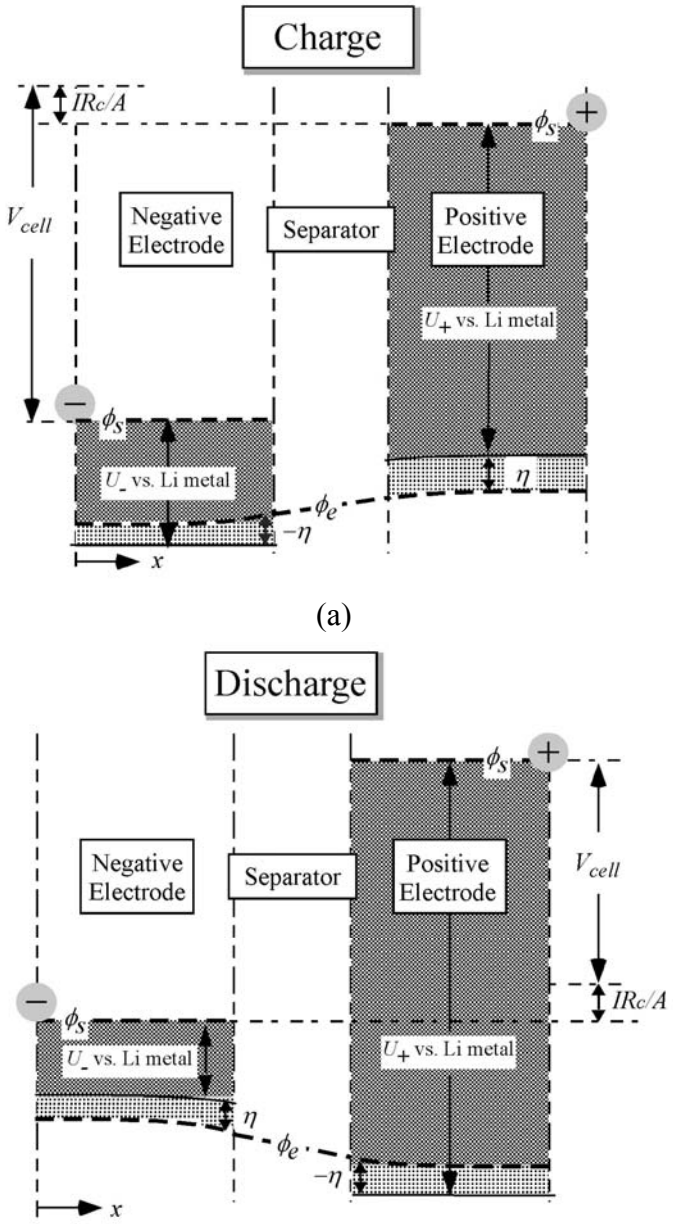

Figure 2.5: The relationship of Vcell and the electrode potentials during (a) charge and (b) discharge.

Chapter 3

Experimental Validation of the ECT Model Using a Three-Electrode Cell

In the previous chapter, an electrochemical-thermal coupled model has been set up, and in this chapter we aim to experimentally validate a capability to predict performance of individual electrodes of Li-ion cells under HEV conditions that encompass a wide range of ambient temperatures. This work is an extension of our previous work on development of comprehensive Li-ion battery models for HEV design, operation and control [**81**,**82**,**89**,**90**,**92**].

3.1 Experimental

The experimental work in this chapter was done by Kwon. In the experiment, a three-electrode cell is made to measure each electrode potential and also a thermocouple is inserted inside the three-electrode cell holder to monitor the average cell temperature. More details about this experiment and the three-electrode cell assembly and temperature/potential measurements can also be found in [**99**,**100**]

3.2 Result and Discussion

Different charge discharge patten such as constant current and pulse current and different temperatures are applied in the experiments with the results being compared to the model output.

3.2.1 Constant Current Validation

The model is first validated by constant current charge and discharge experiments at current rates ranging from 1C (1.2A) to 10C (12A), at room temperature (25ºC). For the cell undergoing constant current charge only, it can't obtain the full capacity (as can be seen from Fig. **3.1,** the charge curves of both model and data) due to the internal resistance, unless the current is very low. For the same reason, the cell can't be fully discharged under constant current condition (see Fig. **3.1**, the discharge curves), unless the current is very low. Usually a following constant voltage charge/discharge process (by decreasing current) is adopted to fully charge/discharge the cell if needed. Thus the cell is charged with constant current until the voltage reaches 4.2V and then is kept at this voltage until the current drops to the cut-off value of 0.1A. The cell then is discharged with constant current until the voltage drops to 2.8V. A model-experimental comparison is shown in Fig. **3.1** for the full cell, where it is seen the predictions match the experimental data quite well for a wide range of C-rates. In Fig. **3.1**, only the constant current charge portions (without the later stage constant voltage charging) are shown. At

low charge/discharge rates, the cell potential stays close to the cell's OCP. As the charge/discharge rate increases, the cell voltage deviates significantly from the OCP due to ohmic (electrolyte ionic resistance), activation (Li insertion/extraction kinetics), and mass transport (Li transport in electrolyte and active material particles) losses.

The measured and predicted cell temperatures are compared in Fig. **3.2** for 1C, 2C, 5C and 10C charge and discharge cases. There is almost no temperature rise for the 1C case since the generated heat is small and can be readily dissipated to the ambient (fixed at 25^{o}C). As the C rate increases, the cell temperature starts to rise significantly above the ambient temperature. For the 2C charge/discharge cases, the cell temperature remains at ~2 to 3ºC above the ambient temperature after about 0.2Ah charge/discharge capacity when the heat generation and dissipation reaches equilibrium. The model prediction generally agrees with the experimental data. For 5C and 10C charge/discharge, there is no thermal equilibrium and the cell temperature keeps rising. For the 10C charge/discharge cases, the cell temperature increases almost linearly as the joule heat from the contact and electronic resistance between the current collector and electrodes dominates heat generation and dissipation. For all the cases, the model captures the cell temperature reasonably well, indicative of the accuracy of the present ECT model.

Next, the behaviors of negative and positive electrodes are separately examined. Fig. **3.3** shows the model-experimental comparison of the potentials of the positive and negative electrodes vs. Li/Li^{+} during 1C, 2C 5C and 10C discharge. The overall agreement of individual electrode's potential is seen to be very good. Fig. **3.3a** shows that the positive electrode potential falls as the discharge current increases from 1C to

10C, while the negative electrode potential rises (Fig. **3.3b**). As mentioned earlier, this departure from the open-circuit potential of each electrode is due to ohmic, kinetic and mass transport losses. The two plots in Fig. **3.3** also reveal that the effect of high C rate is more substantial on the positive electrode than on the negative electrode.

The model prediction of the local SOC profiles in both negative and positive electrodes during 10C discharge is plotted in Fig. **3.4**. (SOC ranges from 0 to 1, where 0 represents the fully discharged state and 1 represents fully charged state. In the code, SOC is calculated at each time step using the solid-phase concentration of Li at the electrode surface.) Initially, SOC in both electrodes is set at unity. During discharge, SOC values in both electrodes decrease with the SOC of the negative electrode dropping faster than that of the positive electrode in a period between 50s and 100s. After that, SOC of the positive electrode drops faster and reaches zero earlier, implying that the discharge is stopped due to the limit of the positive electrode. This difference of SOC evolution in the two electrodes can be explained by Fig. **3.5**, where the solid-phase Li diffusion coefficients of positive and negative electrodes at 25ºC are plotted. The solid-phase Li diffusion coefficient of the positive electrode is measured to be almost constant at 2.0×10^{-10} cm^2/s while its value in the negative electrode is measured to be dependent upon SOC, as shown in Fig. **3.5**[**101**]. It is seen from Fig. **3.5** that initially the Li diffusivity in the negative electrode is much lower than that of the positive electrode, i.e. 2.25×10^{-11} cm^2/s vs. 2.0×10^{-10} cm^2/s, such that the SOC of the negative electrode drops faster. However, Li diffusion coefficient in the negative electrode picks up as SOC drops and becomes much higher than that of the positive electrode during the late stage of

discharge. This explains why the decreasing speed of SOC in the negative electrode is slower as discharge proceeds. The ability of the ECT model to predict not only overall cell performance, but also internal information such as SOC distributions, is useful for design optimization and in-vehicle control of Li-ion batteries.

3.2.2 Pulse Test Validation

The ECT model's capability of simulating pulse charge/discharge characteristic of HEV application is then tested. In this series of tests, 10s discharge and charge pulses at rates of 1C, 2C, 5C and 10C are alternated, with open-circuit relaxation in between (Fig. **3.6**), which is used to mimic the practical HEV battery experience of short consumption and subsequent replenishment to keep the capacity at a constant value. These highly dynamic conditions are more challenging for battery simulation as the requirement for temporal resolution is high. Fig. **3.7a** and **b** show the simulated and measured results for pulse tests at 25ºC and 0ºC with the initial battery SOC at 40% and 60%, respectively. Again the model prediction closely matches the experimental data. Of particular interest are the pulsing cases at 0^{o}C. While it is widely observed that lithium deposition occurs at high rate, low temperature charging, its fundamental mechanism has not been pinpointed clearly. One hypothesis is that the negative electrode potential drops to zero or even negative, thereby thermodynamically favoring Li deposition. Fig. **3.8** thus plots the predicted and measured potential of the negative and positive electrodes separately in these pulsing cases for the initial SOC of 60%. Indeed, it is seen in Fig. **3.8**.

that the negative electrode potential turns negative under 5C and 10C pulse charge, indicating the onset of lithium deposition. Post-mortem material characterization is currently underway to verify whether lithium deposition occurs under these circumstances.

3.3 Conclusions

An electrochemical-thermal (ECT) model has been used to explore Li-ion battery performance for HEV application. For the first time, the model was validated against the experimental data for a full cell as well as individual electrodes under constant charge/discharge and pulse conditions representative of HEVs. Good agreement is found between model predictions and experimental measurements obtained using a three-electrode cell equipped with an internal thermocouple. The capability of the present ECT model in predicting the negative electrode potential opens the possibility to forecast and prevent the conditions leading to Li deposition and hence capacity loss of automotive Li-ion batteries. Future work includes addition of side reactions to the present performance model so as to capture degradation processes and develop a predictive tool for the battery cycle life under typical driving conditions. Finally, control strategies for mitigating Li-ion battery degradation are to be explored.

.

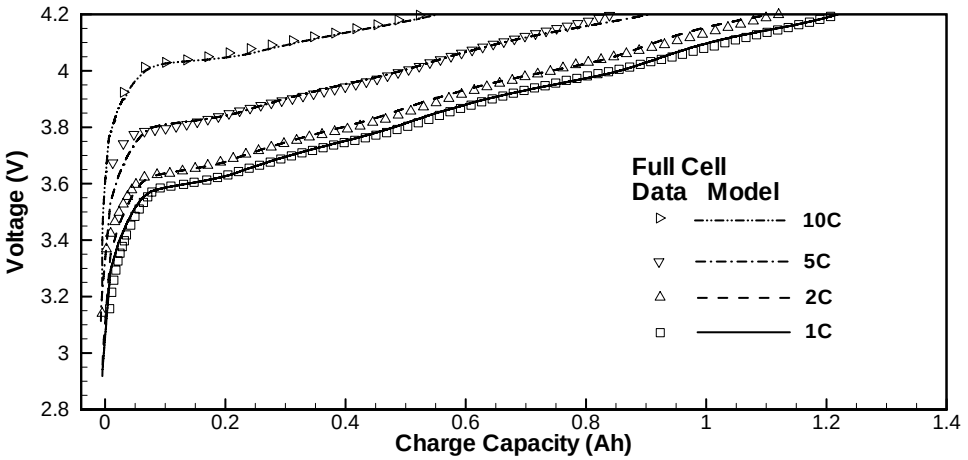

(a)

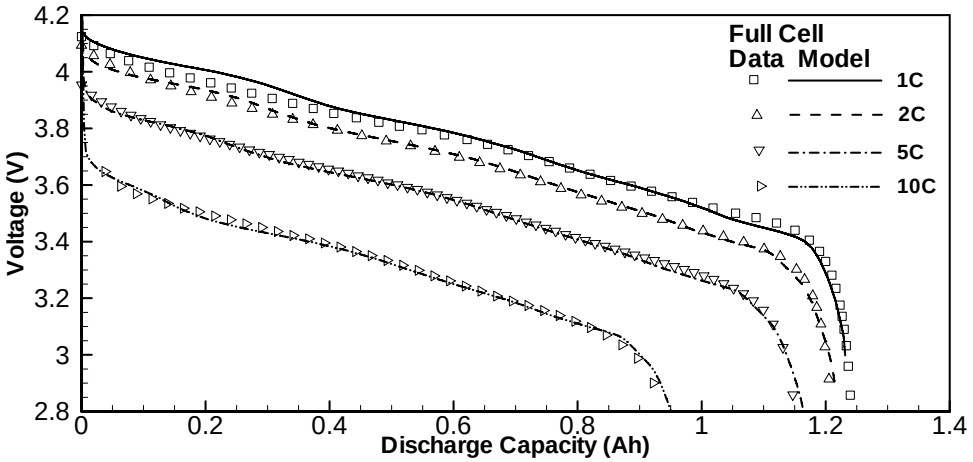

(b)

Figure 3.1: Experimental and simulated of cell voltages for constant current (a) charge and (b) discharge.

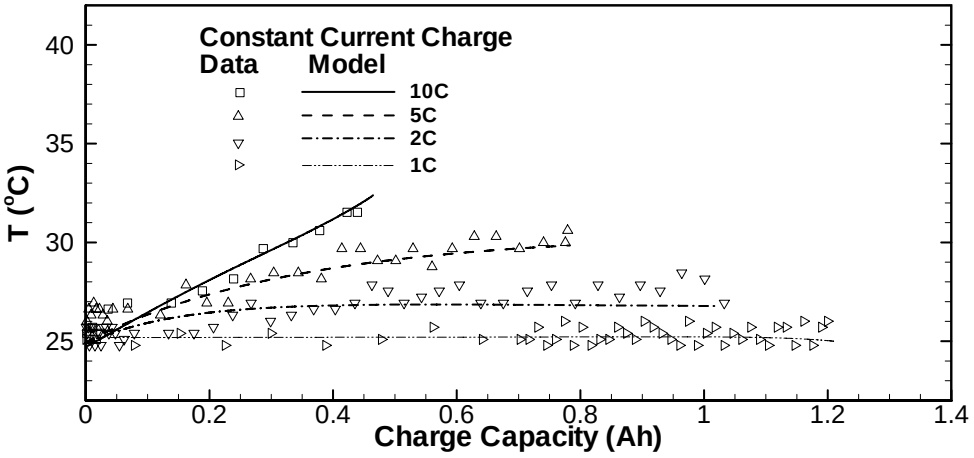

(a)

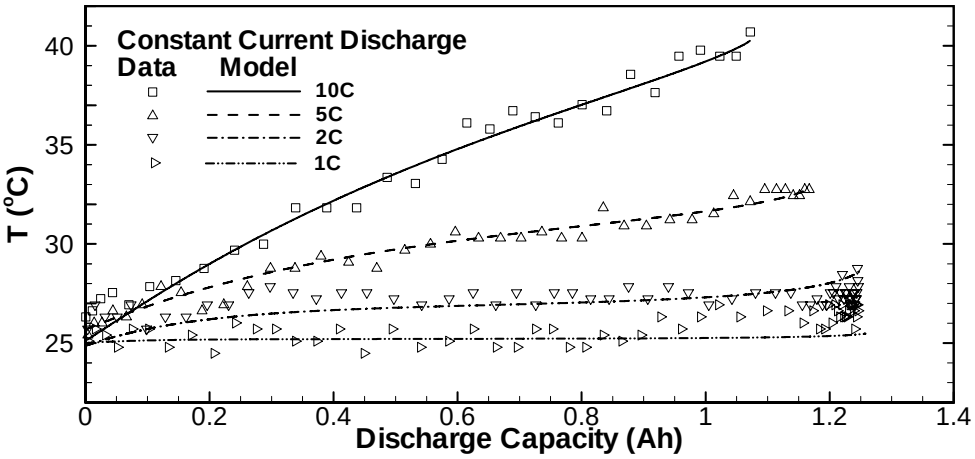

(b)

Figure 3.2: Experimental and simulated cell temperature for constant current (a) charge and (b) discharge. The initial cell temperature and ambient temperature are at 25°C.

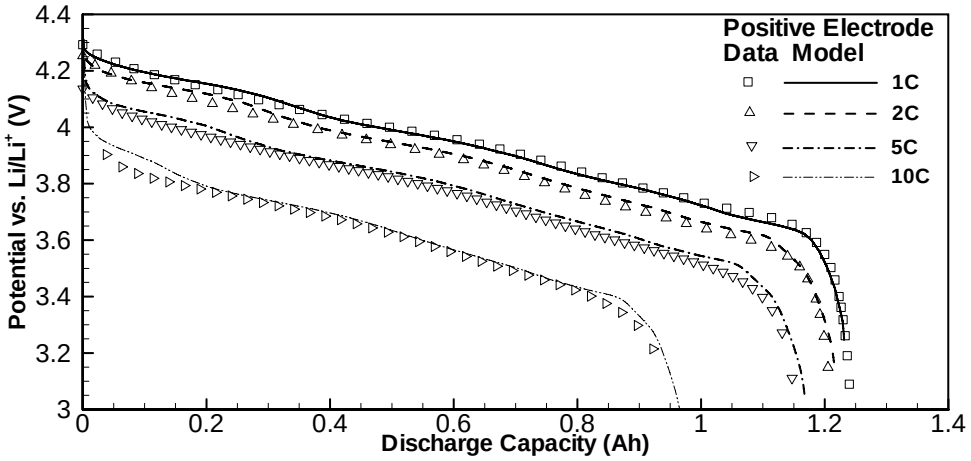

(a)

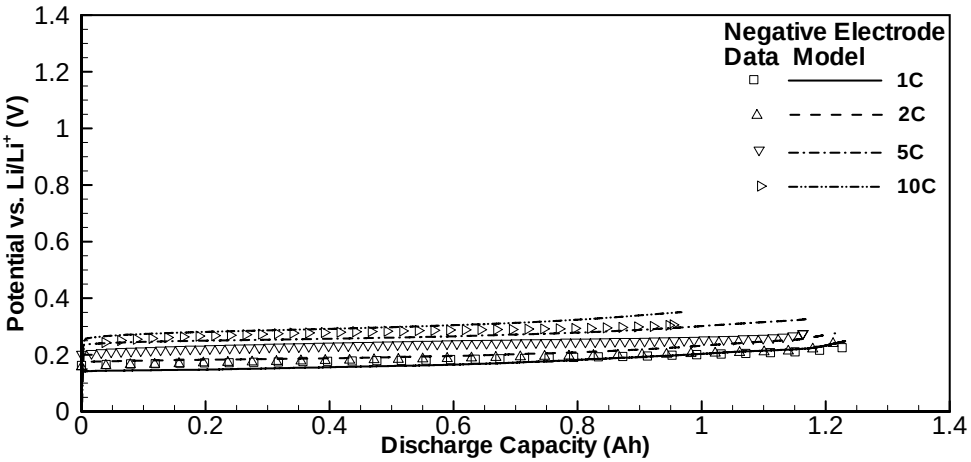

(b)

Figure **3.3**: Experimental and simulated (a) positive and (b) negative electrode potential evolutions during constant current discharge.

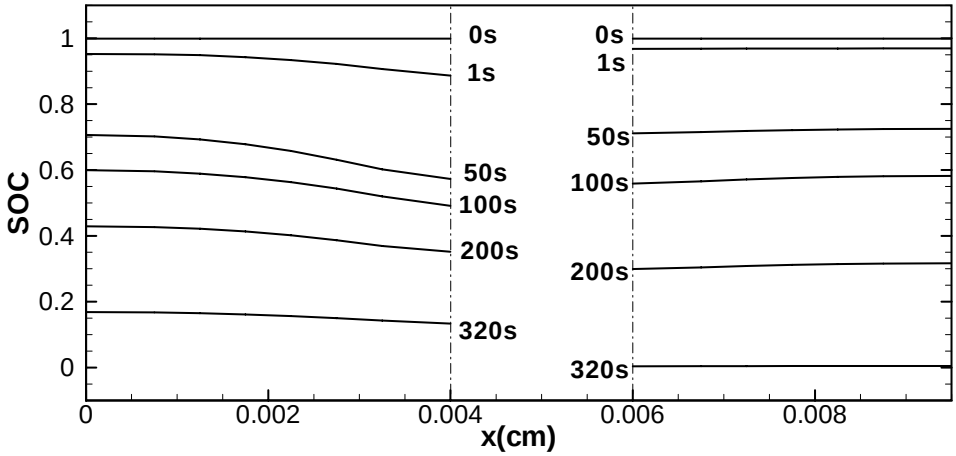

Figure 3.4: Distribution of the normalized Li concentration at particle surfaces during 10C discharge. The cell regions from left to right are negative electrode, separator, and positive electrode.

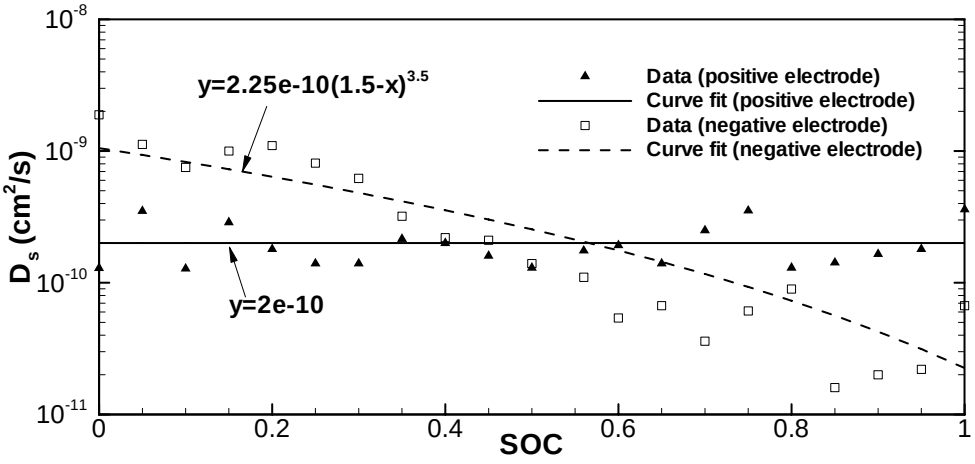

Figure 3.5: Experimental measurement (Kwon and Wang, 2010) and curve fit of the solid-phase Li diffusion coefficient in positive and negative electrodes.

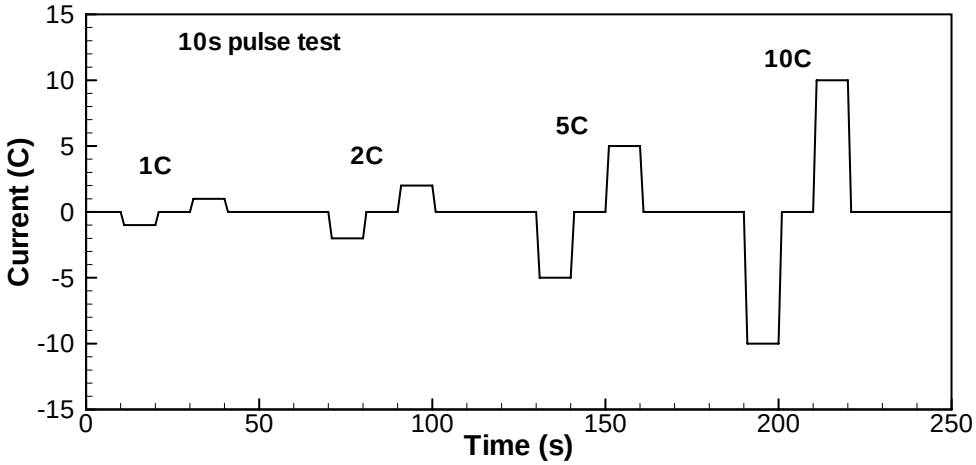

Figure 3.6: Pulse test current profile.

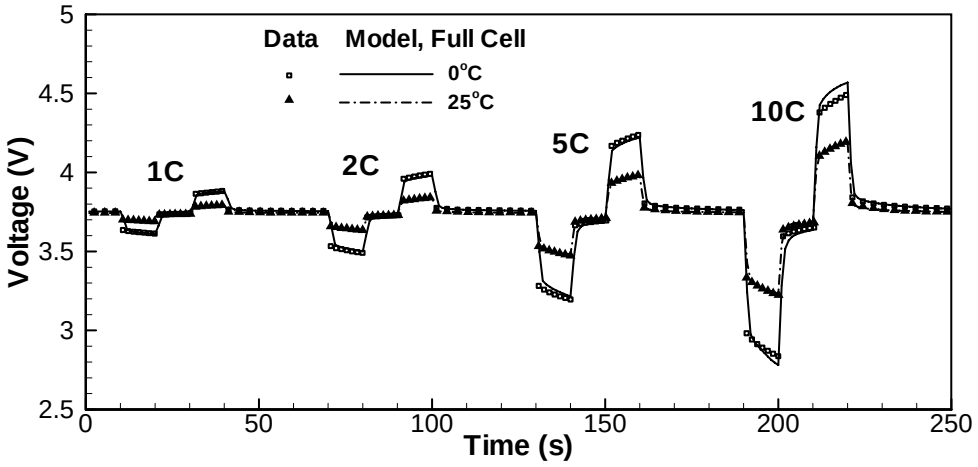

(a)

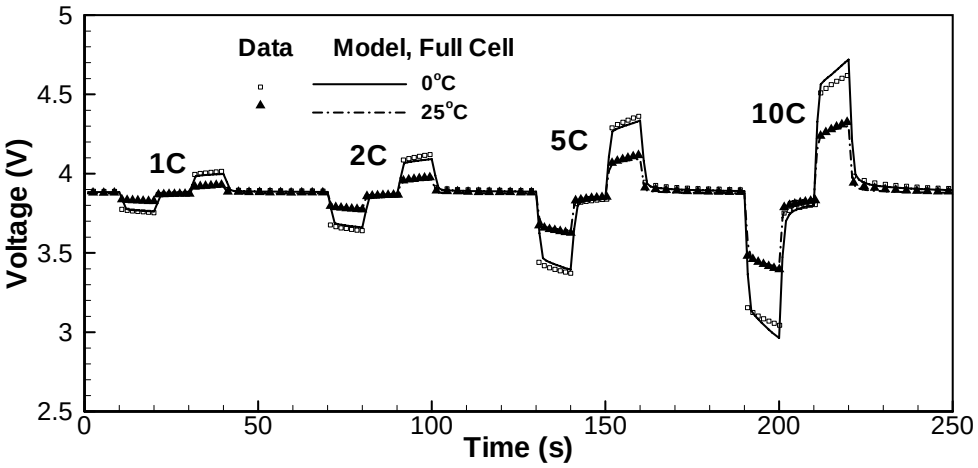

Figure 3.7: (a) Model validation by experimental data for the cell voltage with initial SOC of: (a) 40% and (b) 60% at 25°C and 0°C.

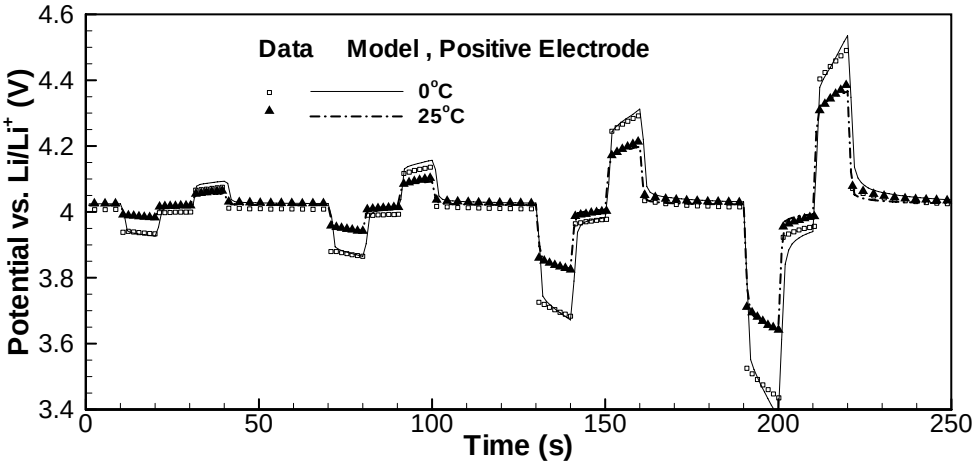

(a)

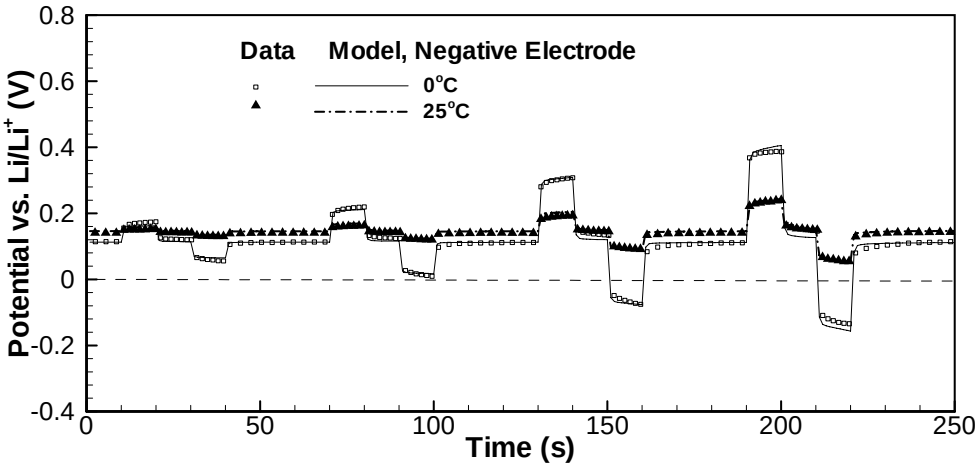

(b)

Figure 3.8: Model validation by experimental data for the potential evolution of: (a) positive electrode and (b) negative electrode with initial SOC of 60% at 25°C and 0°C.

Chapter 4

Study on Subzero Temperature Performance of Automobile Li-Ion Battery

Compared to the studies on Li-ion cells at room temperature, studies at subzero temperature are relatively limited in spite of the fact that peak performance in subzero environmental conditions is required for HEVs. Several possible reasons for low performance of Li-ion cell at subzero temperature are still subject to arguments. For instance, SEI layer, charge transfer resistance and lithium diffusion in the graphite are all suggested to be the limiting factors, even though conductivity of the electrolyte has been excluded, according to many studies. Among these factors, lithium diffusion in carbon is considered the most important factor based on many studies, while the others are doubted [**102**].

Charging the Li-ion battery at subzero temperature is still a big challenge due to the low electrokinetics at low temperature. First, it is very difficult to charge the Li-ion cell to the full capacity obtainable at room temperature due to the increased internal resistance at subzero temperature.

Secondly, Li deposition may occur at the negative carbon electrode, especially at high charge rates. Li deposition is expected to occur on the negative carbon electrode when either the electrode is highly polarized (such as when the electrode potential vs. Li/Li^+ is below 0V or even higher, e.g. 20mV) or when lithium becomes oversaturated on the negative carbon electrode particle surface during charging. At very high charging current, once the Li^+ ions are transported to the negative carbon electrode but cannot be

efficiently intercalated into the electrode particle, Li^+ ion may deposit as metallic Li. The Li diffusion coefficient is reduced at low temperature, which makes this situation even worse. Some of the deposited Li may be reversed at high temperature while some may not be reused in the following cycling, causing permanent capacity loss. The deposited metallic Li can also lead to internal shorting by punching through the separator.

This chapter aims to predict the onset of Li deposition through model simulation and further compare with experimental evidence of [**101**]. The electrochemical-thermal coupled (ECT) model previously developed can be a powerful tool to study this problem based on its capability to model Li-ion performance over a wide range of temperatures. Another task is to study suitable charging protocols for Li-ion batteries at subzero temperatures using the ECT model.

4.1 Approaches

The experiment was done by Kwon and will be briefly introduced here. To determine whether Li deposition on the negative carbon electrode is occurring during a charge process, cell capacity is checked before and after a charge process in the experiment and Li deposition is considered to occur if cell capacity loss is greater than 2%. For more detail on Li deposition experiments, please check the reference [**101**]. One direct way to find the onset conditions of Li deposition is to check the negative electrode potential. It is often considered that Li deposition occurs when the negative electrode potential decreases to 0V vs. Li/Li^+ during charge, or even higher (e.g. 20mV). Plan A of

the experiment is to find the negative electrode potential when Li deposition is considered to occur, i.e. the threshold potential. This method is quite effective at the beginning, and results show that at 0 and -10^{o} C, capacity loss occurs when the negative electrode is lower than 50mV. Fig. **4.1** is adopted from the experimental report showing the cell capacity check before and after test to determine whether Li deposition occurs during the charging at the specific condition.

However, some unpredicted phenomena were observed which makes this criterion unreliable. First, for some cases, the negative electrode potential does not drop below 50mV even though capacity loss does occur. Second, for some other cases, the negative electrode voltage drops to subzero value immediately after charging, however, there is no capacity loss even after about 10 minutes. Therefore plan B is proposed. Plan B seeks to determine the relationship between the onset condition of Li deposition and the charge capacity. In this plan, the cells are charged from fully discharged state (i.e. SOC=0) with four charge rates (1, 2, 5, and 10C) at four temperatures (-20,-10, 0 and 25°C) to ascertain the critical conditions. Since no capacity loss is observed in the experiment for charging at 25°C, we will focus on the subzero temperature charging in this study.

At the same time, the ECT model is also used to simulate the above 16 cases and the results will be discussed in the following section. While the direct results of experiments provide powerful evidence to study capacity loss at different conditions, they have limitations in revealing more information on what is happening inside the cell. By combining both the experimental and simulation results, we attempt to provide some explanation which may be useful in cell design and charge protocol design.

4.2 Result and Discussion

4.2.1 Onset Conditions of Li Deposition

In experiments, by charging a cell several times at a fixed temperature and recording the capacity loss, the onset conditions (based on charged capacity) of Li deposition at different temperatures were obtained. The result is plotted in Fig. **4.2** (represented by symbol)**.** In Fig. **4.2**, each symbol indicates a threshold value for charged capacity at that temperature, that is, if a cell is charged beyond this capacity, the cell capacity loss would be greater than 2%. Please notice that all the charge processes were taken from fully discharged status. Capacity loss was observed to be greater than 2% in all 12 cases.

As discussed, Li deposition may occur when Li ion cannot be effectively inserted into the negative carbon electrode particle. In the model simulation, this means once the Li concentration of the electrode particle surface becomes saturated, further charging may cause Li deposition. In Fig. **4.2**, the model prediction of the onset conditions for Li deposition is also shown (represented by symbol+curve). A symbol at a certain temperature indicates the state that in someplace of the negative electrode, the SOC of particle surface reaches unity, which means Li concentration on the particle surface reaches saturation. In Fig. **4.2**, the model prediction matches the experimental data well so the model can be used for further studies.

Fig. **4.2** also shows that it is very hard to charge the cell without causing damage (Li deposition) to the cell at high charge rate and low temperature. So if we wish to charge a cell under subzero temperatures, constant current charge is not a good choice. Other charge protocols, such as pulse charge, should be adopted and will be discussed later in this chapter.

Li concentration on the negative carbon electrode particle surface (indicated by SOC in the model simulation) is the key parameter to determine whether or not Li deposition occurs during a charge process. Its value is very difficult to measure experimentally, but can be studied by model simulation. The evolution of Li concentration in the electrolyte and electrode during charge of 5C charge at -10^{o} C and 10C charge at -20^{o} C is shown in Fig. **4.3** and Fig. **4.4**. In both cases, capacity losses were observed in the experiments. In Fig. **4.3a**, the electrolyte concentration quickly decreases in almost the entire negative electrode, so that most Li insertion is performed inside the narrow region near the separator while the other part of negative electrode is far from saturation (see Fig. **4.3b**). However, for the 10C case, the particle surface concentration of the entire negative electrode quickly increases to the saturation value (i.e., SOC reaches unity) (Fig. **4.4 b**). Although there is slight difference of Li concentration evolution for these two cases, in both instances the Li insertion is not quick enough so that Li ion is easily accumulated on the particle surface and Li deposition may occur.

In Fig. **4.5** to Fig. **4.8**, the Li concentration of 10C charge at the four temperatures is plotted from 25^{o} C to -20^{o} C. Except at 25^{o} C, capacity loss was observed in all the cases at 0, -10 and -20^{o} C in experiment [**101**].

Comparing Fig. **4.5a**, Fig. **4.6a** and Fig. **4.7a**, the surface SOC of the negative electrode particle becomes non-uniform as temperature decreases with the surface SOC of the electrode particle near the separator increasing faster than the other part. On the contrary, in the last case (Fig. **4.8a**), the surface SOC of the whole negative electrode particle increased in a very short time. In all the three cases with capacity loss observed, Li^{+} ion cannot be inserted into the negative electrode particle quickly enough due to the reduced Li diffusion coefficient in the negative electrode.

Next, the simulated electrolyte concentration distribution is compared. For all three cases with capacity loss observed (Fig. **4.6b,** Fig. **4.7b**, and Fig. **4.8b**), the electrolyte concentration greatly decreases in the negative electrode and Li insertion is forced to perform inside a small region near the separator causing surface over saturation. On the contrary, in the case with no capacity loss observed (Fig. **4.5a**), the electrolyte concentration varies little from the initial value in the electrode, thus the reaction is more uniform inside the cell and Li deposition is less likely to happen. This phenomenon, observed by simulation, may indicate some useful application in Li-ion battery charging.

To further check the key factors that control Li deposition, some parametric studies are carried out. As mentioned, Li diffusion in the negative electrode is widely considered to be the most important factor for low cell performance at low temperature. In this study, Li diffusion coefficients of the positive and negative electrodes, $D_{s,c}$ and

$D_{s,a}$, are measured at different temperatures and plotted in Fig. **4.9** and Fig. **4.10**, respectively. In the model, the values of $D_{s,c}$ and $D_{s,a}$ are determined from these experimental data by curve fitting. As temperature decreases from 25° C to -10° C, $D_{s,a}$ decreases about 2 orders of magnitude while $D_{s,c}$ decreases only about 1 order. This means, at subzero temperature, the negative electrode will become the electrode that limits the cell performance, due to the poor Li insertion performance. The change of $D_{s,c}$ with SOC is reasonably small and thus is ignored in the model. However, the change of $D_{s,a}$ with SOC is much greater so in the model $D_{s,a}$ is function of SOC as well. As it is mentioned, $D_{s,a}$ also decreases as SOC increases from zero to unity, so as the charging process goes on and SOC rises, the rate of Li diffusion into the negative electrode particle will be reduced, and in return, the increase of SOC will be accelerated.

From the above analysis, it is clear that improving the Li diffusion rate into the negative carbon electrode particle will be an effective way to improve Li-ion cell performance at subzero temperature. This can be realized by either increasing the Li diffusion coefficient in the negative electrode or by reducing the negative electrode particle size. From the view of manufacture, the later method is relatively easier. This was also proved by our model simulation, as shown in Fig. **4.11**. It is very clear that the one with smaller particle radius has much better performance. To compare, a simulation with Li diffusion coefficient of negative carbon electrode increased to 10 times was also carried out and the conclusion is that it obtains the similar improvement.

4.2.2 Charging Protocol under Subzero Temperature

Charging of Li-ion battery under subzero temperature is very important in HEV application. Therefore, one application of this study is to develop proper charging protocols at subzero temperature, which is much less studied than room temperature charging.

Conventional Li-ion battery charging consists of two stages, as shown in Fig. **4.12**. The battery is first charged with a constant current (CC) until the cell voltage reaches the cutoff voltage, followed by a constant voltage (CV) charging until the current drops to about 3% of its rate value. The CC stage typically takes 1h (with 1C constant current) and about 88% of the cell capacity is charged. The CV stage takes about 1.2 to 2h to charge the rest. One disadvantage of charging Li-ion battery at high voltage is that it will decrease the cycle life, probably due to side reactions.

Fig. **4.13** shows the simulation result of the percentage of charged capacity (based on the nominal cell capacity) after CC charge at different temperatures. It shows that as charge rate increases (from left to right), less capacity can be charged into the cell during the CC stage and more charging is required during the CV stage by reducing the current. Also as temperature decreases (from top to bottom), less capacity can be charged into the cell during the CC stage. In addition, Li deposition at subzero temperature should also be considered. All of these factors make it a tough job to develop an efficient charging protocol at subzero temperature.

As discussed, Li diffusion coefficient in the electrodes will be greatly increased with temperature. To take advantage of this, the protocol should be well designed to

increase the cell temperature first. For the situation where there is no subsidiary heating system, the cell temperature can be increased by utilizing the heat generated during the charge-discharge process. From the study in Chapter 3, the rising rate of the cell temperature is strongly related to the charge/discharge rate. So high charge/discharge rate should be adopted to quickly increase the cell temperature at the beginning stage. In order to prolong the heating time, constant current should be replaced by pulse current, while the pulse current should also be well designed to avoid Li deposition.

In Fig. **4.14a** the current profiles of three different charge protocols are shown. They are constant 10C current charge, pulse 10C charge (charge+rest) and pulse 10C charge-discharge (charge+rest+discharge). Fig. **4.14b** shows that under the constant 10C current charge, the SOC (of the negative electrode particle surface near the separator) reaches unity in very short time (less than 20s). As comparison, under the pulse 10C charge protocol, it lasts for about 200s, and for the pulse charge-discharge protocol including discharge, the SOC does not reach unity even after 600s. This greatly reduces Li deposition.

The cell temperature and charged capacity under these three protocols is shown in Fig. **4.15**. The improvement of cell temperature and charged capacity from constant current protocol to the pulse charge protocol is small. However, in the pulse charge-discharge protocol, the cell temperature could be greatly increased from the above two protocols because the cell is also heated up when it is discharged.

This pulse charge-discharge protocol is still not optimized and has room for improvement through a better design. In Fig. **4.16**, “protocol 1” represents the above pulse charge-discharge protocol, and “protocol 2” represents an improved pulse charge-

discharge protocol. In protocol 2, both charging and discharging periods are extended in one cycle so that the heating time is prolonged. Furthermore, the ratio of charging and discharging period is increased so that more capacity can be charged in one cycle. Certainly, all these improvements should be done under the condition that the SOC (of the negative electrode particle surface) does not reach unity during the whole process to avoid Li deposition.

Fig. **4.16b** shows that the surface SOC of the negative electrode particle near the separator rises fastest in each protocol and never reach unity during the whole process. At the beginning stage, the SOC of protocol 2 varies extensively compared to protocol 1 due to the extension of charge and discharge time. However, the variation is relaxed after about 100s, and getting close to protocol 1. By checking the cell temperature from Fig. **4.17a**, we can find that, the cell temperature increases quickly during the process so that the Li diffusion coefficient of the negative electrode is greatly increased. This is why the variation of the SOC is getting smaller. After about 10 minutes, the cell temperature in protocol 2 reaches about 17°C which means the cell is effectively heated up, indicating the charge protocol under subzero is done and the optimized charge protocol under room temperature can be applied.

Fig. **4.17b**, also shows that the charged capacity of protocol 2 is larger than that of protocol 1 due to the rising of charging period. Fig. **4.18** shows that as temperature increases, the internal resistance is reduced and therefore the overpotential decreases (as the arrows indicate).

Fig. **4.19a** shows that during the first 600s (step 1) the capacity charge efficiency of the protocol 2 is similar to 2C constant charge case, however, Fig. **4.19b** shows that for 2C constant charge case, SOC reaches unity after about 600s, while this is not the case in protocol 2. Fig. **4.19c** also shows that there is only small temperature increase for the 2C constant charge case.

Also shown in Fig. **4.19** are the second step charges of protocol 2 after 600s, which are 2C, 5C and 10C constant current charges. In step 2, the constant charge lasts another 602s, 299s and 46s for 2C, 5C and 10C, respectively. And then the SOC of the cell near separator reaches unity for all the three cases. The final charged capacities for these three cases are 83%(2C case), 76%(5C case) and 58%(10C case), respectively. Although the charged capacity of the 2C case is the most, it takes longest time and the cell temperature drops to about 3°C which is not a wanted result. Under the 10C case, the cell temperature keeps increasing but the charged capacity is the least. For 5C case, the cell temperature drops to about 14°C but the charged capacity is higher than 10C case. Overall, during step 2, the charge rate should not be too low, otherwise the cell temperature will greatly drop. On the other hand, how high the current should be applied is dependent of the practical needs.

In this study, three different type of charging protocols are compared using the validated ECT model. The results show that the pulse charge-discharge protocol aiming to heat up the cell as quickly as possible is the best of these three protocols. Development of an efficient charging protocol at subzero temperature is a difficult challenge, requiring attention not only to the importance of charging speed, but also to the avoidance of that

Li deposition. In this study it is shown that the ECT model can be a powerful tool in this application.

4.3 Conclusions

The Li-ion cell is still not able to satisfy the current HEV application at subzero temperature. Li diffusion coefficient in the electrodes decreases greatly at subzero temperature which makes Li insertion rate unable to meet the rapid charging requirement. One serious problem for charging Li-ion battery at subzero temperature is that Li may deposit at the surface of the negative carbon electrode. Li deposition is favored by low temperature and high charge rate. To reduce the chance of Li deposition, improving Li diffusion performance is an effective solution. This can be obtained by either reducing the negative electrode particle size or improving the Li diffusion coefficient.

In this chapter, the previously developed ECT model is validated with experiments under subzero temperature conditions and used to study cell behavior under this situation. One observation from the model study is that, either low temperature or high charge rate may force Li insertion into the negative carbon electrode to occur in a narrow region near the separator. Therefore the electrode particle surface concentration increases more quickly in this area such that Li deposition is mostly like to happen in this region.

The model is then used to study charging protocol under subzero temperature. The study shows that a well designed charge protocol is very important in order to safely

charge the cell under subzero temperature and avoid Li deposition at the same time. Simulation results show that the key step is to heat up the cell as quickly as possible at the beginning stage. This can be realized by a charging protocol with high rate charge-discharge pulse current. The ECT model is proved to be a powerful tool in this application.

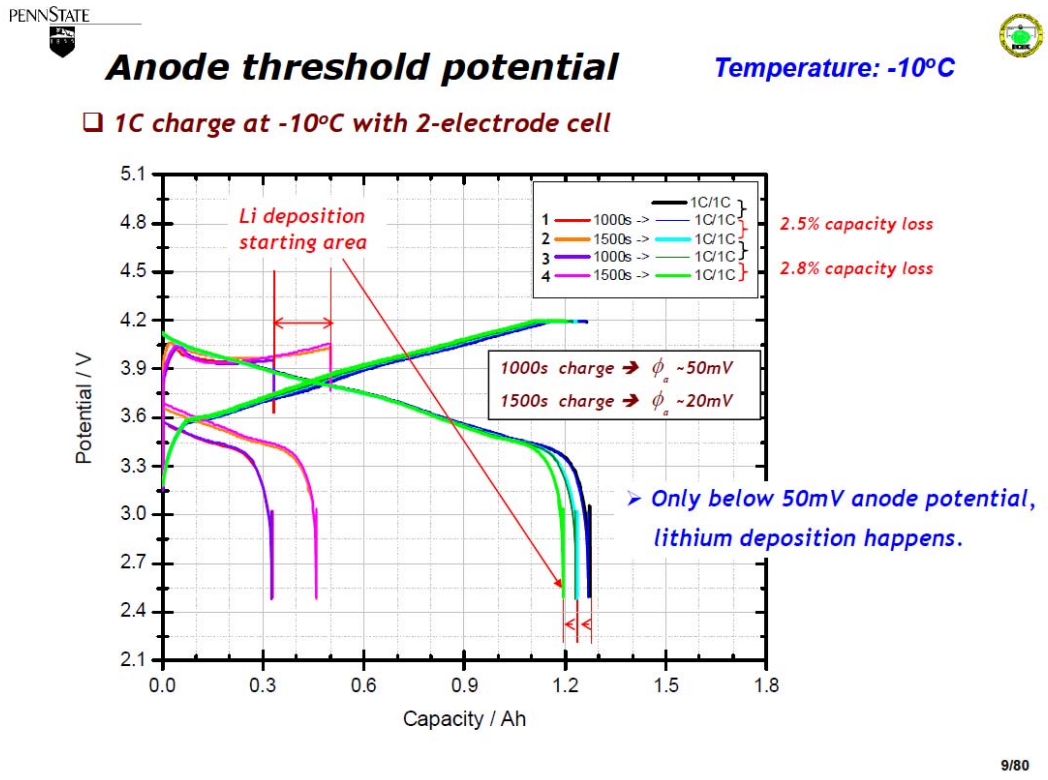

Figure 4.1: Cell capacity checked before and after the cell is charged from SOC=0 at -10°C. (Kwon and Wang, 2010)

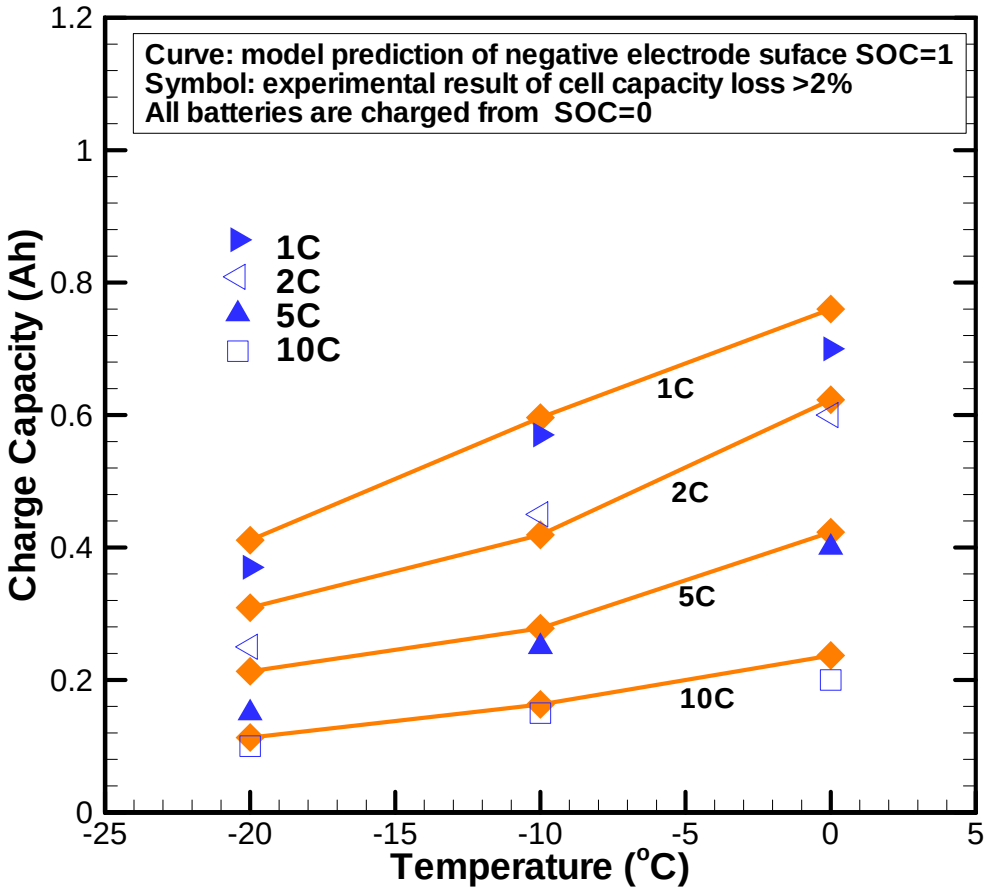

Figure 4.2: Experimental (Kwon and Wang, 2010) and model prediction of onset condition for Li deposition on the negative electrode at different chamber temperatures.

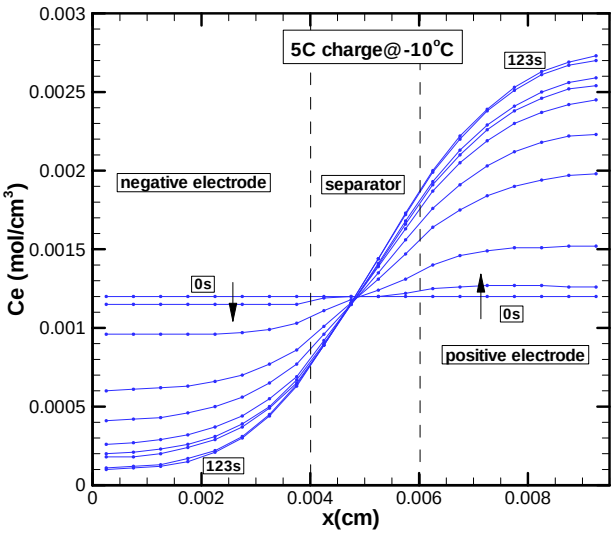

(a)

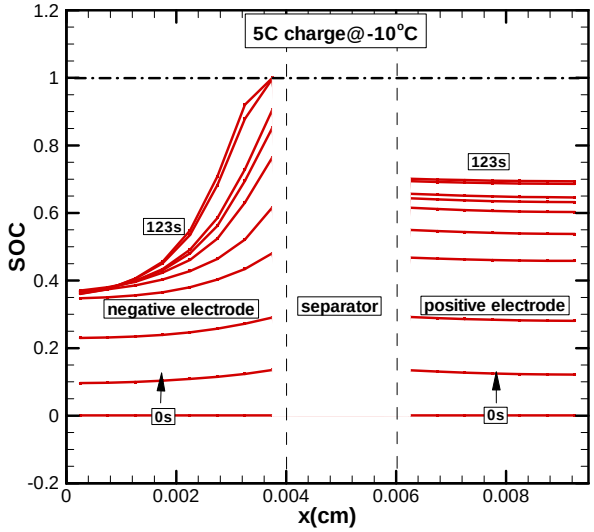

(b)

Figure 4.3: Model simulation of (a) electrolyte Li concentration and (b) surface SOC of the electrode particle for 5C charge at -10°C (chamber temperature); initial SOC=0 everywhere in the electrodes.

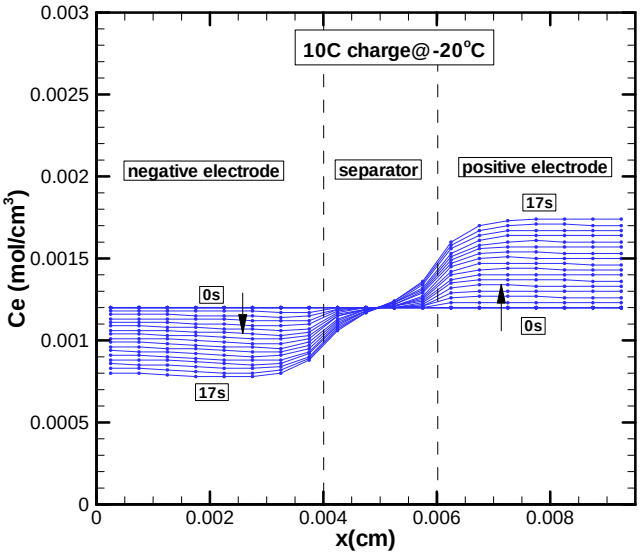

(a)

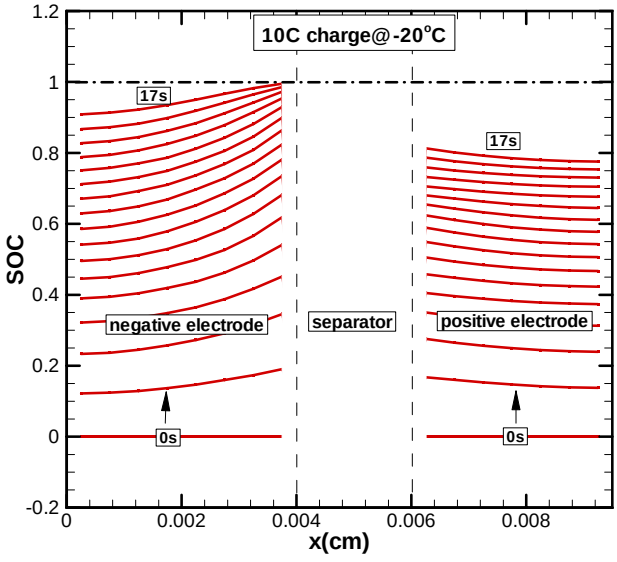

(b)

Figure 4.4: Model simulation of (a) electrolyte Li concentration and (b) surface SOC of the electrode particle for 10C charge at -10°C(chamber temperature); initial SOC=0 everywhere in the electrodes.

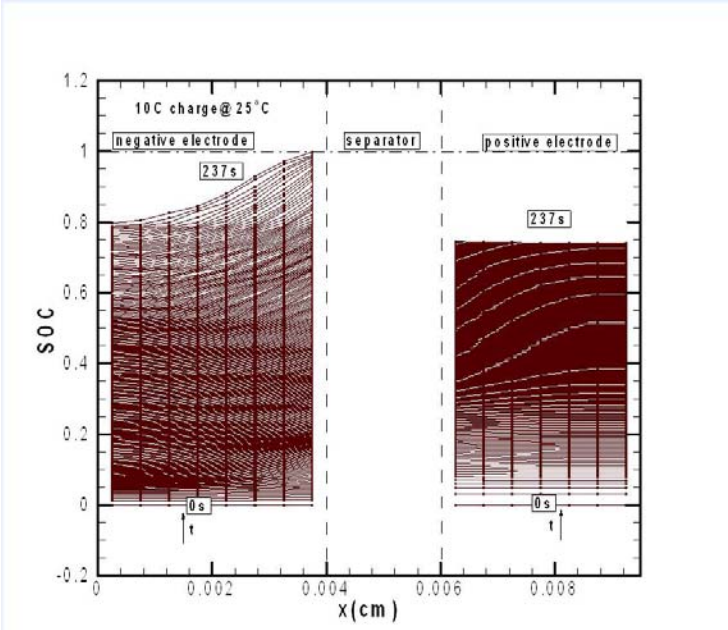

(a)

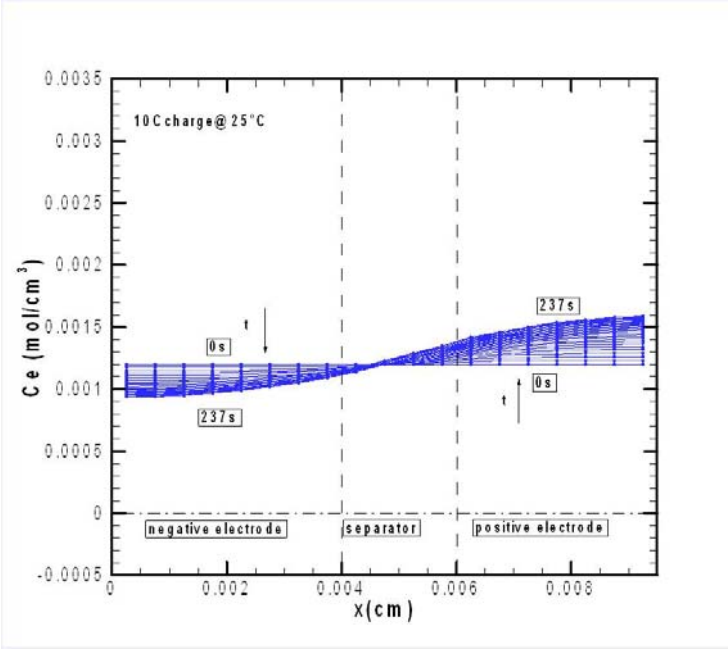

(b)

Figure 4.5: Model simulation of (a) surface SOC of the electrode particle and (b) electrolyte Li concentration for 10C charge at 25°C(chamber temperature), initial SOC=0 everywhere in the electrodes.

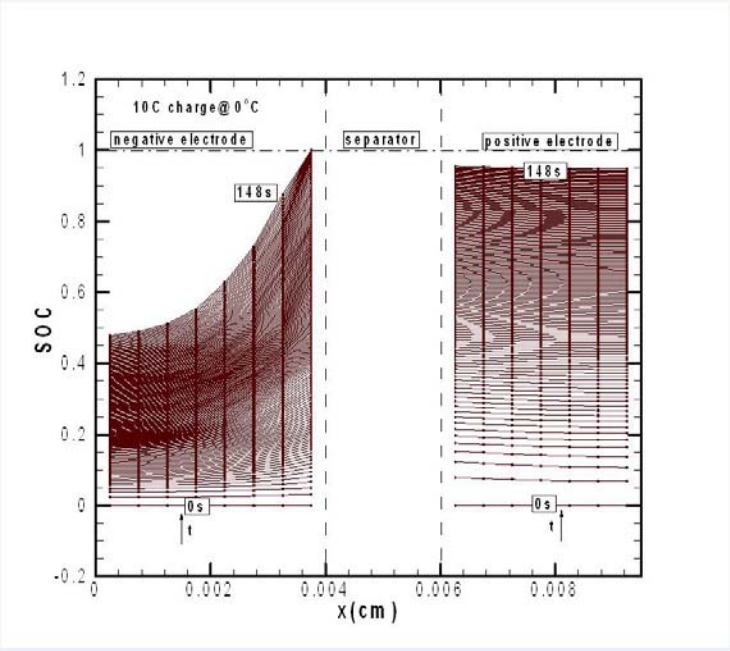

(a)

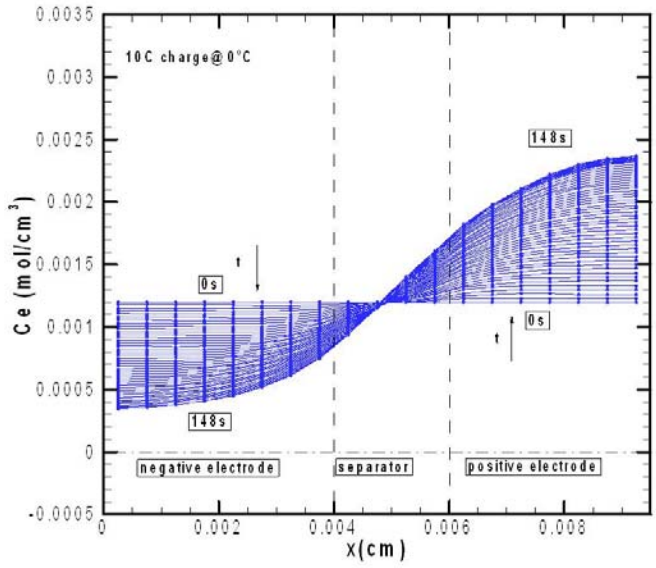

(b)

Figure 4.6: Model simulation of (a) surface SOC of the electrode particle and (b) electrolyte Li concentration for 10C charge at 0°C(chamber temperature), initial SOC=0 everywhere in the electrodes.

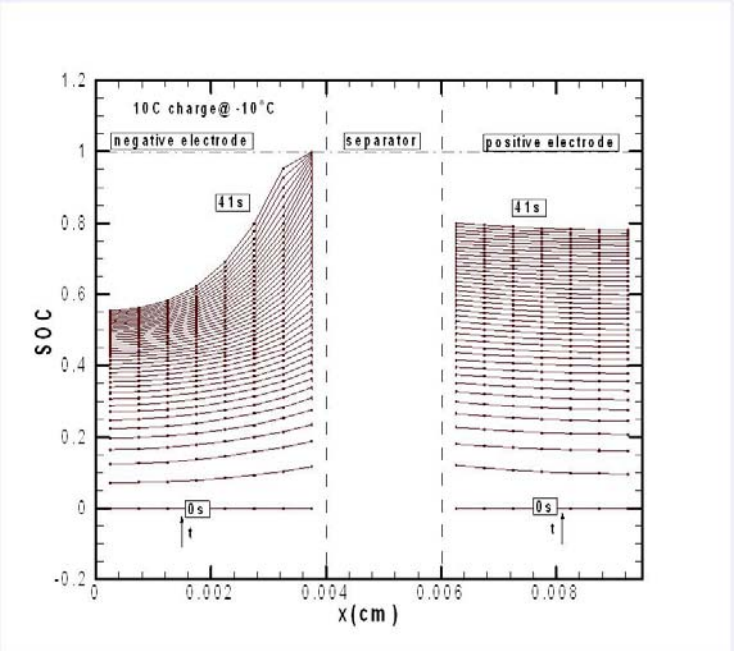

(a)

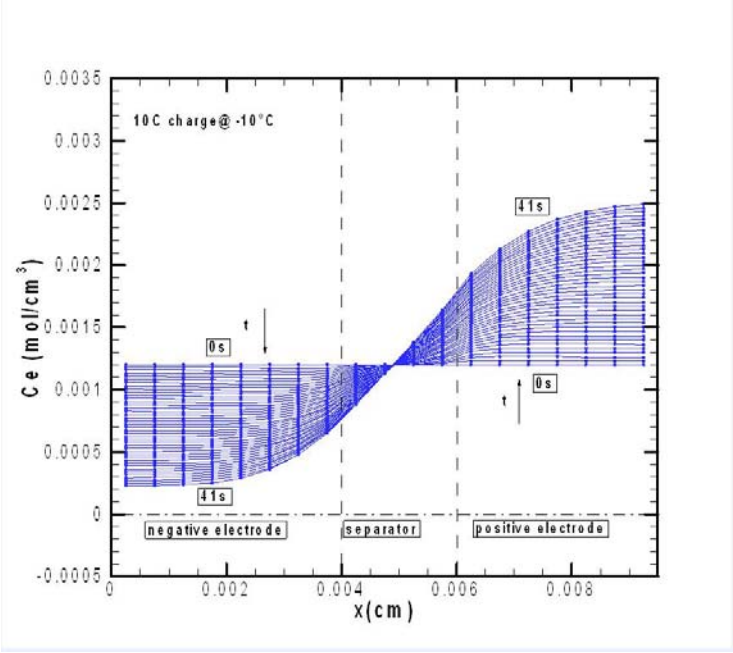

(b)

Figure 4.7: Model simulation of (a) SOC distribution and (b) electrolyte Li concentration for 10C charge at -10°C(chamber temperature), initial SOC=0 everywhere in the electrodes.

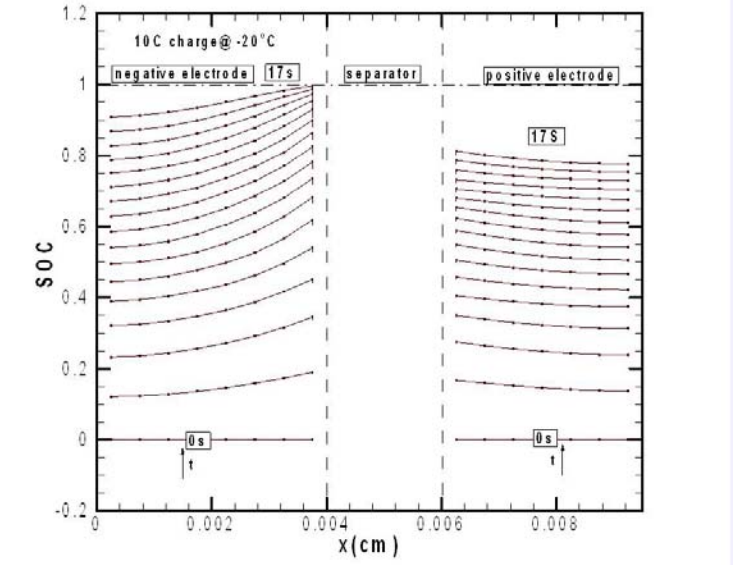

(a)

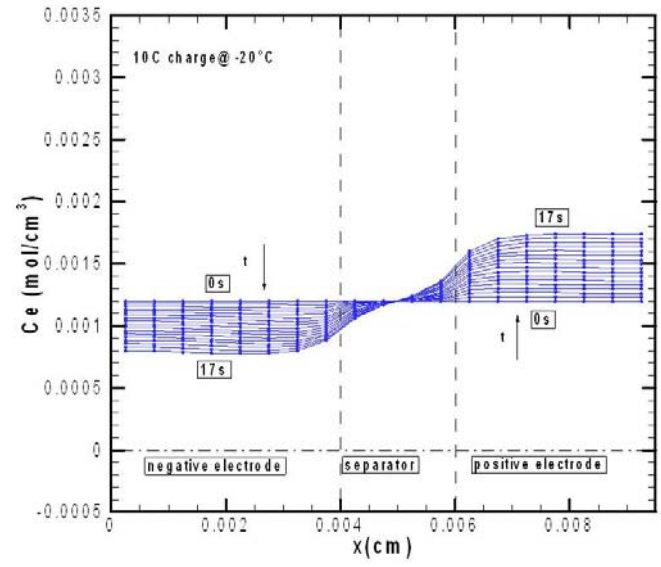

(b)

Figure 4.8: Model simulation of (a) surface SOC of the electrode particle and (b) electrolyte Li concentration for 10C charge at -20°C(chamber temperature), initial SOC=0 everywhere in the electrodes.

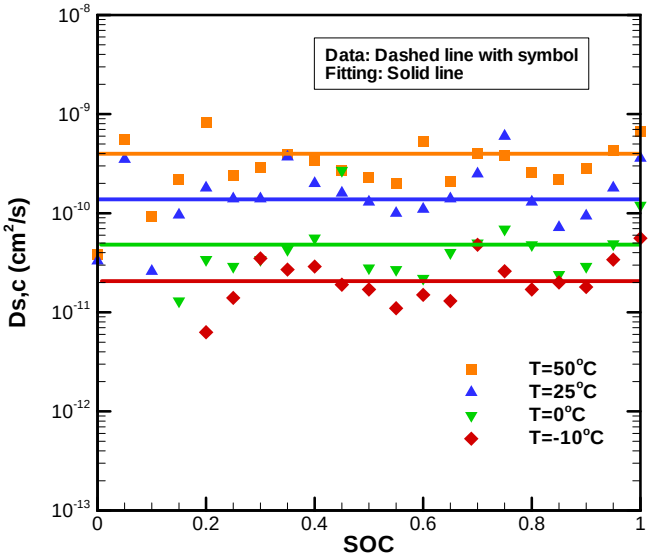

(a)

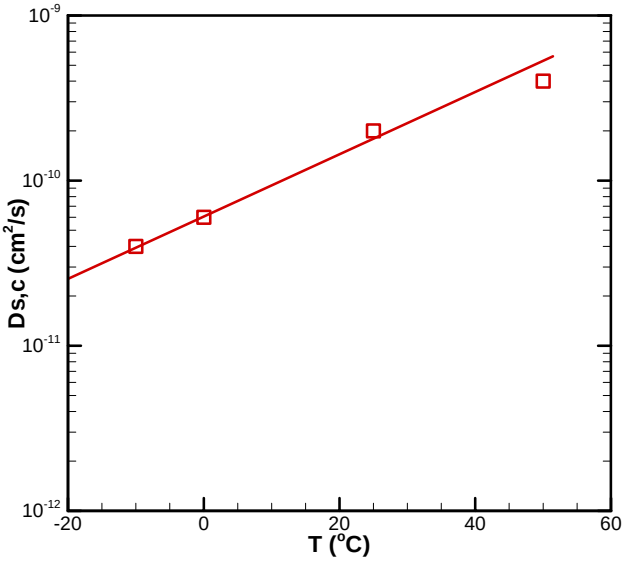

(b)

Figure 4.9: Li diffusion coefficient of the positive electrode as functions of (a) SOC and (b) chamber temperatures. (Kwon and Wang, 2010)

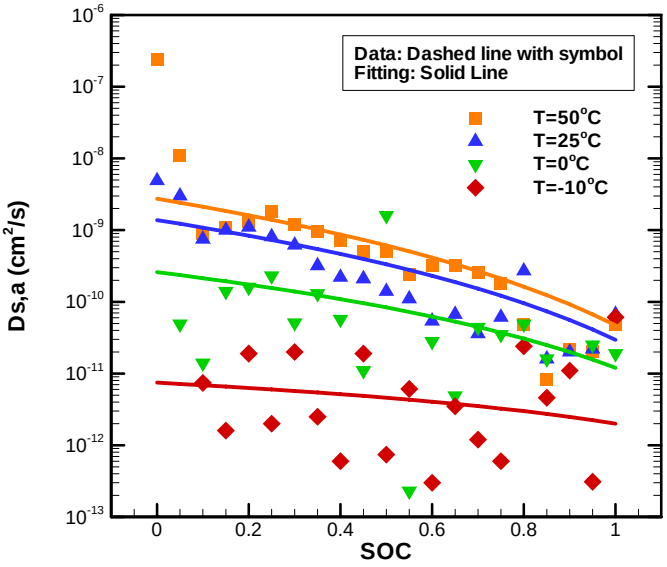

(a)

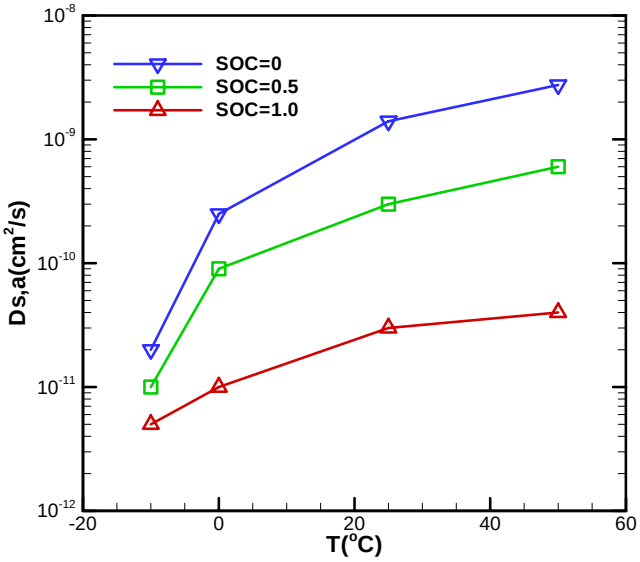

(b)

Figure **4.10**: Li diffusion coefficient in the negative electrode as functions of (a) SOC and (b) chamber temperatures.(Kwon and Wang, 2010)

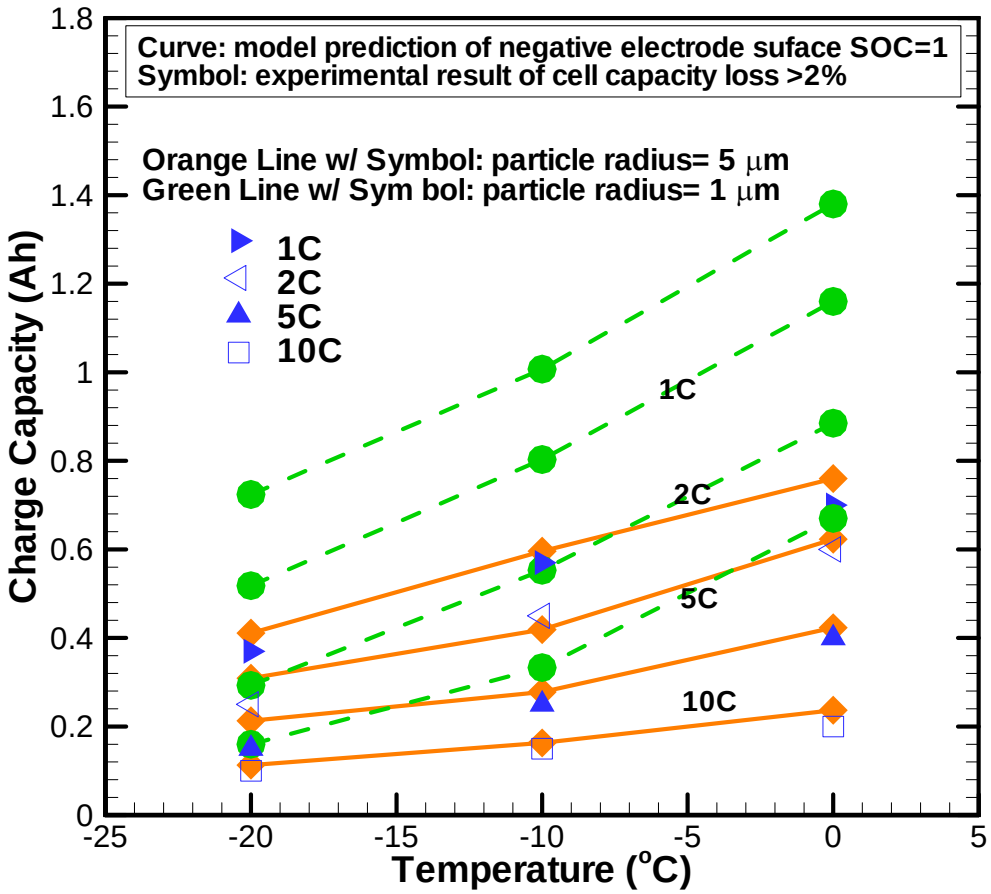

Figure **4.11**: Model prediction of onset condition for Li deposition on the negative electrode at different chamber temperatures with the negative electrode particle radius is reduced to 1/5 of the original value (dashed line with symbol). As comparison, the model prediction of the original case is also shown (which is the case shown in Figure **4.2**).

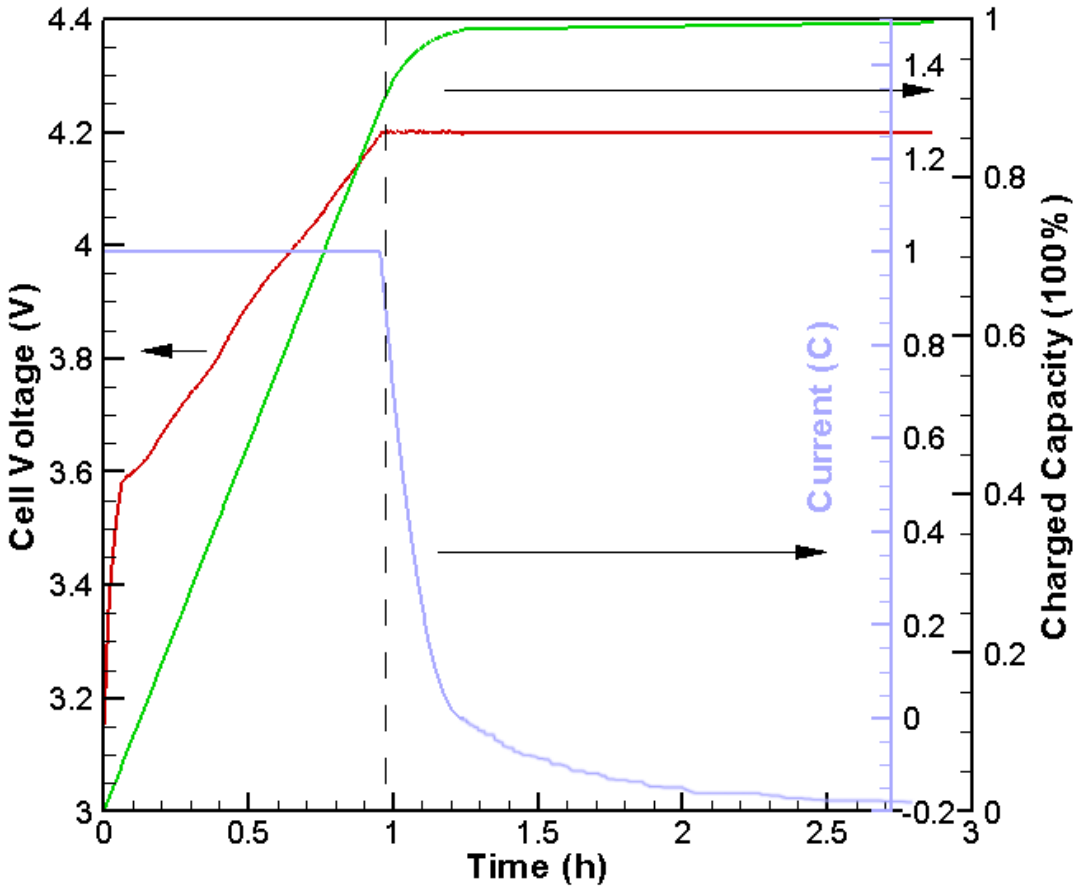

Figure **4.12**: Schematic of the conventional charging protocol.

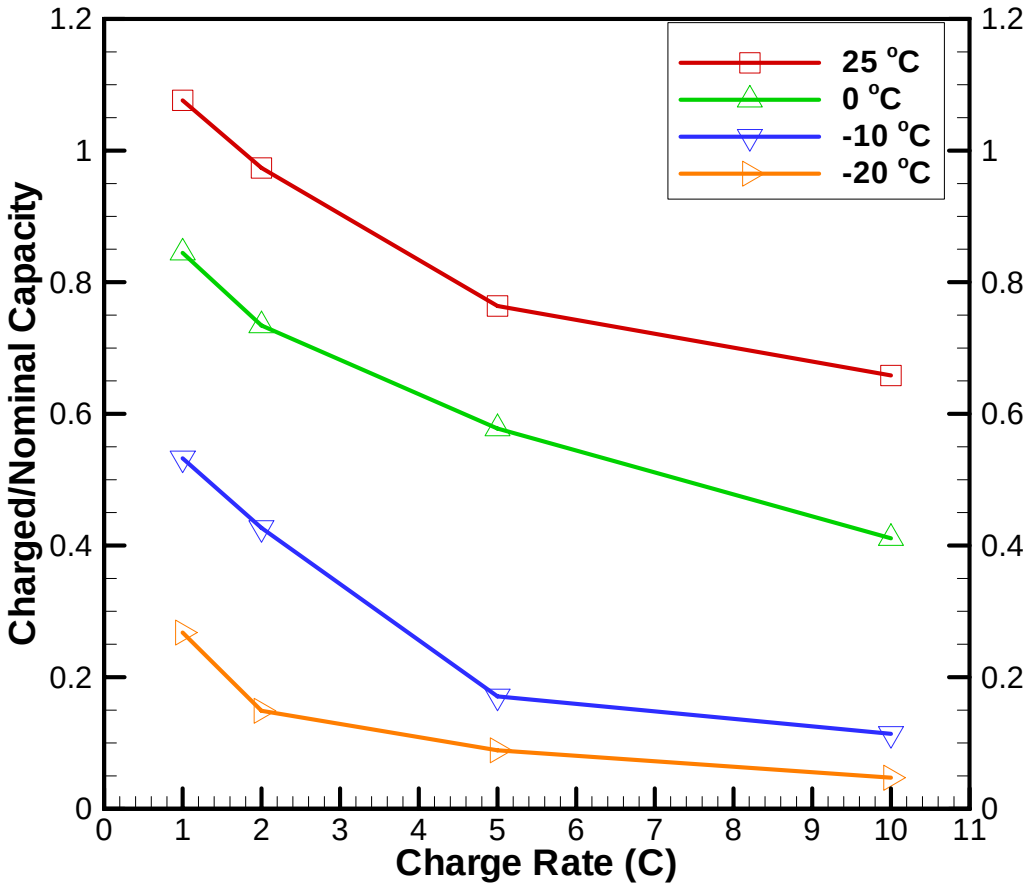

Figure 4.13: Charged capacity/nominal capacity vs. charge rate at different chamber temperature for constant current charge when surface SOC of the negative electrode particle reaches unity (simulation result).

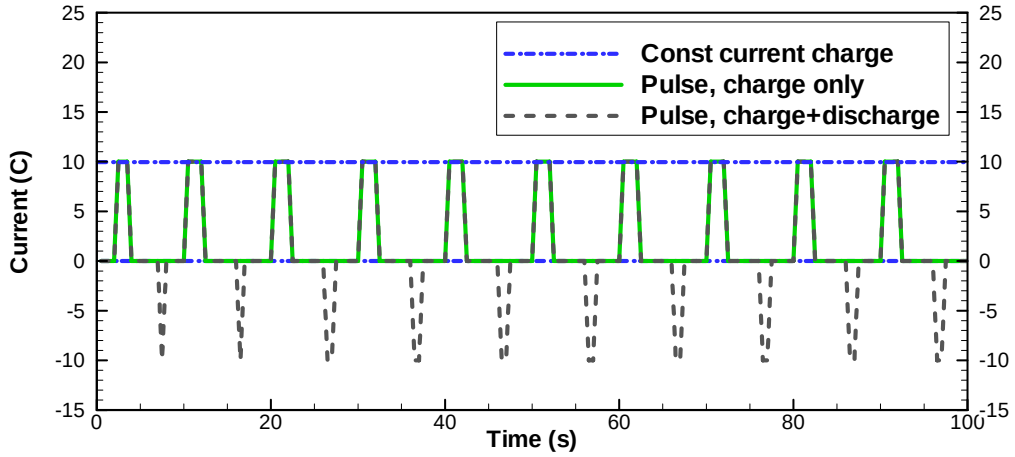

(a)

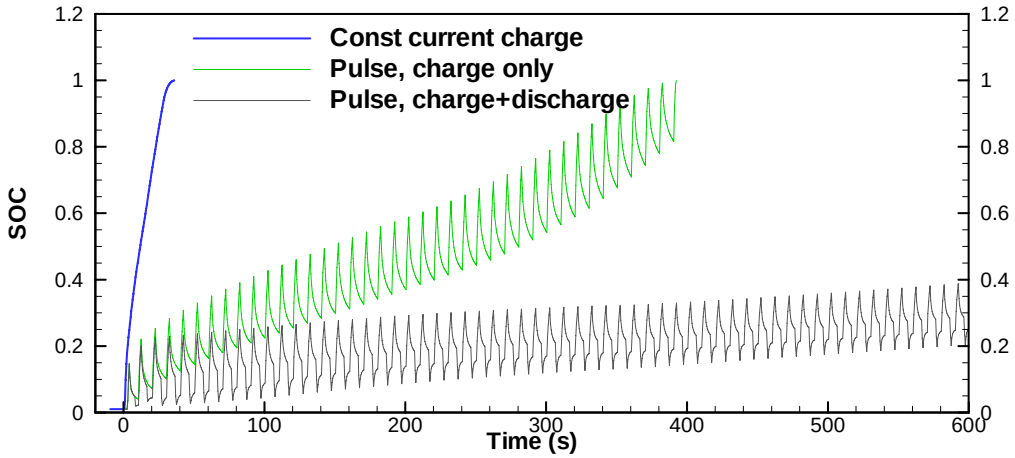

(b)

Figure 4.14: (a) Current profiles of three charge protocols, (blue) constant 10C current charge, (green) pulse 10C charge and (grey) pulse 10C charge + 10C discharge. (b) Monitoring the SOC of the negative electrode particle surface close to the separator.

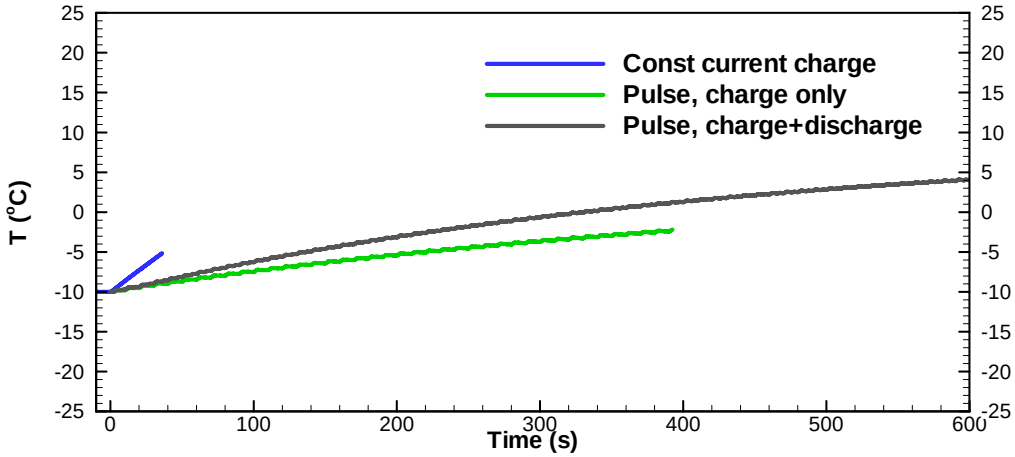

(a)

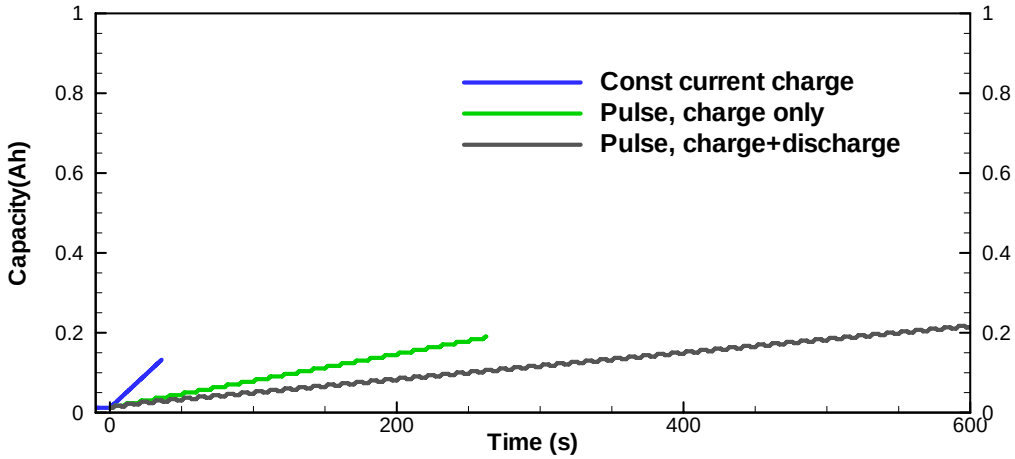

(b)

Figure 4.15: (a) Cell temperature and (b) charged capacity under the three different charge protocols.

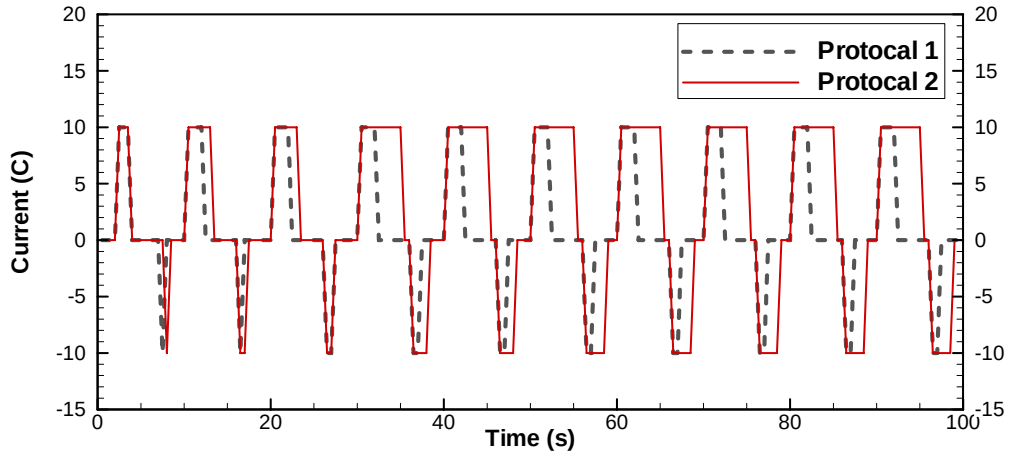

(a)

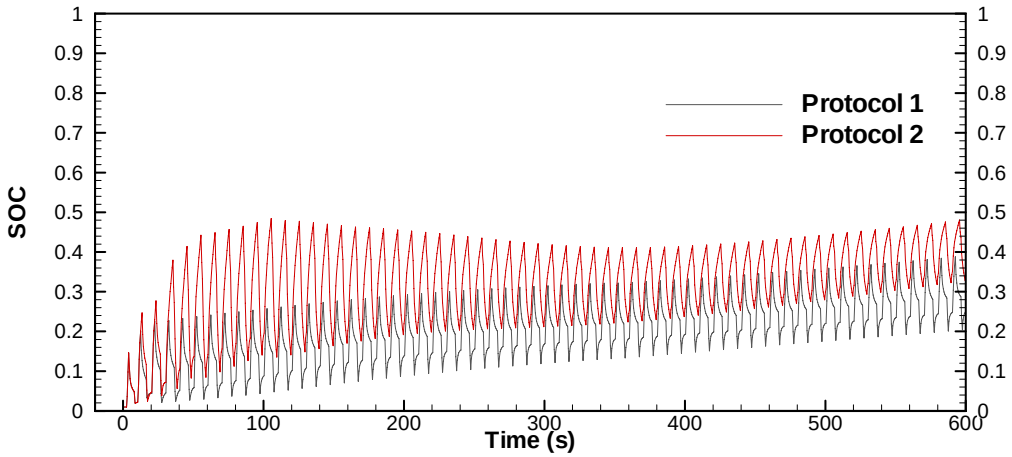

(b)

Figure 4.16: The original protocol (protocol 1) and improved protocol (protocol 2). (a) Current profile and (b) SOC of the negative electrode particle surface close to the separator.

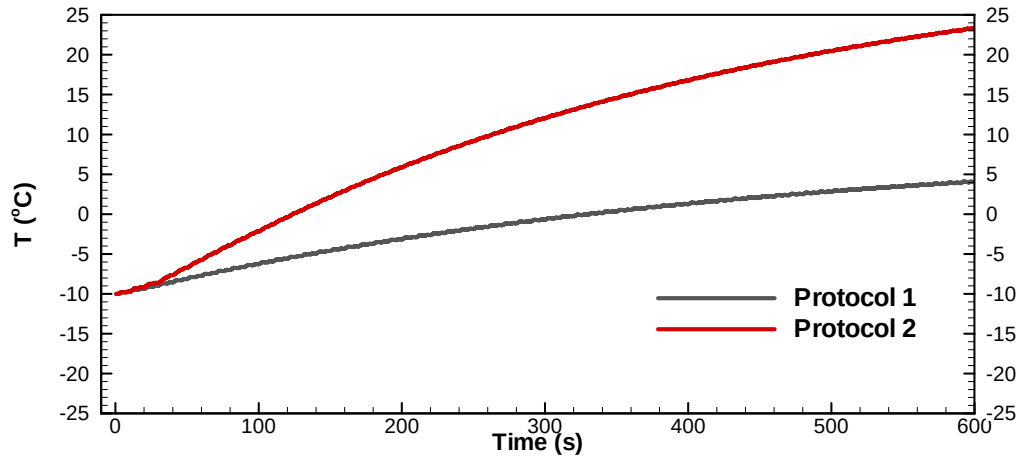

(a)

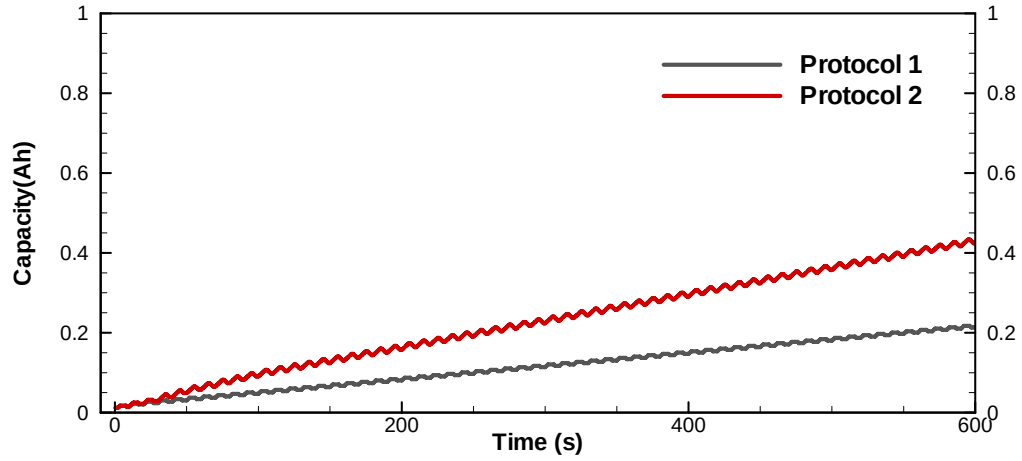

(b)

Figure 4.17: (a) Cell temperature and (b) charged capacity under the two protocols.

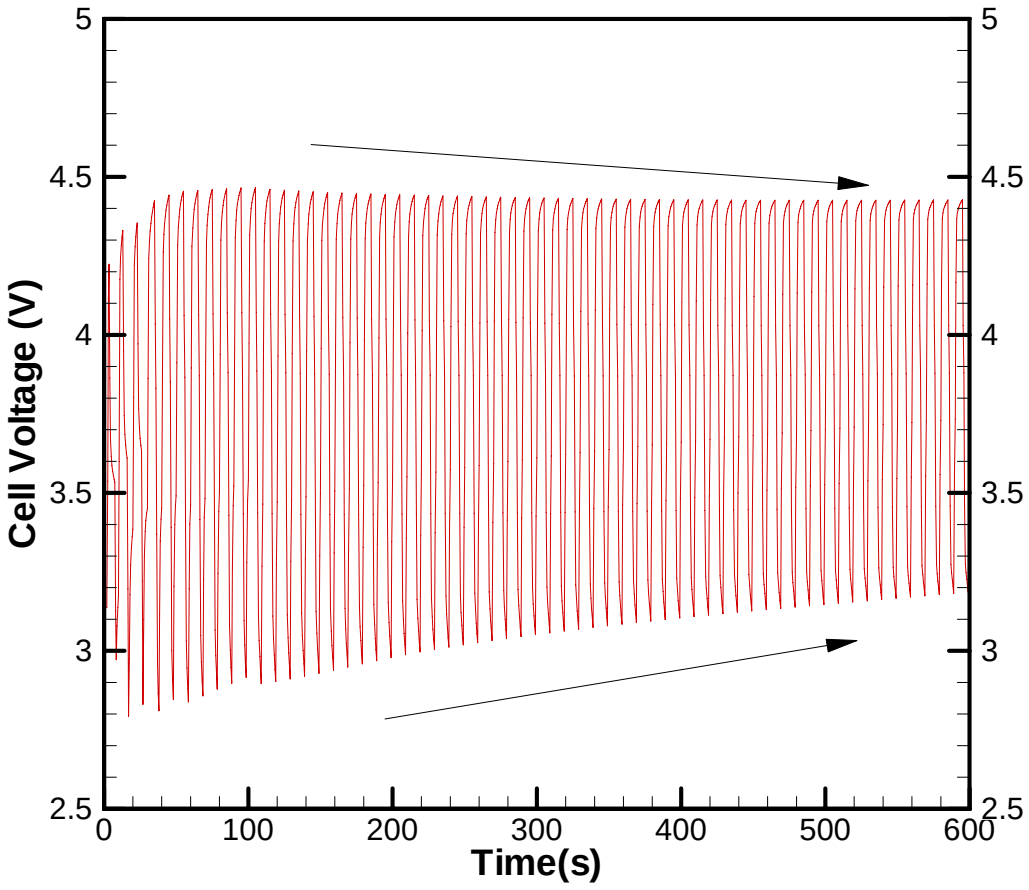

Figure **4.18**: Cell voltage for protocol 2.

Fig. **4.19**

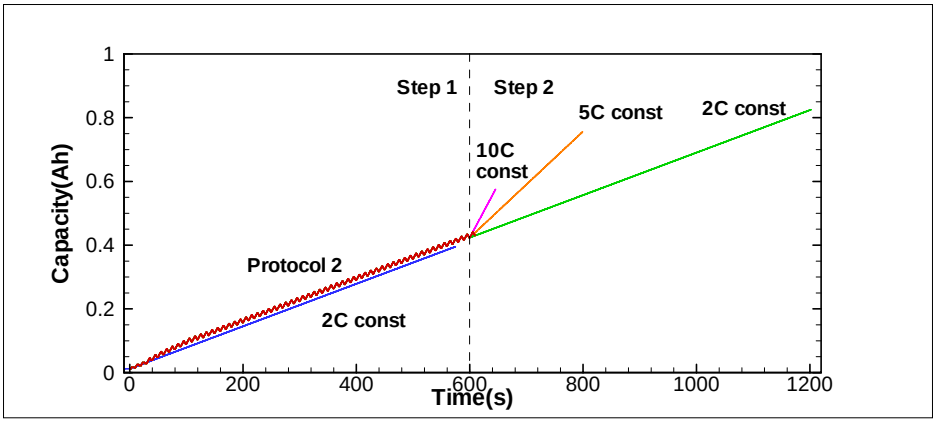

(a)

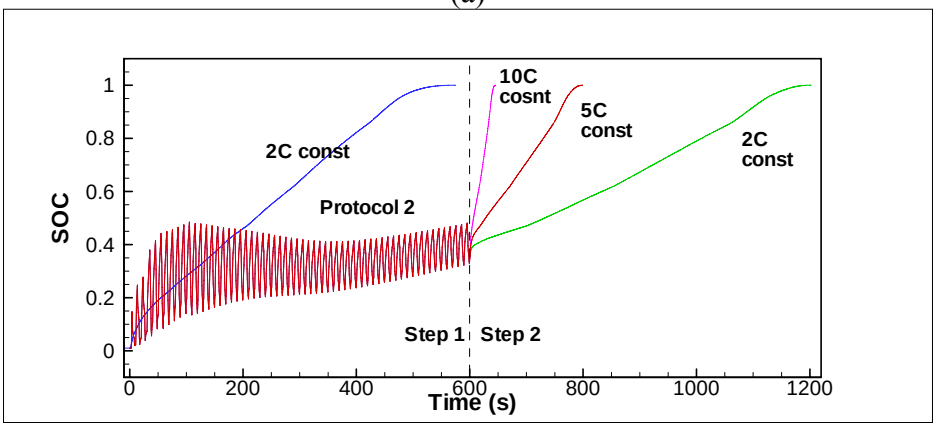

(b)

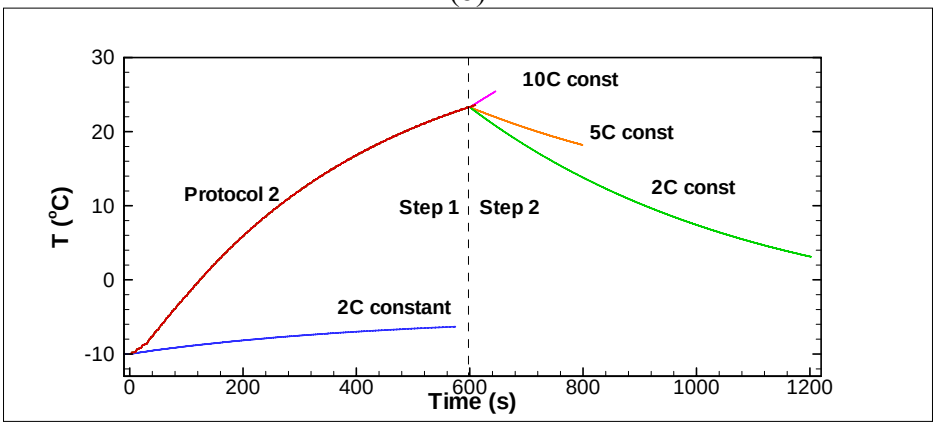

(c)

Figure **4.19**: Comparison of protocol 2 with 2C constant current charge.

Chapter 5

Li-Ion Battery Degradation Model

5.1 Side Reactions

Side reactions that occur at the two electrodes—the main reasons that cause Li-ion battery aging—are summarized and listed in the following sections.

5.1.1 Carbon-Based Anode

1. An SEI film forms during the first charge of a fresh cell through electrolyte reduction, causing one-time irreversible capacity loss due to the consumption of active lithium. An ideal SEI film, formed in good electrolyte systems such as electrolyte solutions based on EC-DMC or EC-DEC, allows lithium intercalation-deintercalation to occur smoothly with stable charge-discharge cycles[13,21,22,23,24].

2. Electrolyte reduction might still occur during subsequent cycling or storage, leading to further capacity loss and impedance growth. This is mostly due to carbon expansion/contraction during lithium intercalation/deintercalation processes [61]. In other words, further electrolyte reduction is greatly related to the area of exposed lithiated carbon.

5.1.2 Lithium Nickel Oxide-Based Cathode [43] [44][45][46][47]

1. On the surface of active particles, a thin $Li_xNi_{1-x}O$ or NiO-type layer exists which exhibits different electronic and ionic properties from the bulk oxide. In addition, an ill-defined mixture of organic and inorganic material surface was observed, and Li^+ ions from the electrolyte must either diffuse, migrate, or both through this film to react electrochemically at the oxide surface. Hence, the NiO-type layer and surface film significantly increase the electrode impedance.

2. The thickness of NiO-type layer and surface film was estimated to be on the order of tens of nanometers and was not significantly changed during cycling [**46**].

3. The interfacial impedance increase might be due to a degradation of the ionic pathway for Li^+ ions between the electrolyte in the electrode pores and the bulk oxide active material, which could result from changes in the electrolyte/oxide interfacial structure, composition and/or properties, causing a reduction in the exchange current density at the interface, a decrease in the ionic conductivity of surface films and a lowering of the lithium diffusion coefficient through these films [**45**].

5.2 The Degradation Model with Degradation in Each Electrode

From the above discussion, anode SEI film development involves several steps and might consist of two different layers, while surface film on the nickel oxide-base

electrode might also consist of two different layers as observed by experiments. It is, however, difficult to distinguish the different layers and thus almost all the current degradation models treat the surface film as a one-layer homogeneous film. In this study, the one-layer electrolyte film will also be adopted in the degradation model.

Based on current knowledge of respective aging mechanisms in each electrode and common assumptions in the current degradation models, the following assumptions of our degradation model are made.

General Assumptions

1. No gas phase is present.

2. Concentrated binary electrolyte is assumed [79,93].

3. Charge transfer kinetics follows Butler-Volmer equation.

4. Ionic species transport in the electrolyte is by migration and diffusion only.

5. The active electrode materials are made up of spherical particles of uniform size.

6. Cell temperature is uniform spatially.

7. No interaction between the side reactions at the anode and the cathode.

8. All the capacity loss and impedance rise are attributed to surface film formation, which consumes active lithium and increase electrode resistance, on the anode and the cathode. Other degradation processes are neglected.

Anode Side Reaction Assumptions

9. Surface film (i.e. SEI film) thickness increases due to side reaction product precipitate.

10. SEI film porosity, conductivity and diffusion coefficient do not change during aging.

Cathode Side Reaction Assumptions

11. Surface film thickness change during aging is negligible.

12. Surface film porosity, conductivity and diffusion coefficient are changed during aging due to precipitate of side reaction product which blocks the pores of existing surface film.

Assumptions 1 through 10 are commonly used in degradation models in the current literature for simulating aging of the anode, while assumptions 11 and 12 are introduced in the present work to simulate aging of the cathode according to the degradation phenomena summarized at the beginning of this chapter.

The surface film model is shown in Fig. **5.1**, and the different mechanisms of film formation on the two electrodes are shown in Fig. **5.2**. The actual surface film development in each electrode is much more complicated and may involve both thickness increase and porosity decrease. Moreover, at the anode, graphite exfoliation and graphite particle cracking due to solvent co-intercalation might also occur and lead to a rapid degradation of the electrode. Therefore, we should be very cautious when interpreting experiments using the model.

Nevertheless, the degradation model introduced above will make the first attempt to capture the typical aging phenomena at each electrode uncovered by various experiments.

5.2.1 Surface Film Description

Lithium diffusion and migration through the electrolyte film are described by conservation of Li^+ and conservation of charge equations, respectively

Eq. 5.1

$$\frac{\partial c_{ef}}{\partial t} = \frac{\partial}{\partial r}\left(D_{ef} \frac{\partial c_{ef}}{\partial r} \right) \tag{5.1}$$

and

Eq. 5.2

$$\frac{\partial}{\partial r}\left(\kappa_{ef} \frac{\partial \phi_{ef}}{\partial r} \right) + \frac{\partial}{\partial r}\left(\frac{\kappa_{ef}^{D}}{c_{ef}} \frac{\partial c_{ef}}{\partial r} \right) = 0 \tag{5.2}$$

Where the assumption is made that the side reaction is taking place only at the solid/electrolyte film interface.

Using impedance model parameters determined in the work of Dees *et al.*[46] for a fresh cell, we estimate characteristic times of the three diffusion layers and double layer capacitance to be:

- Bulk active material diffusion: $\tau_s = R_s^2 / D_s = 300$ s
- Electrolyte film diffusion: $\tau_{ef} = \delta_{ef}^2 / D_{ef} = 50$ ms
- Double layer capacitance: $\tau_{dl} = R_{ct} C_{dl} = 4$ μs

A charge/discharge model like the present performance model and experimentation is impossible to decouple surface layer phenomena faster than ~1 Hz. An analytical impedance model, valid for small perturbations about a given state of charge, is better suited to the task of resolving of surface dynamics across disparate time

scales and thus observing electrolyte film layer growth/property changes during life-cycle testing. For this reason, EIS data is proposed to be collected at regular intervals during accelerated life-cycle testing.

5.2.2 Determination of Parameters

Different treatments are carried out for the anode and the cathode surface films. For the anode SEI film, steady state of surface film concentration and potential gradients are assumed. For the electrolyte film layer at the cathode, the property ($D_{ef,c}$, $\kappa_{ef,c}$,) changes as a function of side reaction rates. And the capacities of both electrodes change with cycling ($c_{s,lost}$).

In the electrodes, assume the electrolyte film layers are formed by irreversible side reactions at the solid/electrolyte interface,

Eq. 5.3 for anode

$$\begin{aligned} &2EC + 2e^- + 2Li^+ \rightarrow (CH_2OCO_2Li)_2 \downarrow + C_2H_4 \uparrow \\ &EC + 2e- + 2Li+ \rightarrow Li_2CO_3 \downarrow + C_2H_4 \uparrow \end{aligned} \quad [5] \qquad (5.3)$$

And Eq. 5.4 for cathode

$$EC + LiNiO_2 \rightarrow NiO_2 - CH_2CH_2OCO_2Li \downarrow \quad [40] \qquad (5.4)$$

reducing/oxidizing EC to generic species. Note that in realty there may be several side reactions taking place at the solid/electrolyte film interface; the properties of actual generic species should be determined by experimental studies. The reactions proceed with Tafel kinetics at rate

Eq. **5.5** for anode

$$j_a^{\ s} = -a_{s,a}^s i_{0,a}^s \exp\left[-\frac{\alpha_c^s}{RT}(\phi_s - \phi_{e,s} - U_a^{\ s})\right] \quad (5.5)$$

Eq. **5.6** for cathode

$$j_c^{\ s} = a_{s,c}^s i_{0,c}^s \exp\left[\frac{\alpha_a^s}{RT}(\phi_s - \phi_{e,s} - U_c^{\ s})\right] \quad (5.6)$$

where U_a^s and U_c^s are the equilibrium potentials for side reactions at the anode and the cathode, respectively. The Bulter-Volmer kinetic expression was used to describe the overall charge transfer process occurring across the electrode/electrolyte interface. At each electrode, the local volumetric charge transfer current density was defined based on Li^+ insertion/deinsertion and side reaction current densities as shown in Fig. **5.16**.

Solid phase conservation equations (Li and e^-) will use modified source term $j^{Li} + j_a^{\ s}$ (for the andoe) or $j^{Li} + j_c^{\ s}$ (for the cathode). Total active lithium lost to side reaction at each electrode is

Eq. **5.7**

$$c_{s,lost}^s = \frac{1}{nF\varepsilon_s L}\int_0^t\int_0^L j^s(x,\tau)\,dx\,d\tau \quad (5.7)$$

The anode electrolyte film layer thickness may be expected to increase according to rate law

Eq. **5.8**

$$\frac{\partial \delta_{ef,a}}{\partial t} = \frac{j_a^{\ s}}{a_{s,a}nF}\frac{M_a^{\ s}}{\rho_a^{\ s}} \quad (5.8)$$

where M^s and ρ^s are the molecular weight and density of the product species, respectively.

At the cathode, the film porosity, $\varepsilon_{ef,c}$, is gradually reduced during cycle life using a rate law similar to Eq. **5.8** .

Eq. **5.9**

$$\frac{\partial \varepsilon_{ef,c}}{\partial t} = -\frac{j_c^{\,s}}{a_{s,c} nF} \frac{M_c^{\,s}}{\rho_c^{\,s}} \tag{5.9}$$

The electrolyte film conductivity and diffusion coefficient may be adjusted during aging from reference values using Bruggeman-type relations

Eq. **5.10**

$$\begin{aligned} \kappa_{ef} &= \kappa_{ef}^{ref} (\varepsilon_{ef,c})^{\tau} \\ D_{ef} &= D_{ef}^{ref} (\varepsilon_{ef,c})^{\tau} \end{aligned} \tag{5.10}$$

Furthermore, the change of available active surface area (for both Li^+ insertion/deinsertion and side reactions) per unit volume due to side reaction product precipitation can be expressed as [**70**,**103**],

Eq. **5.11**

$$a_c = a_c^{\,0} \left[1 - \left(\frac{\varepsilon_{ef,c}^0 - \varepsilon_{ef,c}}{\varepsilon_{ef,c}^0} \right)^{\xi} \right] \tag{5.11}$$

where $a_c^{\,0}$ and $\varepsilon_{ef,c}^0$ are initial values, and ξ is an experimentally determined parameter used to describe the morphology of the precipitate, with the large values indicating needle shaped deposits whereas small values represent flat deposits. In total, degradation model parameters U^s, i_o^s, (M^s / ρ^s), and ε_{ef} will be chosen to fit experimentally measured changes in $D_{ef,c}$, $\kappa_{ef,c}$, δ_{ef}, and $c_{s,lost.}$

To summarize, the degradation model will treat the anode SEI film with constant film parameters except for thickness. In contrast, the cathode surface film parameters (except for thickness) in the model are considered to be life dependent (i.e. $D_{ef,c}$, $\kappa_{ef,c}$,), as is the electrode capacity loss ($c_{s,lost}$) of each electrode. These life-dependent parameters will be obtained from EIS model interpretation of EIS data obtained from aged cells at regularly selected cycle numbers.

5.3 Experimental

The aging test of this study was done by Kwon and will be briefly introduced here. Please also check Zhang and Wang's 2009 paper for more details of the test procedure.

The accelerated cycling at 5C rate between 3.0 and 4.2 V were performed at 50°C. Five cells aged to five different cycle numbers of 1000, 2000, 3000, 4000 and 5000. For individual measurement of each electrode, these cells were subsequently opened at fully discharged state and assembled into a three-electrode cell holder with a lithium-metal reference electrode. Capacity characterization and EIS of the fresh and cycled cells were carried out on three-electrode cells at 25°C.

5.4 Result and Discussion

The experimental data will be analyzed to obtain necessary information which can be used to adjust the degradation model parameters. All the experimental data used in this present work were measured in a chamber with fixed temperature of 25°C except the accelerated aging test which is carried out at 50°C. So as are the parameters used in the model and simulation results.

5.4.1 Electrode Analysis

The OCPs of the electrodes are very important information for models. The SEI film layer resistance influence only fast dynamics and may be ignored for slow charge/discharge. Important information thus can be obtained by analyzing the evolution of the electrode OCP during cycling. In our experiment, the electrode OCPs of the fresh and cycled cells were obtained by GITT (galvanostatic intermittent titration technique) method which is carried out by discharging a fully charged cell using 1C-rate for 3min and then rest for 30mins till the cell voltage reaches the lower cut-off voltage. One advantage of this method is that Li diffusion coefficients in the two electrodes can also be obtained at the same time.

OCPs of the fresh and cycled cells from the experiment are plotted in Fig. **5.4**. During a discharge process, Li^+ ions are inserted into the positive electrode so the y value in $Li_y(NiMnCo)_{1/3}O_2$ increases and the positive electrode potential decreases. Toward the

end of discharge, the electrode potential drops rapidly and the discharge process ends as the cell voltage reaches the lower cut-off voltage. As shown in this figure, the positive electrode OCP shrinks as cycling which means the capacity of the electrode reduces and less lithium can be inserted into the electrode. This electrode capacity reduction may be due to the composite damaged (active material loss) or reaction area blockage on the positive electrode.

On the negative electrode, during a discharge process, Li ions are de-intercalated from the negative electrode so the x value in Li_xC_6 decreases and when the x value is low, the electrode potential increase rapidly and the discharge process ends as the cell voltage reaches the lower cut-off voltage. In general, the negative electrode of a Li-ion battery is made to have larger capacity than the positive electrode to avoid Li deposition that can occur during high current charging. This is also true for the cells used in this present work. In Fig. **5.4b**, the negative electrode potential never exceeds the value of 0.4V for all the cases, which means the negative electrode is not the limiting electrode during cycling. On the other hand, the maximum negative electrode potential of the cycled cell is about the same value as the fresh cell (about 0.4V). This suggests that at the end of the discharge, x value is not high either; otherwise, the potential curve will be flatter.

Besides OCP, EIS data of the positive and negative electrodes is also important information. Equivalent circuit is always used for fitting the impedance spectra of an electrode as shown in Fig. **5.5**. In the figure, R_0 is the uncompensated ohmic resistance of the electrolyte and electrode, etc. C_{SEI} and R_{SEI} are capacitance and resistance of

surface film. C_{DL} and R_{CT} are double-layer capacitance and resistance, and W_d is Warburg diffusion impedance related to Li diffusion in the electrode particles.

The impedance spectra of the two electrodes shown in Fig. **5.6** were obtained with an AC amplitude of 5 mV over the frequency range from 50KHz to 0.005Hz. The impedance spectra of the positive electrode show only one clear semi-circle which is generally attributed to the charge transfer and a low-frequency tail. The impedance spectra of the negative electrode is however unclear and unstable. Roughly, it shows two semi-circles. The left higher frequency semi-circle is generally attributed to the SEI layer and the right lower frequency semi-circle is attributed to the charge transfer impedance. The low-frequency tail is barely seen.

In Fig. **5.6**, the "bulk resistance", R_0 of the two electrodes does not change appreciably. The diameter of the semi-circle of the positive electrode represents the charge transfer resistance between the electrolyte and the active material. It increases as cell ages and nearly doubles after 2000 cycles and quadruples after 5000 cycles. As is mentioned earlier in this chapter, Li^+ ions from the electrolyte must either diffuse, migrate, or both through the surface film to react electrochemically at the oxide surface. Upon aging, the interfacial impedance increase might result from changes in the electrolyte/oxide interfacial structure, composition and/or properties, causing a reduction in the exchange current density at the interface. On the negative electrode, the charge transfer and SEI layer resistance of the negative electrode are relatively small and show almost no change upon aging. It seems that in this case, the SEI layer is quite stable during cycling.

The low-frequency tail of the positive electrode keeps the same shape during cycling, which indicates Li diffusion impedance change is very small in the bulk of solid particle. The experimental measurement also shows that the Li diffusion coefficients of the two electrodes are in the same order of magnitude for fresh cell and cell after 5000 cycles.

To summarize, as the cell ages, the charge transfer resistance of the positive electrode shows clear increase and is the primary contributor to cell impedance rise.

5.4.2 Model Validation

Based on the above analysis, the summary of assumptions for degradation model is proposed.

On the negative electrode,

1. SEI layer forms and grows due to electrolyte reduction.
2. The structure of the carbon electrode is not damaged on aging and is not the limiting electrode.
3. SEI grows (getting thicker) on aging and causes active lithium loss and slight impedance rise.

While on the positive electrode,

1. Surface film forms and grows (possibly) due to electrolyte oxidation.

2. Active material loss and/or being blockage from reaction causes impedance rise and thus capacity fade by reducing the capability of the positive electrode to deliver and accept lithium.
3. Separation of oxide particles due to surface film growth makes Li^+ ion diffusion and migration more difficult, leading to impedance rise.

Both OCP and EIS data analysis suggest that the positive electrode is dominating the cell degradation so the first step of developing degradation model is to interpret the aging mechanism on the positive electrode.

The OCP curves of the positive electrode shown in Fig. **5.4** were used as first estimation of the positive electrode reaction area for the cycled cells. The surface film porosity was then calculated from Eq. **5.11**. And the other surface film properties can be calculated from Eq. **5.10**. These parameters were then implanted into the degradation model and constant C-rate discharge simulations were carried out. The results were then compared to the experimental data. Adjustments of the parameters were made to obtain a better match. After several adjustments, the surface film properties that match the experimental data can be determined. The next step is to determine the side reaction parameters. This is done by running the degradation model (at 50°C) for 5000 cycles and the model simulated film properties are compared to the estimated value. Adjustment is also needed in order to obtain a good match. The surface film parameters are shown in Table **5.1**.

The final simulated result of 1C to 10C discharge is plotted in Fig. **5.7** to Fig. **5.10** where experimental data is also plotted for comparison. Overall, the simulation result shows very good agreement with the experimental data.

The simulated result of 1C capacity change during cycling is shown in Fig.**5.11** and compared to the experimental data. Also plotted in the figure is the model simulated result of cell active lithium change during cycling. The 1C capacity reduced rapidly at the beginning of aging cycle. The drop is then slowed down during cycling. One of the reasons for this slowing down is that as the cell ages, the electrode impedance increases such that the period of one cycle is shortened, as is the side reaction time. The simulated active lithium loss is less than 1C capacity loss. This is because the cell performance reduction is also caused by cathode reaction area blockage and electrode surface film resistance growth.

Fig. **5.12** shows that the simulation result of the degradation model agrees well with the experimental data not only of full cell but also of the individual electrode.

In many model studies, the capacity loss is often attributed to the SEI layer formation on the negative or positive electrode, which actually is not able to catch the electrode performance after aging. To prove this, another simulation (after 1000 cycles) was carried out which attributes all the 1C capacity loss to SEI layer formation on the negative electrode. The result of this simulation is shown in Fig. **5.13**. Also shown is the previous simulation result from Fig. **5.12**. In Fig. **5.13b**, without considering the degradation on the positive electrode, the positive electrode potential does not drop dramatically at the end of discharge because there is enough composite in this electrode.

Fig. **5.13c,** the negative electrode potential increases dramatically at the end of discharge because there is not enough active lithium in the cell so that the x value in Li_xC_6 reaches the lower limit and the discharge ends. In this case, neither cell voltage nor the electrode potentials matches the experimental result which means that this treatment is not able to catch the experimentally observed phenomena in this present work.

The cell open circuit voltage (OCV), i.e. the difference of the OCPs of the two electrodes, is the key information for predicting the remaining battery capacity for most fuel gauge algorithms in many applications. However, the curve of OCV changes with battery degradation. Shown in Fig. **5.14** are the OCVs of a fresh cell and a cell after 1000 cycles. The SOC value of the plot is based on the fresh cell. One can see that for the same cell voltage at 3.6V, the SOC values of the two curves are quite different, which means the OCV of a fresh cell can not be used for predicting the remaining battery capacity for a aged cell. So how to estimate the OCV of an aged cell is very important topic in HEV applications. This is also the reason why a degradtion model should be able to predict the elctrode OCP evolution during aging. The appoach presented in this chapter may provide some useful ideas, however much more need to done in the future.

Shown in Fig.**5.15** are simulated results of the average surface film porosity, reaction area and lithium coefficient in the surface film on the positive electrode with cycling. All the degradations present the same tendency as the capacity loss, as discussed in Fig.**5.11**.

The transfer resistance, R_{CT} is related to the exchange current, I_0 by the following equation, valid for very low over-potential [**104**].

Eq. **5.12**

$$R_{CT} = \frac{RT}{nI_0F} \tag{5.12}$$

where R is gas constant, T is temperature, n is electron moles involved in the electrochemical process and F is Faraday constant. The exchange current can be expressed as $I_0 = i_0 a$ where a is the electrode active surface area (reaction area). The positive electrode reaction area is reduced as the cell ages and therefore the value of R_{CT} increases (Fig. **5.6a**). The changes of R_{CT} and reciprocal of exchange current during cycling are plotted in Fig.**5.15b**. Where the values are made dimensionless by divided by the initial values. It shows that within 2000 cycles the $1/I_0$ value agrees well with R_{CT} but after 2000 cycles R_{CT} increases faster than $1/I_0$. This deviation is probably due to other changes of the electrode such as structure change making the charge transfer more difficult.

Shown in Fig. **5.16** is the simulated result of the average surface film resistance on the electrode with cycling. The symbols are extracted from experimental EIS data. The anode surface film is small, shows light changes during cycling and is not the dominating degradation electrode as discussed.

Discharge capacity at different C-rates for fresh and cycled cells from model simulation and experimental data is plotted in Fig. **5.17**. Both model simulation and experimental data shows the same tendency that as cell ages, the cell rate capacity is greatly impacted. For the fresh cell, the difference of cell capacity under different C-rates is less than 0.08Ah, which means the cell has good performance even at high C-rates.

However this difference is increased to about 0.25Ah after 5000 cycles, which means as cell ages, the increase of the electrode impedance (mostly the positive electrode) greatly reduces cell power capability.

5.5 Conclusions

In this chapter, we introduce a Li-ion battery degradation model which considers the different surface film formation on the two electrodes due to side reactions during cycling. Assumptions of the respective aging mechanisms on the two electrodes are made based on the extensive experimental studies in this field. Such a model is proved to be able to simulate the cell performance for cell under the accelerated aging test (carried out by Kwon). The simulation results agree well with the experimental data.

By analyzing the OCP curves and EIS data of the two electrodes during cycling we found that aging on the positive electrode is the main reason causing cell capacity loss and impedance rise during the accelerated aging test for the cells used in the present work. During cycling, the positive electrode active material is lost and/or blockage from reaction which causes impedance rise and thus capacity fade by reducing the capability of the positive electrode to deliver and accept lithium. This mechanism is the key for a model to capture the degradation phenomena well. Otherwise, if the capacity loss is attributed to the SEI layer formation on the negative or surface film on the positive electrode, the model is not able to catch the real electrode performance after aging.

In the degradation model developed in this chapter, the aging processes can be simulated by the surface film evolution during aging. On the positive electrode, the deposit of side reaction product reduces the porosity of the surface film, which results in the reduction of reaction area. The conductivity and diffusion coefficient of the surface film are then reduced. The result is that the cell capacity is reduced due to the loss of active material and impedance is increased due to the increase of charge transfer resistance and diffusion resistance. On the negative electrode, the thickness of the surface film increases due to the side reactions. The negative electrode capacity is however not impacted during aging or at least it is not the limiting factor. This is consistent with the OCP analysis of the cycled cells.

In the future work, the degradation model will further help to prolong battery life through engineering and optimization in HEV applications.

Table **5.1**: Surface film parameters

Parameters	Anode	Cathode
U_a^s or U_c^s (V)	0.4 [a]	3.8 [a]
τ_{ef}	1.5 [a]	1.5 [a]
ξ	NA	0.8 [a]
$\varepsilon_{ef,0}$	0.5 [a]	0.5 [a]
$D_{ef,0}$ (cm^2/s)	10^{-12a}	10^{-12a}
$\kappa_{ef,0}$ (S/cm)	10^{-2a}	10^{-2a}
$\delta_{ef,0}$ (cm)	10^{-6a}	10^{-6a}
$i^s_{0,ref}$ (A/cm^2)	10^{-6a}	10^{-6a}
M^s / ρ^s (cm^3/mol)	50[a]	50[a]

[a] Assumed values

$_0$ Initial values

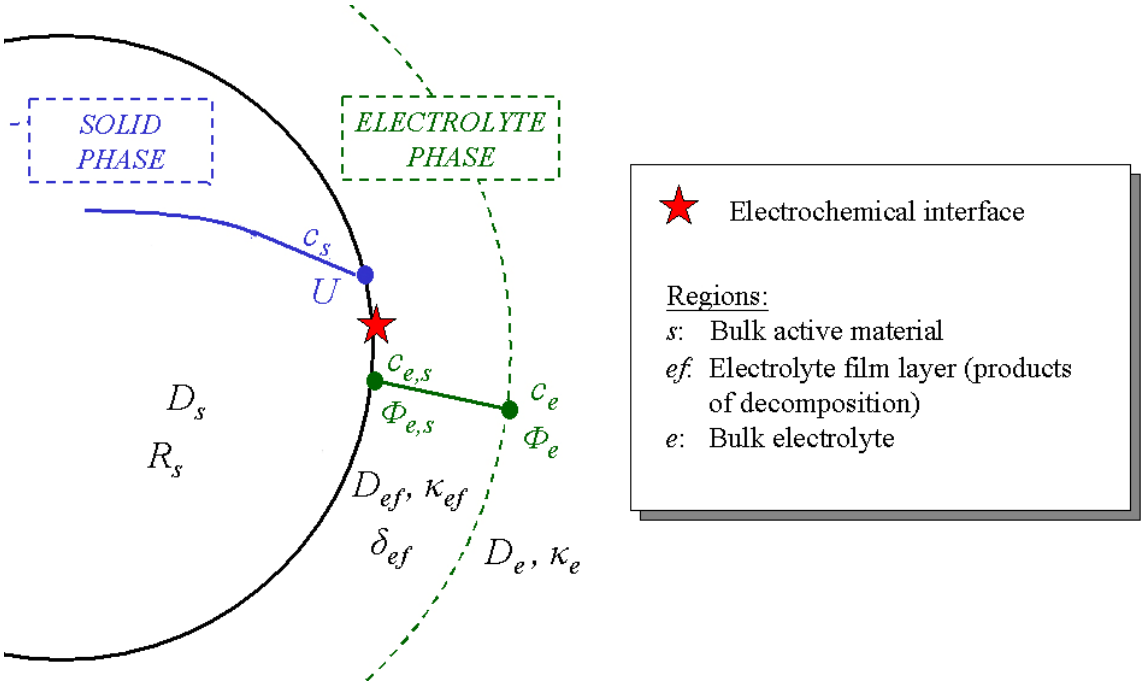

Figure 5.1: Illustration of solid particle and electrolyte surface layer model.

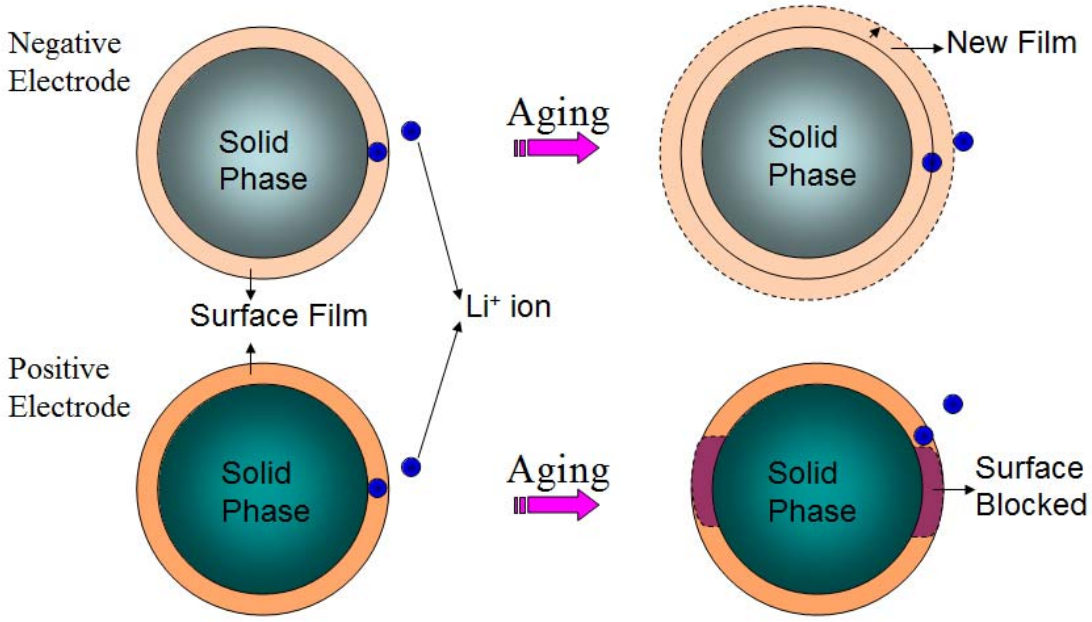

Figure 5.2: Different film formation mechanisms on the anode and cathode particle surfaces.

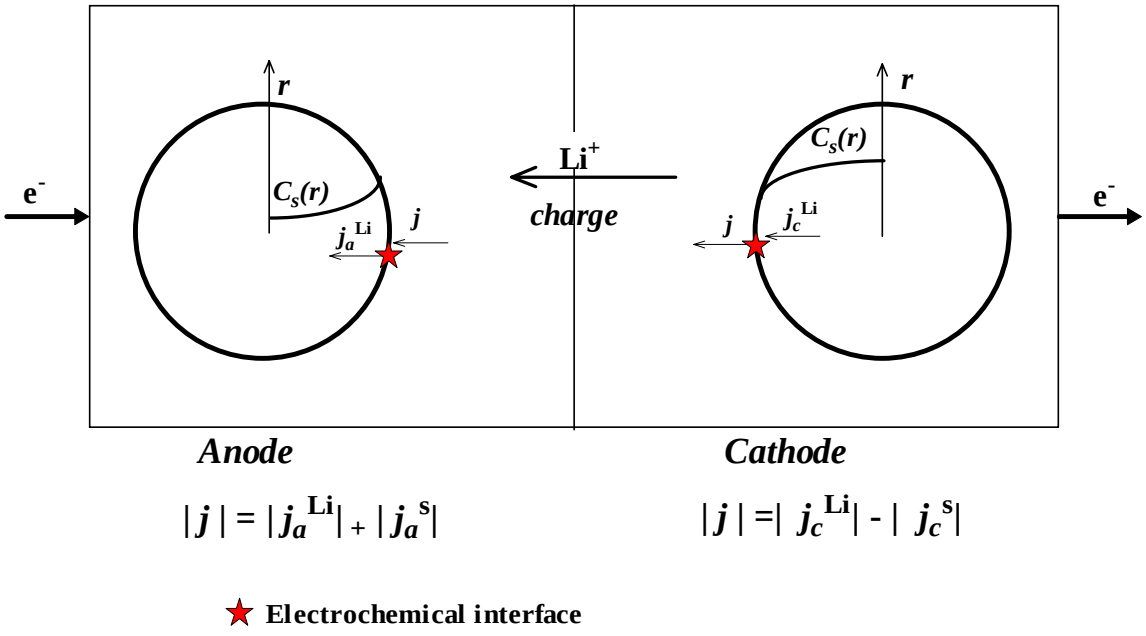

Figure 5.3: Schematic representation of local volumetric charge transfer current density related to Li^+ insertion/de-insertion and side reactions.

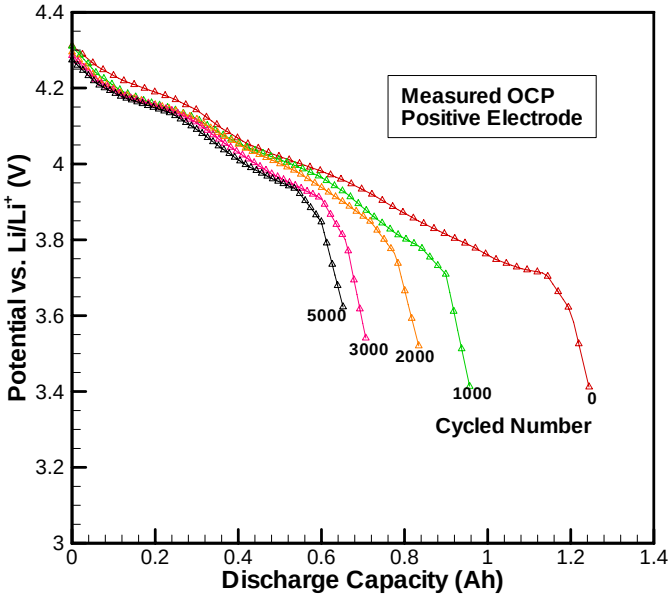

(a)

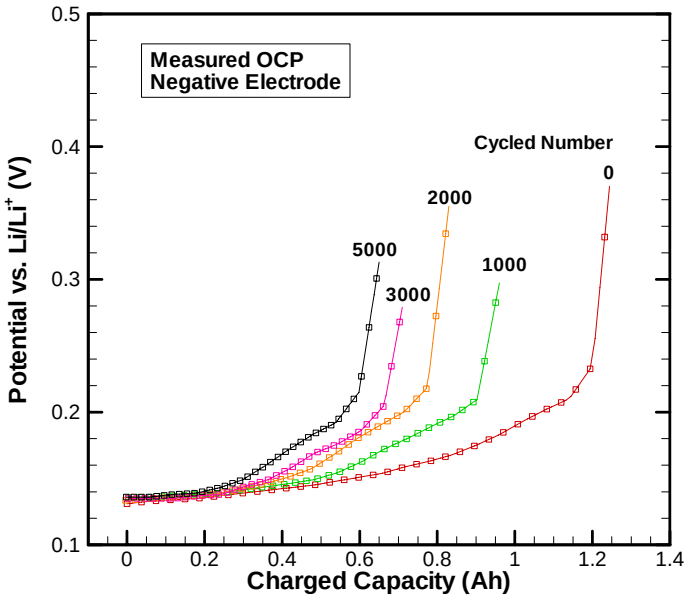

(b)

Figure 5.4: Experimentally measured OCPs of (a) cathode and (b) anode of the fresh and cycled cells at 25°C. (Kwon and Wang, 2010)

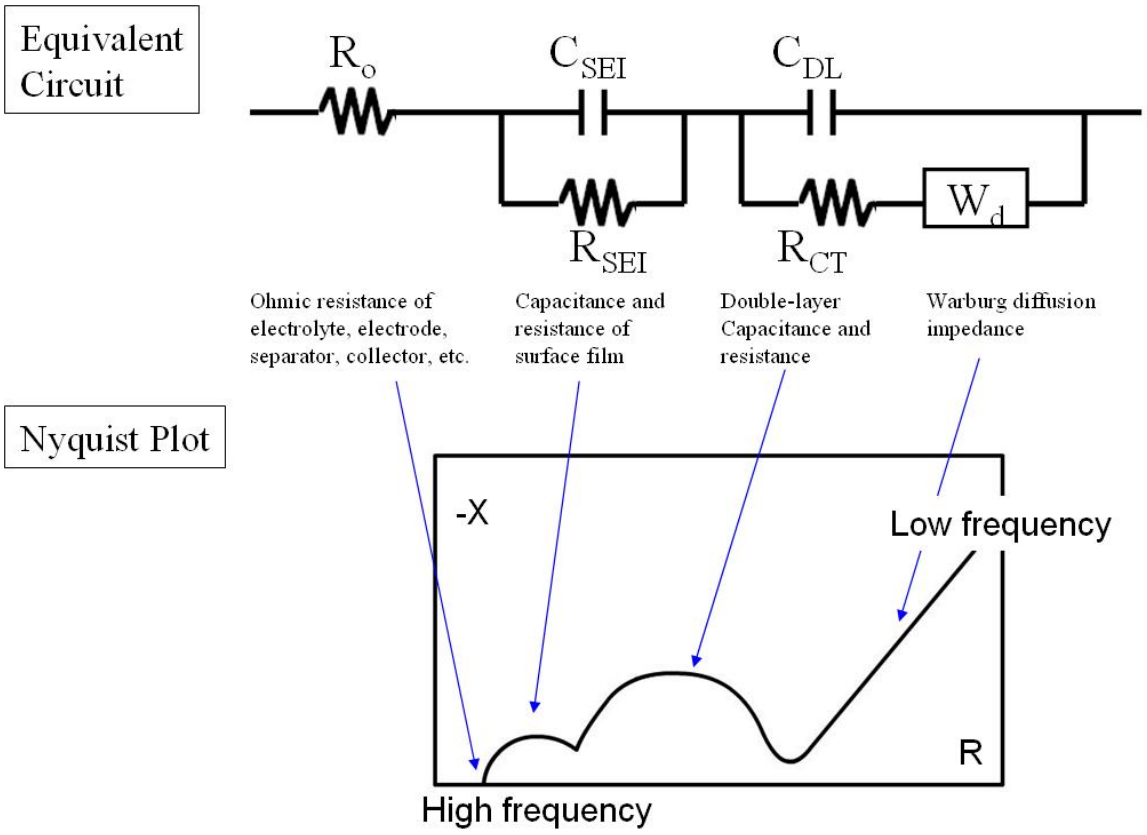

Figure 5.5: An equivalent circuit used for fitting the impedance spectra of an electrode.

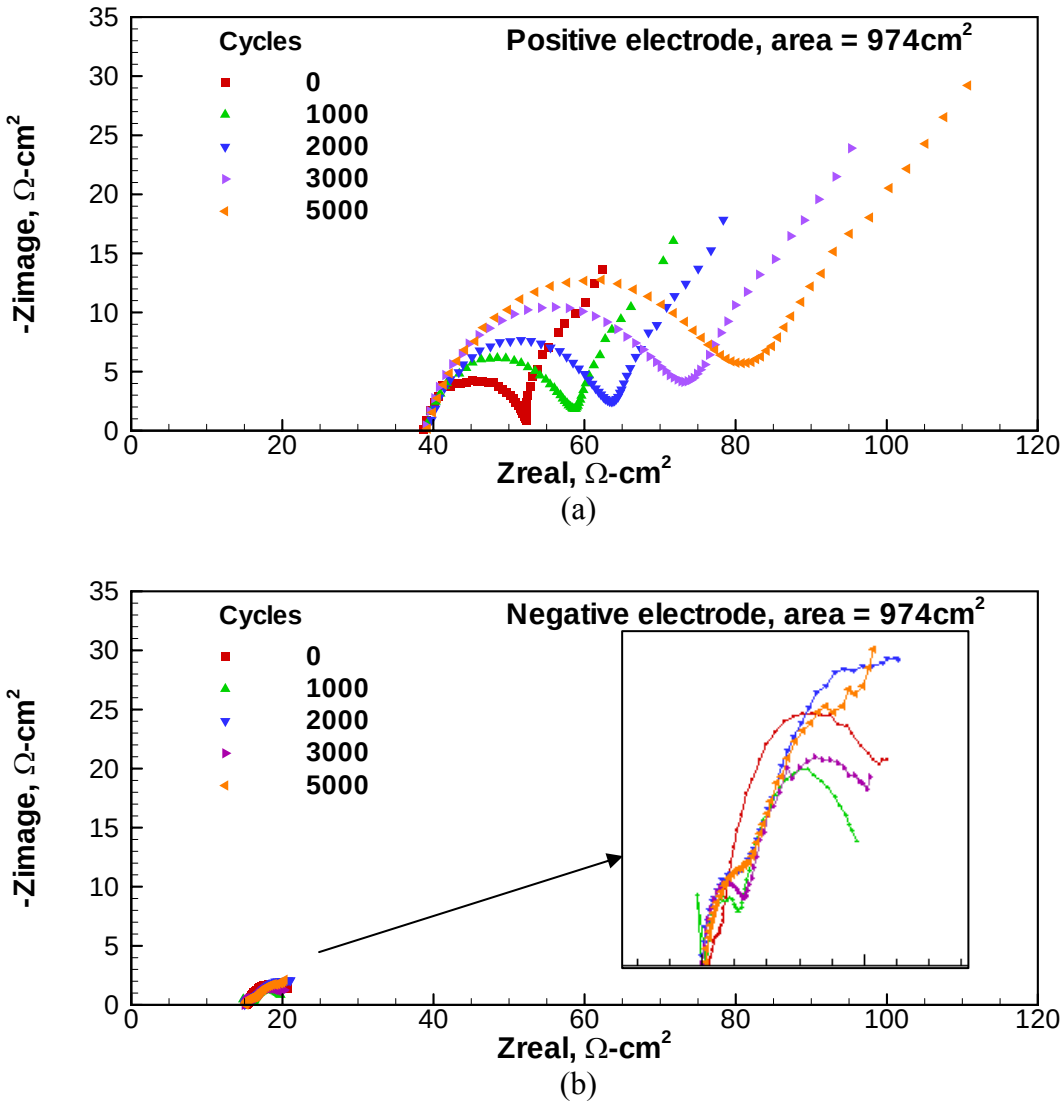

Figure 5.6: EIS data of the positive and negative electrodes from the fresh and cycled cells at 25℃. (Kwon and Wang, 2010)

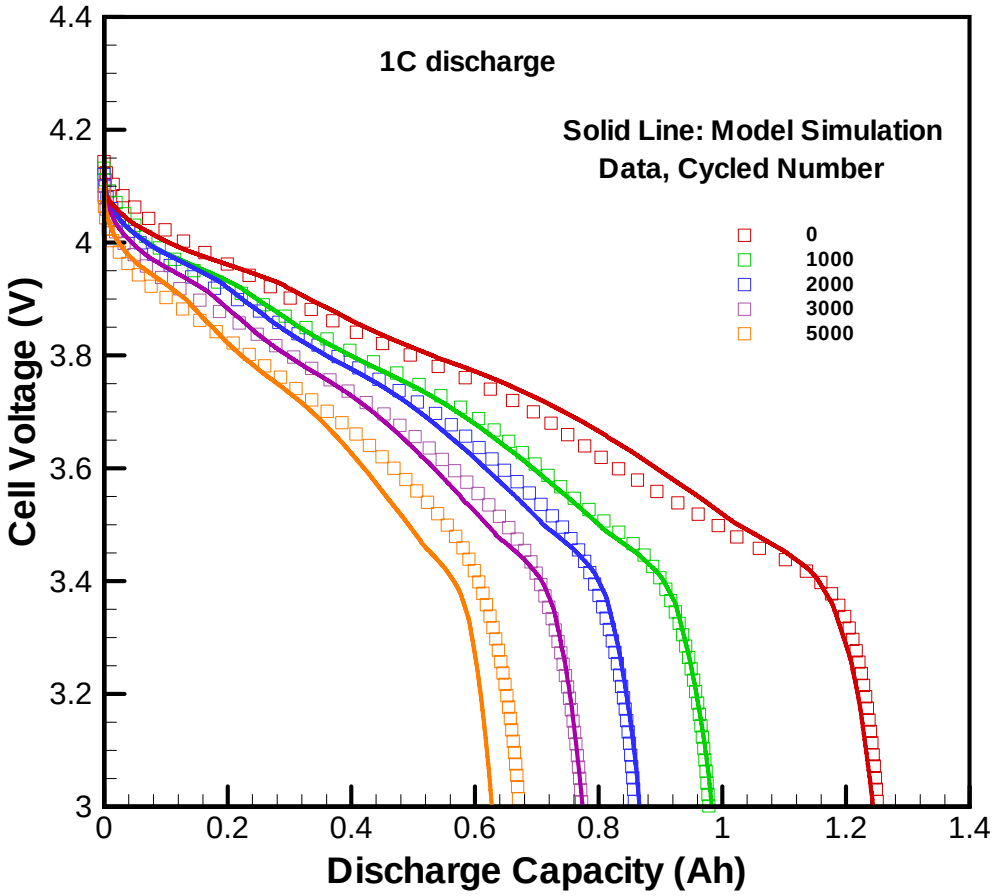

Figure 5.7: 1C discharges. Model simulation compared with experiment measured cell voltages for fresh and cycled cells at 25℃.

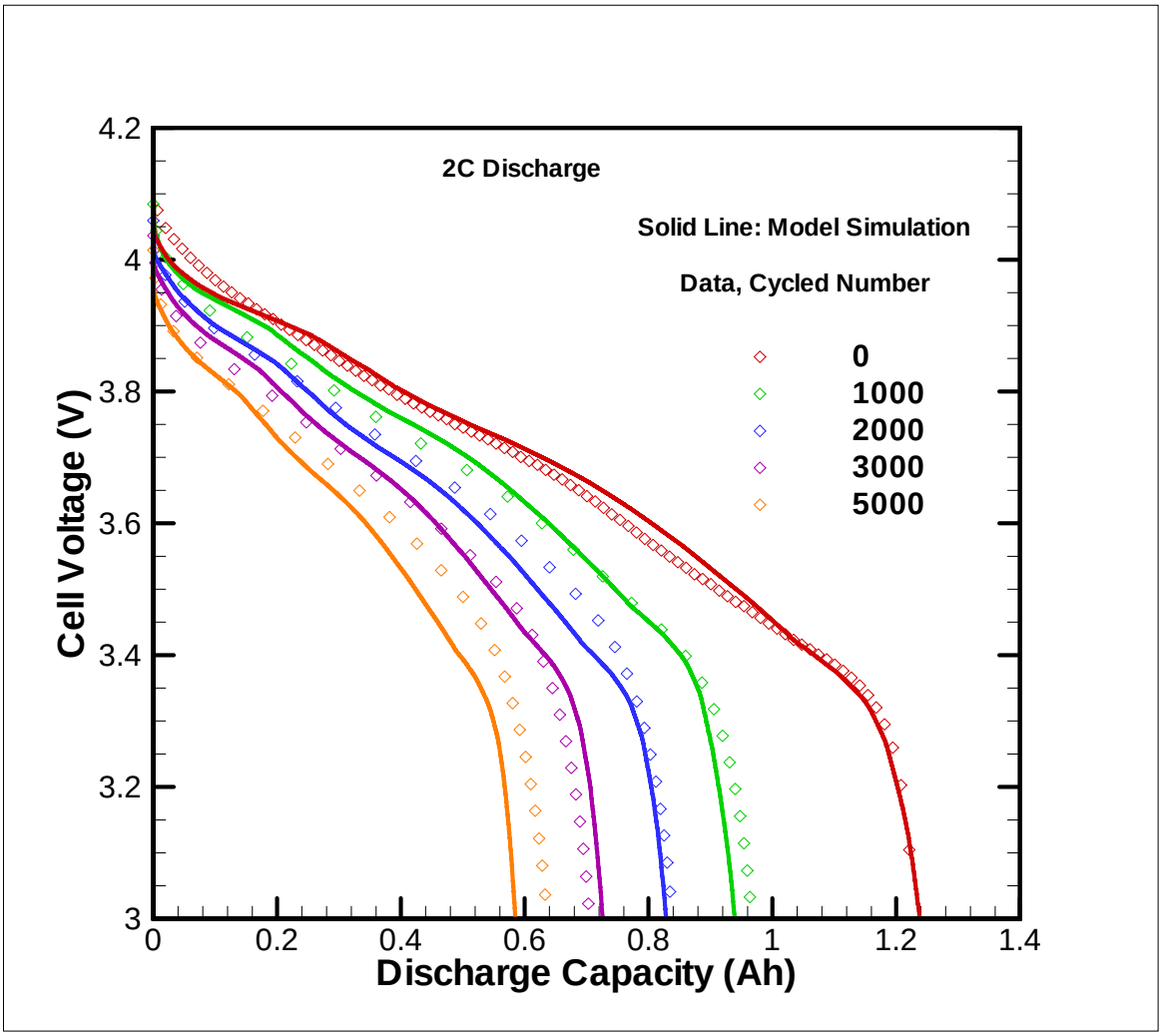

Figure **5.8**: 2C discharges. Model simulation compared with experiment measured cell voltages for fresh and cycled cells at 25°C.

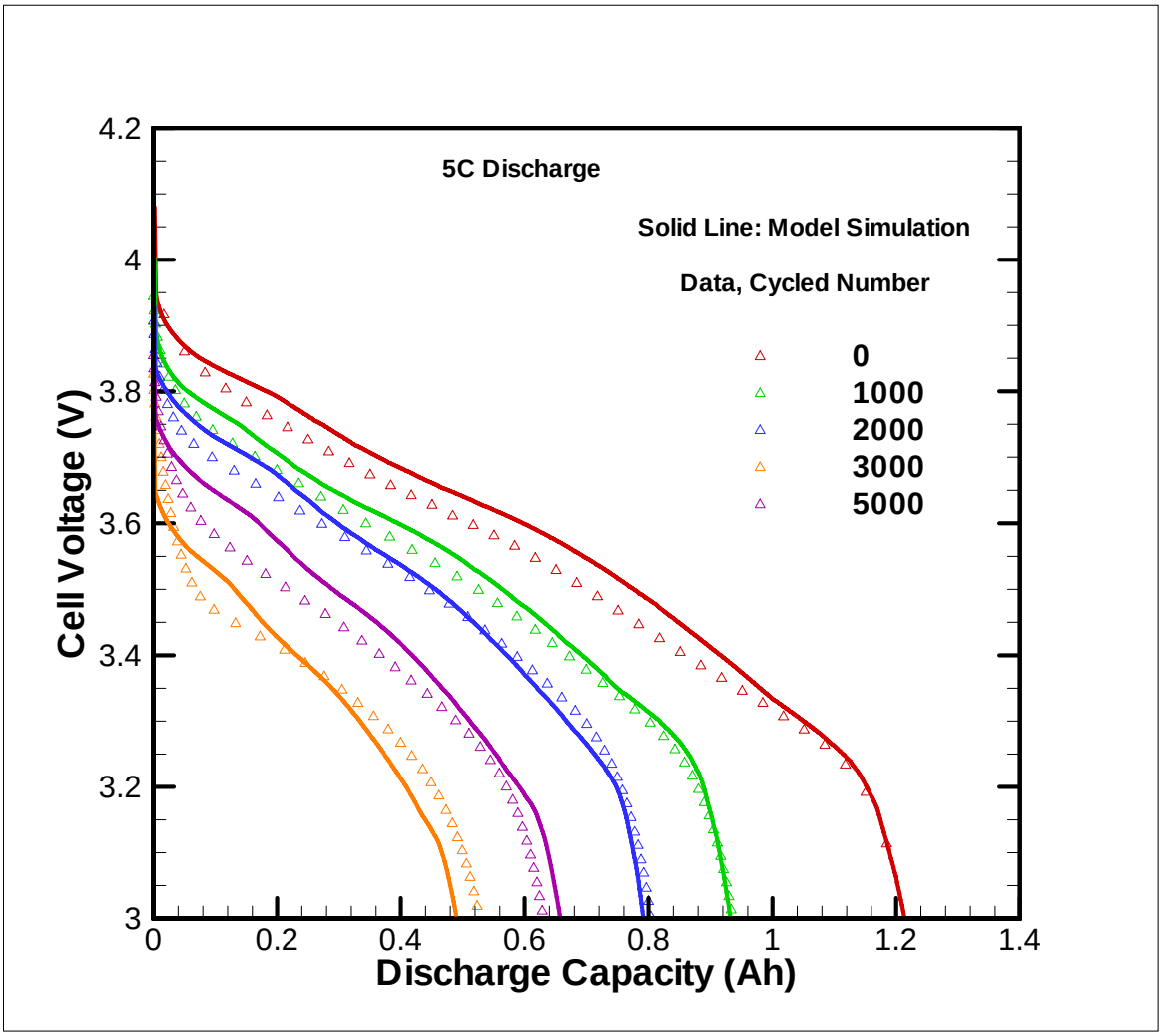

Figure **5.9**: 5C discharges. Model simulation compared with experiment measured cell voltages for fresh and cycled cells at 25°C.

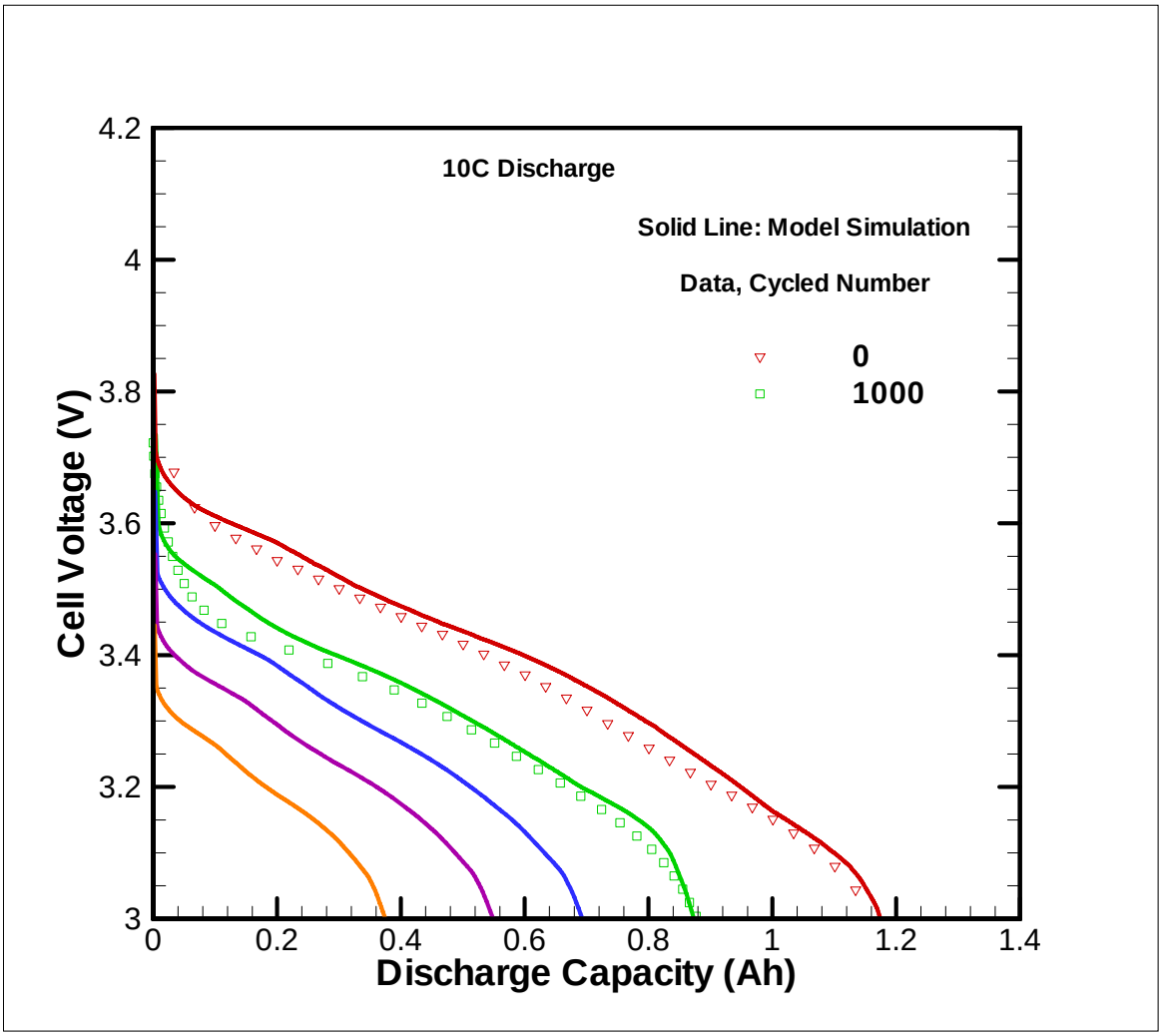

Figure **5.10**: 10C discharges. Model simulation compared with experiment measured cell voltages for fresh and cycled cells. The experimental data for 2000, 3000 and 5000 cycles are abnormal and not shown here at 25℃.

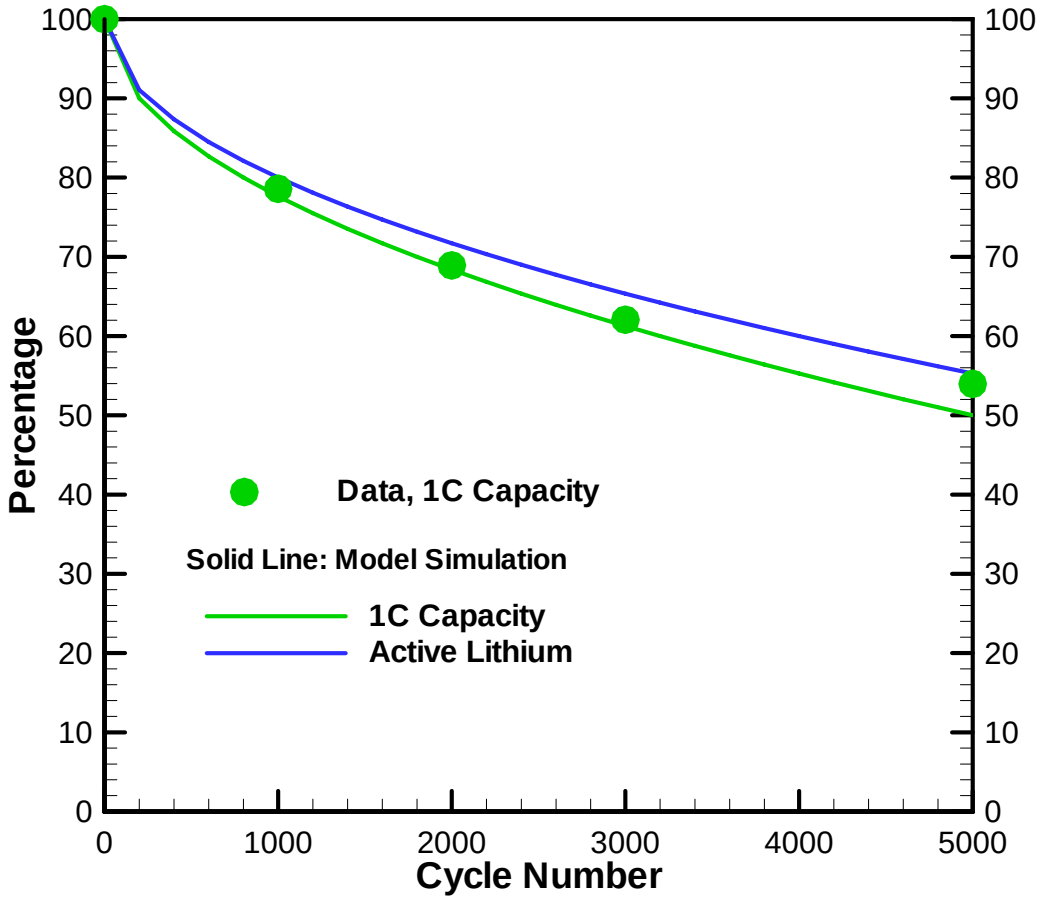

Figure 5.11: Measured and model simulated 1C capacity loss at 25°C. Also plotted is the model simulated active lithium loss.

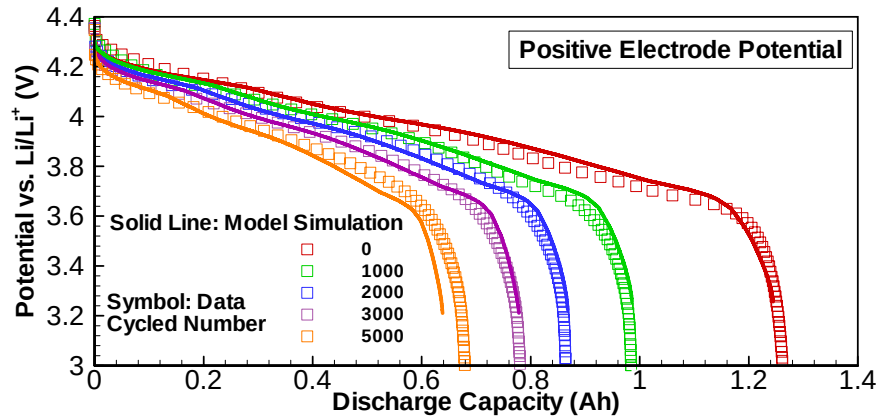

(a)

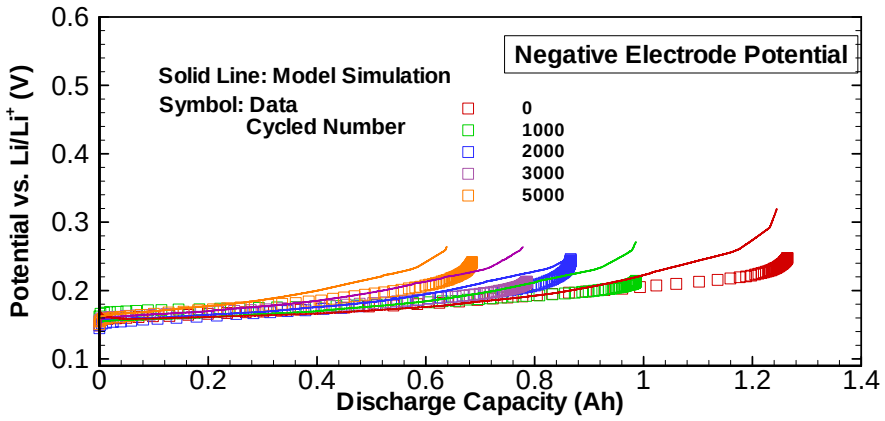

(b)

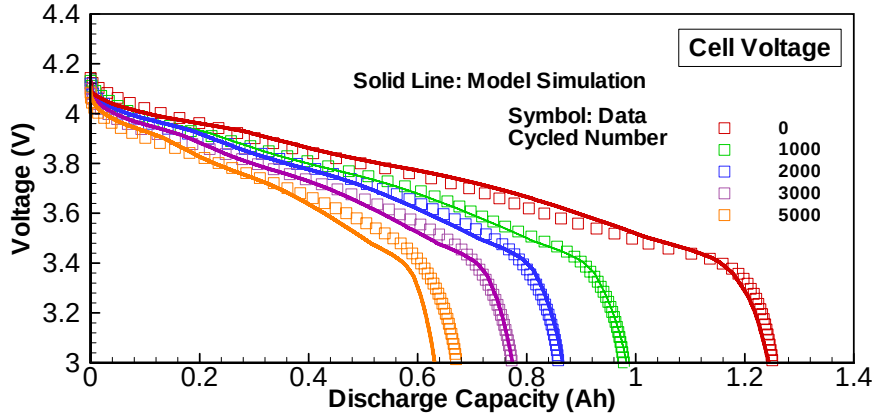

(c)

Figure 5.12: Comparison of model simulation and experimentally measured electrode potentials and cell voltage, 1C discharge at 25°C.

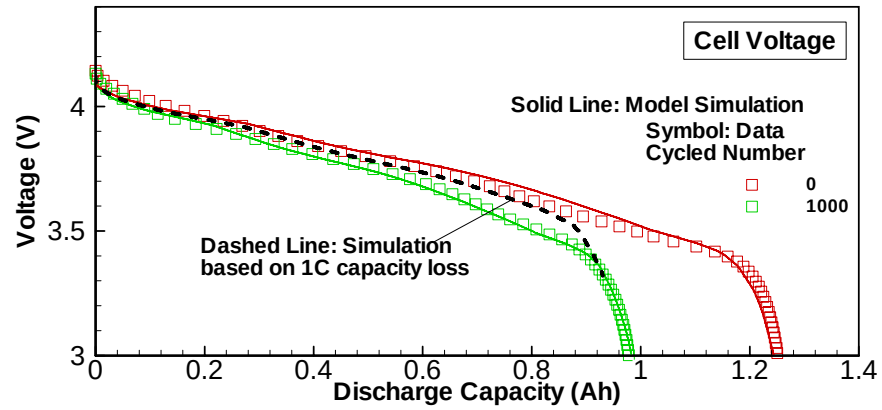

(a)

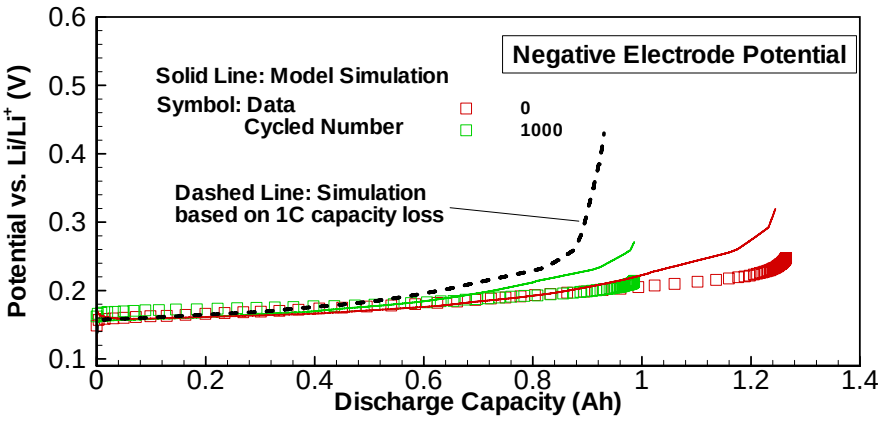

(b)

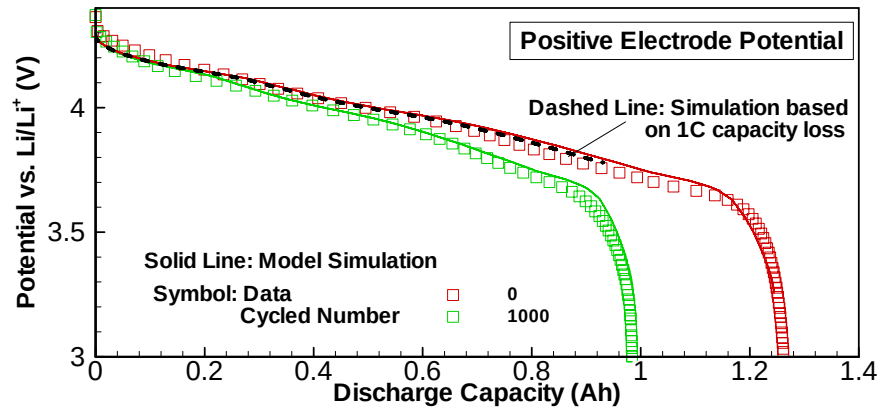

(c)

Figure 5.13: Added simulation based on 1C capacity loss and compare with the simulation result shown in Fig. 5.8.

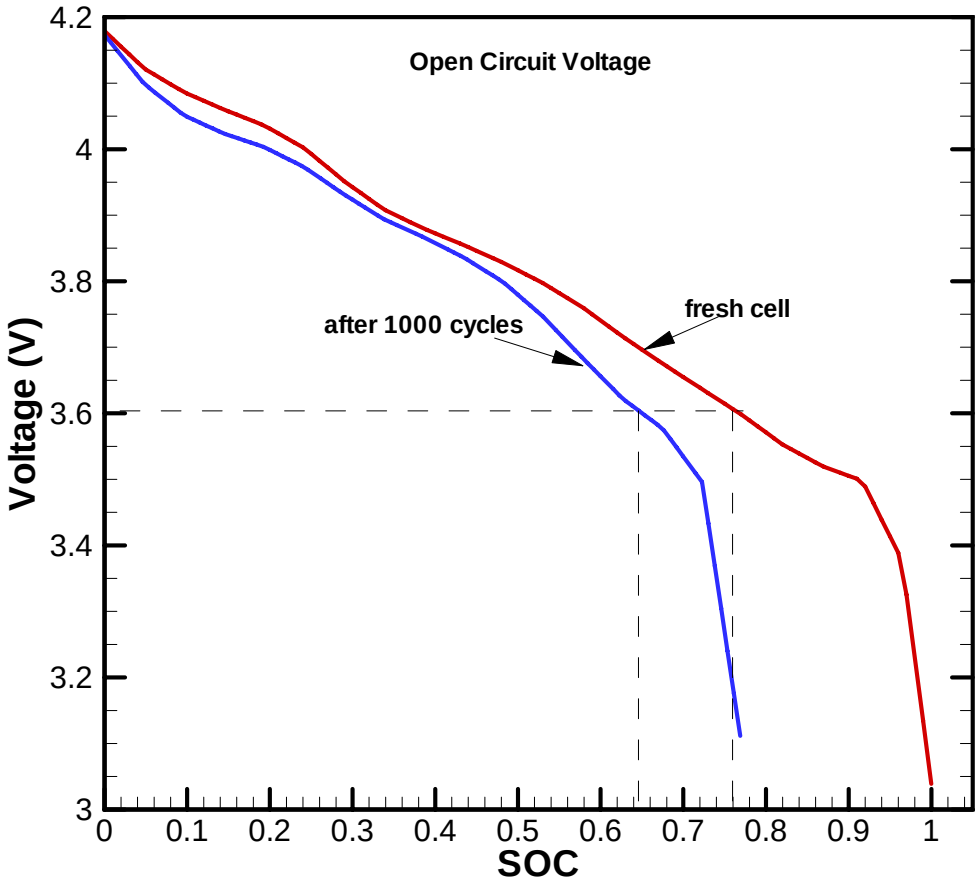

Figure 5.14: The measured open circuit voltage (the difference of the two electrode OCPs) of the fresh cell and cell after 1000 cycles. The SOC value is based on the fresh cell. For the same voltage at 3.6V, the SOC values of the two curves are quite different.

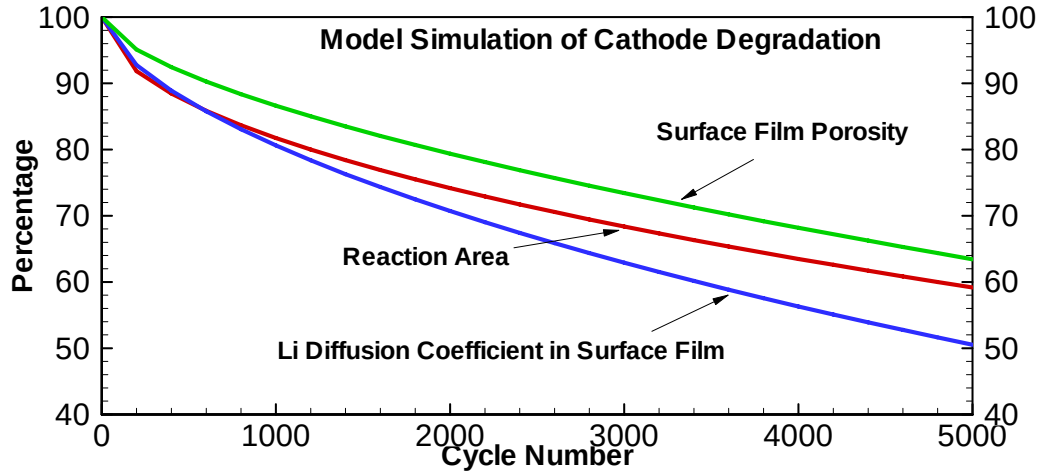

(a)

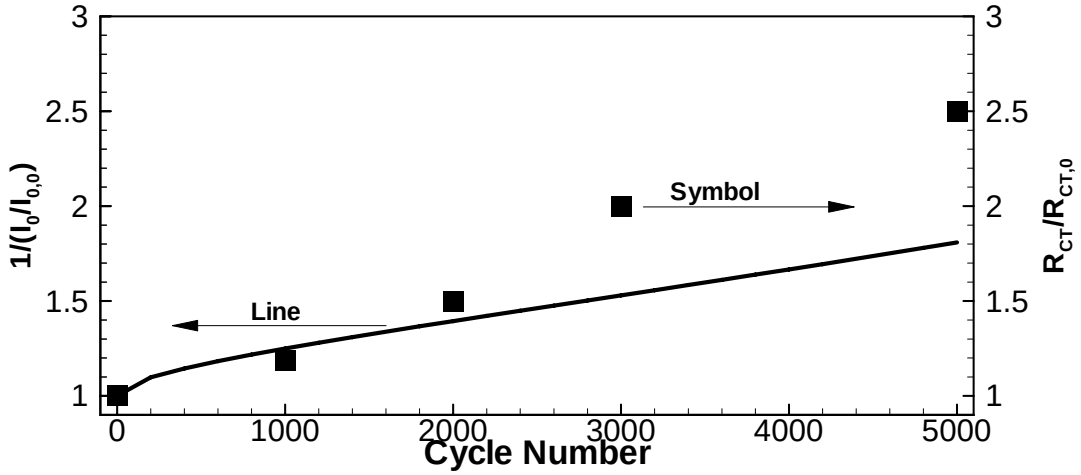

(b)

Figure 5.15: (a) Simulated result of the average surface film porosity, reaction area and Li diffusion coefficient in the surface film on the cathode with cycling. (b) Curve: model simulated of reciprocal of (the cathode exchange current divided by the initial value) and symbol: R_{CT} divided by the initial value (extracted form EIS data).

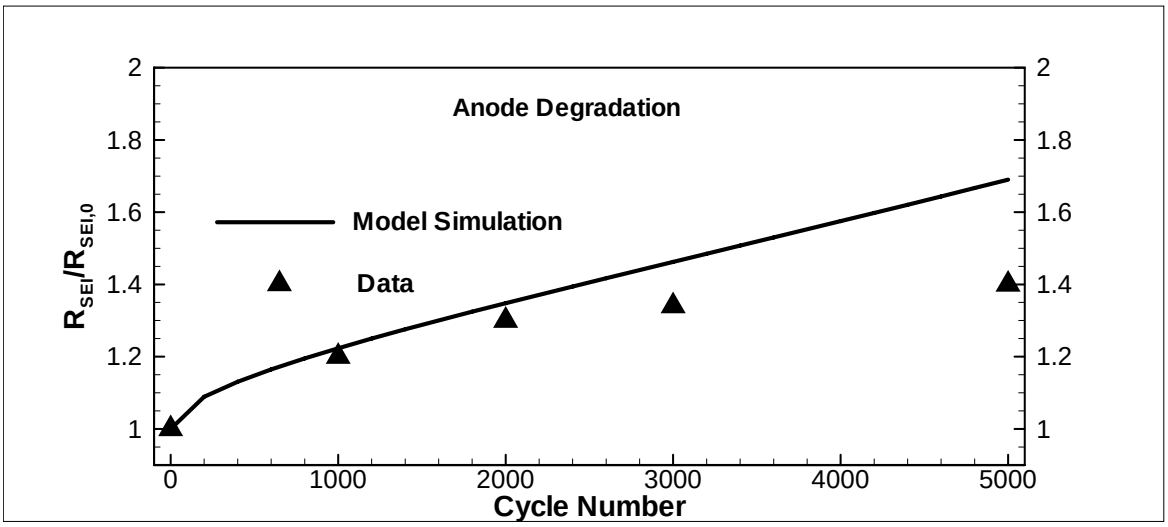

Figure 5.16: Simulated result of the average surface film resistance on the electrode with cycling. The symbols are extracted from experimental EIS data. The initial value is about 5mohm.

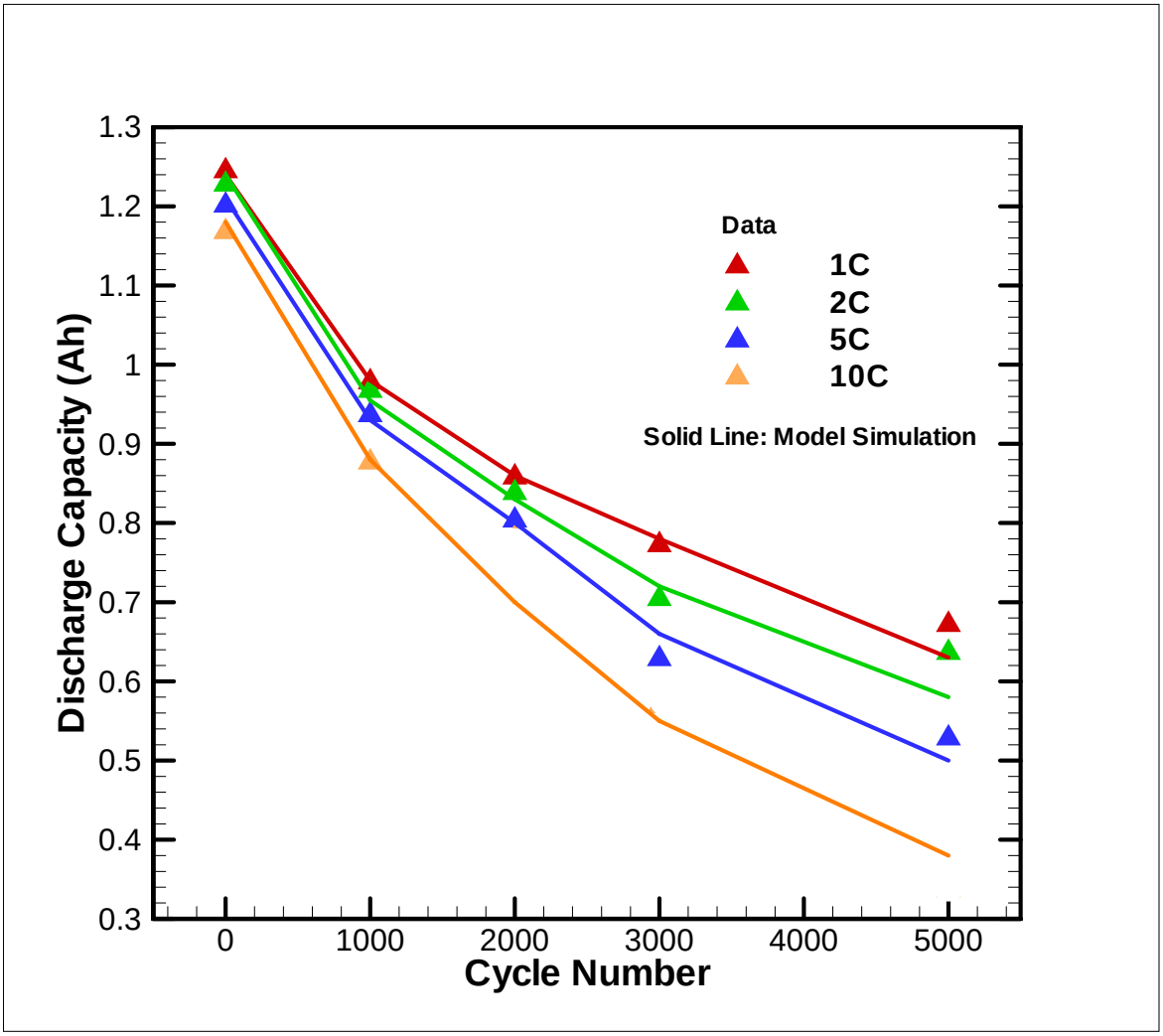

Figure 5.17: Discharge capacity at different C-rates for fresh and cycled cells. Both experimental data and simulated result are plotted. The discharge capacity obtained shows the decreased rate capability with cycling.

Chapter 6

Conclusions and Future Work

6.1 Conclusions

This dissertation introduces a general, electrochemical-thermal coupled model for not only a full cell, but also individual electrodes such that anode and cathode contributions to both performance and degradation can be separately delineated and predicted. In the present work, we:

1. Experimentally validate a fundamental electrochemical-thermal model (performance model) using constant and transient pulse current data at various temperatures.
2. Use the validated model to study lithium deposition on the negative electrode in overcharge or subzero temperature situations. Discuss the possible charge strategy under subzero temperature.
3. Extended the performance model to include degradation of a Li-ion battery due to surface film formation on both electrodes and use this degradation model to interpret the aging phenomena observed by the accompany experiment. (The experiment was carried out by Kwon.)

Efforts are made to validate both the performance model and degradation model with the experimental data. After that, an effort is made to fully utilize the models to explore the inside mechanism of several issues of concern, such as Li deposition on the negative carbon electrode and cell degradation. Some observations and suggestions from the model studies are,

1. Either low temperature or high charge rate may force Li insertion into the negative carbon electrode to occur in a narrow region near the separator. Therefore, Li deposition is mostly like to happen at this location. Either reducing the negative electrode particle size or improving the Li diffusion coefficient can reduce the chance of Li deposition.
2. Improving Li-ion cell by the heat generated inside the cell will reduce the chance of Li deposition during charging at subzero. A good charge protocol can be designed to obtain this goal.
3. For the Li-ion battery studied in the present work, aging on the positive electrode is the main reason that causes cell capacity loss and impedance rise during the accelerated aging test. During cycling, the positive electrode active material is lost and/or blocked from reaction which causes impedance rise and thus capacity fade by reducing the capability of the positive electrode to deliver and accept lithium.

6.2 Future Work

More work can be done to improve the charge protocol discussed in Chapter 4.2.2. Model simulation should be combined with experiments to obtain a more practical charge protocol.

Also, the degradation model studied in the present work is limited to a specific Li-ion battery with a specific set of aging mechanisms. Different aging mechanisms can be designed and studied with the degradation model. Normally, increasing cycling test temperature will increase the side reaction rate. Also, increasing the EOCV will increase the side reaction at the positive electrode and thus also increase the capacity loss.

Furthermore, the degradation can be used in a more practical application in HEV test. The following are some of the interesting parameters to be studied: SOH (state of health), DOD and EOCV.

SOH is defined as the ratio of full charge capacity of a cell to its rated or design capacity. For example, if the actual capacity of a fully charged aged cell is only 80% of its rated capacity, then the SOH of this cell is 80%.

DOD, introduced in the first chapter, is the inverse of SOC. An HEV battery is required to maintain at least 2000 cycles of deep discharges (80% DOD).

The effects of EOCV and DOD have been roughly studied in Ref.[66,67,68], however, they should be more carefully examined by considering more facts beside side reaction time, for instance, side reaction rates at the high EOCV and DOD.

Generally speaking, high EOCVs, excessive charge rates and extreme depth of discharges, as well as high operation temperatures all have a negative effect and shorten

the battery life. Thus, to explore the fundamental physics behind these phenomena in further work is meaningful and the suggestions based on the degradation model with degradation description in each electrode will then be much more specific and useful.

Bibliography

1. S. G. Chalk, J. F. Miller, “Key challenges and recent progress in batteries, fuel cells, and hydrogen storage for clean energy systems” *J. Power Sources*, 159, 73-80 (2006).

2. T. Miller, Advances in NiMH and Li-ion batteries for full hybrids, *Advanced Automotive Batteries Conference*, Baltimore, 2006.

3. *Lithium batteries- Science and technology*, G.- A. Nazri and G. Pistoia, Editors, *Kluwer Academic Publishers*, Norwell, Massachusetts, USA (2004).

4. M. Winter, J. O. Besenhard, M. E. Spahr, and P. Novak, “Insertion electrode materials for rechargeable lithium batteries” *Adv. Mater*., 10, 725-763 (1998).

5. A. M. Andersson, “Surface phenomena in Li-ion batteries”, PhD Thesis, Uppsala University, Sweden (2001).

6. D. Guyomard1 and J.M. Tarascon, "High voltage stable liquid electrolytes for $Li_{1+x}Mn_2O_4$/carbon rocking-chair lithium batteries" *J. Power Sources*, 54, 92-98 (1995).

7. D. Guyomard and J. M. Tarascon, "Rechargeable $Li_{1+x}Mn_2O_4$/carbon Cells with a new electrolyte composition potentiostatic studies and application to practical cells" *J. Electrochem. Soc*., 140, 3071-3081 (1993).

8. J. M. Tarascon and D. Guyomard, "New electrolyte compositions stable over the 0 to 5 V voltage range and compatible with $Li_{1+x}Mn_2O_4$/carbon Li-ion cells" *Solid State Ionics*, 69, 293-305 (1994).

9. Y. Ein-Eli, S. R. Thomas, V. Koch, D. Aurbach, B. Markovsky, and A. Schechter, "Ethylmethylcarbonate, a promising solvent for Li-ion rechargeable batteries" *J. Electrochem. Soc*. 143, L273 (1996).

10. Y. Ein-Eli, S. F. McDevitt, D. Aurbach, B. Markovsky, and A. Schechter, "Methyl Propyl Carbonate: A Promising Single Solvent for Li-Ion Battery Electrolytes" *J. Electrochem. Soc*. 144, L180 (1997).

11. U. Heider, R. Oesten and M. Jungnitz, "Challenge in manufacturing electrolyte solutions for lithium and lithium ion batteries quality control and minimizing contamination level" *J. Power Sources*, 81-82, 119-122 (1999).

12. P. Arora, R. White, and M. Doyle, “Capacity fade mechanisms and side reactions in lithium-ion batteries,” *J. Electrochem. Soc.*, 145, 3647-3667 (1998).

13. D. Aurbach, "Review of selected electrode–solution interactions which determine the performance of Li and Li ion batteries" *J. Power Sources*, 89, 206-218 (2000).

14. J. Vetter, P. Novák, M.R. Wagner, C. Veit, K.-C. Möllerb, J.O. Besenhard, M. Winter, M. Wohlfahrt-Mehrens, C. Vogler, and A. Hammouche, “Ageing mechanisms in lithium-ion batteries” *J. Power Sources,* 147, 269-281 (2005).

15. M. Wohlfahrt-Mehrens, C. Vogler, and J. Garche, “Aging mechanisms of lithium cathode materials” *J. Power Sources,* 127**,** 58–64 (2004).

16. A. N. Dey and B. P. Sullivan, "The electrochemical decomposition of propylene carbonate on graphite" *J. Electrochem. Soc*., 117, 222 (1970).

17. E. Peled and H. Straze, "The kinetics of the magnesium electrode in thionyl chloride solutions" *J. Electrochem. Soc*., 124, 1030-1035 (1977).

18. E. Peled, “The electrochemical behavior of alkali and alkaline earth metals in nonaqueous battery systems- the solid electrolyte interphase model” *J. Electrochem. Soc.*, 126, 2047 (1979).

19. A. Meitav and E. Peled, "Solid electrolyte interphase (SEI) electrode- II. The formation and properties of the SEI on magnesium in $SOCl_2$-$Mg(AlCl)_4)_2$ solutions" *J. Electrochem. Soc*., 128, 825-831 (1981).

20. E. Peled, “Film forming reaction at the lithium/electrolyte interface” *J. Power Sources,* 9, 253-266 (1983).

21. E. Peled, D. Golodnitsky, G. Ardel, and V. Eshkenazy, "The SEI model-application to lithium-polymer electrolyte batteries" *Electrochim. Acta*, 40, 2197-2204, (1995).

22. E. Peled, D. Golodnitsky, C. Menachem, and D. Bar-Tow, "An advanced tool for the selection of electrolyte components for rechargeable lithium batteries" *J. Electrochem. Soc*.,145, 3482-3486 (1998).

23. S. Mori, H. Asahina, H. Suzuki, A. Yonei, K. Yokoto, “Chemical properties of various organic electrolytes for lithium rechargeable batteries 1. Characterization of passivating layer formed on graphite in alkyl carbonate solutions” *J. Power Sources*, 68, 59-64 (1997).

24. R. Fong, U. von Sacken, and J. R. Dahn, "Studies of lithium intercalation into carbons using nonaqueous electrochemical cells" *J. Electrochem. Soc*., 137, 2009-2013 (1990)

25. S. -K. Jeong, M. Inaba, T. Abe, and Z. Ogumi, "Surface film formation on graphite negative electrode in lithium-ion batteries: AFM Study in an ethylene carbonate-based solution" *J. Electrochem. Soc*., 148, A989-A993 (2001).

26. Y. -C. Changa and H. -J. Sohnb, "Electrochemical impedance analysis for lithium ion intercalation into graphitized carbons" *J. Electrochem. Soc*., 147, 50-58 (2000).

27. D. Zhang, B. S. Haran, A. Durairajan, R. E. White, Y. Podrazhansky and B. N. Popov, "Studies on capacity fade of lithium-ion batteries" *J. Power Sources*, 91, 122-129 (2000).

28. X. Zhang, P. N. Ross, Jr., R. Kostecki, F. Kong, S. Sloop, J. B. Kerr, K. Striebel, E. J. Cairns, and F. McLarnon, "Diagnostic characterization of high power lithium-ion batteries for use in hybrid electric vehicles" *J. Electrochem. Soc*., 148, A463-A470 (2001).

29. C. Wang, A. J. Appleby, and F. E. Little, "Electrochemical impedance study of initial lithium ion intercalation into graphite powders" *Electrochim*. *Acta*, 46, 1793-1813 (2001).

30. I. Bloom, B.W. Cole, J.J. Sohn, S.A. Jones, E.G. Polzin, V.S. Battaglia, G.L. Henriksen, C. Motlock, and R. Richardson, "An accelerated calendar and cycle life study of Li-ion cells " *J. Power Sources*, 101, 238-247 (2001).

31. A.M. Andersson, K. Edström, and J.O. Thomas, "Characterisation of the ambient and elevated temperature performance of a graphite electrode" *J. Power Sources*, 81–82, 8-12 (1999).

32. G. Amatucci, A. du Pasquier, A. Blyr, T. Zheng, and J.M. Tarascon, "The elevated temperature performance of the $LiMn_2O_4$/C system: failure and solutions" *Electrochim. Acta,* 45, 255-271 (1999).

33. P. Ramadass, B. Haran, R. White, and B.N. Popov, "Capacity fade of Sony 18650 cells cycled at elevated temperatures- Part I. Cycling performance" *J. Power Sources*, 112, 606-613 (2002).

34. P. Ramadass, B. Haran, R. White, and B.N. Popov, "Capacity fade of Sony 18650 cells cycled at elevated temperatures- Part II. Capacity fade analysis" *J. Power Sources*, 112, 614-620 (2002).

35. M.N. Richard and J.R. Dahn, "Accelerating rate calorimetry study on the thermal stability of lithium intercalated graphite in electrolyte. I. Experimental" *J. Electrochem. Soc*., 146, 2068-2077 (1999).

36. H. Maleki, G. Deng, A. Anani, and J. Howard, "Comparison of the reactivity of various carbon electrode materials with electrolyte at elevated temperature" *J. Electrochem. Soc*., 146, 3224-3229 (1999).

37. P. Arora, M. Doyle, and R. E. White, "Mathematical modeling of the lithium deposition overcharge reaction in lithium-ion batteries using carbon-based negative electrodes" *J. Electrochem. Soc*., 146, 3543-3553 (1999).

38. Y. Ein-Eli, B. Markovsky, D. Aurbach, Y. Carmeli, H. Yamin, and S. Luski "The dependence of the performance of Li-C intercalation anodes for Li-ion secondary batteries on the electrolyte solution composition" *Electrochim. Acta*, 39, 2559-2569 (1994).

39. D. Aurbach, M. D. Levi, E. Levi, H. Teller, B. Markovsky, G. Salitra, U. Heider, and L. Heider, "Common electroanalytical behavior of Li intercalation processes into graphite and transition metal oxides" *J. Electrochem. Soc*., 145, 3024-3034 (1998).

40. D. Aurbach, K. Gamolsky, B. Markovsky, G. Salitra, Y. Gofer, U. Heider, R. Oesten, and M. Schmidt, "The study of surface phenomena related to electrochemical lithium intercalation into Li_xMO_y host materials (M = Ni, Mn)" *J. Electrochem. Soc*. 147, 1322-1331 (2000).

41. I. Bloom, S. A. Jones, E. G. Polzin, V. S. Battaglia, G. L. Henriksen, C. G. Motlock, R. B. Wright, R. G. Jungst, H. L. Case, and D. H. Doughty, "Mechanisms of impedance rise in high-power, lithium-ion cells" *J. Power Sources*, 111, 152-159 (2002).

42. I. Bloom, S. A. Jones, V. S. Battaglia, G. L. Henriksen, J. P. Christophersen, R. B. Wright, C. D. Ho, J. Belt, and C. G. Motloch, "Effect of cathode composition on capacity fade, impedance rise and power fade in high-power, lithium-ion cells" *J. Power Sources*, 124, 538-550 (2003).

43. D. P. Abraham, R. D. Twesten, M. Balasubramanian, I. Petrov, J. McBreen, and K. Amine, "Surface changes on $LiNi_{0.8}Co_{0.2}O_2$ particles during testing of high-power lithium-ion cells" *Electrochem. Commun.* 4, 620-625 (2002).

44. D. P. Abraham, R.D. Twesten, M. Balasubramanian, J. Kropf, D. Fischer, J. McBreen, I. Petrov, K. Amine, "Microscopy and spectroscopy of lithium nickel oxide-based particles used in high power lithium-ion cells," *J. Electrochem. Soc*., 150, A1450-1456 (2003).

45. D. P. Abraham, E. M. Reynolds, E. Sammann, A. N. Jansen, and D. W. Dees, "Aging characteristics of high-power lithium-ion cells with $LiNi_{0.8}Co_{0.15}Al_{0.05}O_2$ and $Li_{4/3}Ti_{5/3}O_4$ electrodes," *Electrochemica Acta*, 51, 502-510 (2005).

46. D. Dees, E. Gunen, D. Abraham, A. Jansen, J. Prakash, "Alternating current impedance electrochemical modeling of lithium-ion positive electrodes," *J. Electrochem. Soc*., 152, A1409-A1417 (2005).

47. M. Dubarrya, V. Svobodaa, R. Hwua, and B. Y. Liaw, "Capacity and power fading mechanism identification from a commercial cell evaluation" *J. Power Sources*, 165, 566-572 (2007).

48. Z. R. Zhang, H. S. Liu, Z. L. Gong, and Y. Yang, "Electrochemical performance and spectroscopic characterization of TiO_2-coated $LiNi_{0.8}Co_{0.2}O_2$ cathode materials," *J. Power Sources*, 129, 101-106 (2004).

49. J. R. Dahn, E. W. Fuller, M. Obrovac, and U. von Sacken, "Thermal stability of $LixCoO_2$, Li_xNiO_2 and λ-MnO_2 and consequences for the safety of Li-ion cells" *Solid State Ionics*, 69, 265 (1994).

50. H. Arai and Y. Sakurai, "Characteristics of Li_xNiO_2 obtained by chemical delithiation" *J. Power Sources*, 81-82, 401 (1999).

51. R. V. Chebiam, F. Prado, and A. Manthiram, "Structural instability of delithiated $Li_{1-x}Ni_{1-y}Co_yO_2$ cathodes" *J. Electrochem. Soc*., 148, A49 (2001).

52. K. K. Lee, W. S. Yoon, K. B. Kim, K. Y. Lee, and S. T. Hong, "A Study on the Thermal Behavior of Electrochemically Delithiated $Li_{1-x}NiO_2$" *J. Electrochem. Soc*., 148, A716 (2001).

53. S. S. Choi and A. Manthiram, "Factors influencing the layered to spinel-like phase transition in layered oxide cathodes" *J. Electrochem. Soc*., 149, A1157-A1163 (2002).

54. S. Jouanneau, D. D. MacNeil, Z. Lu, S. D. Beattie, G. Murphy, and J. R. Dahna, "Morphology and safety of $Li[Ni_xCo_{1-2x}Mn_x]O_2$ ($0 \le x \le 1/2$)" *J. Electrochem. Soc*., 150, A1299-A1304 (2003).

55. H. J. Bang, H. Joachin, H. Yang, K. Amine, and J. Prakash, "Contribution of the Structural Changes of $LiNi_{0.8}Co_{0.15}Al_{0.05}O_2$ Cathodes on the Exothermic Reactions in Li-Ion Cells" *J. Electrochem. Soc*., 153, A731-A737 (2006).

56. H. Lee, Y. Kim, Y.-S. Hong, Y. Kim, M. G. Kim, N.-S. Shin, and J. Cho, "Structural characterization of the surface-modified $Li_xNi_{0.9}Co_{0.1}O_2$ cathode materials by MPO_4 coating (M=Al, Ce, SrH, and Fe) for li-ion cells" *J. Electrochem. Soc*., 153, A781-A786 (2006).

57. J. Shim, R. Kostechi, T. Richardson, X. Song, K. A. Strebel, "Electrochemical analysis for cycle performance and capacity fading of a lithium-ion battery cycled at elevated temperature" *J. Power Sources*, 112, 222-230 (2002).

58. H. Yang and J. Parakash, "Determination of the reversible and irreversible heats of a $LiNi_{0.8}Co_{0.15}Al_{0.05}O_2$/Natural graphite cell using electrochemical-calorimetric technique" *J. Electrochem. Soc*., 151, A1222-A1229 (2004).

59. K. Kumai, H. Miyashiro, Y. Kobayashi, K. Takei, and R. Ishikawa, "Gas generation mechanism due to electrolyte decomposition in commercial lithium-ion cell" *J. Power Sources*, 81-82, 715-719 (1999).

60. D. Aurbach, B. Markousky, A. Shechter, Y. Ein-Eli, and J. Cohen, "A comparative study of synthetic graphite and Li electrodes in electrolyte solutions based on ethylene carbonate-dimethyl carbonate mixtures" *J. Electrochem. Soc*., 143, 3809-3820 (1996).

61. R. Yazami, Y. F. Reynier, "Mechanism of self-discharge in graphite-lithium anode" *Electrochim. Acta*, 47, 1217-1223 (2002).

62. R. Darling and J. Newman, "Modeling side reactions in composite $Li_yMn_2O_4$ electrodes" *J. Electrochem. Soc.*, 145, 990 (1998).

63. J. Christensen and J. Newman, "Effect of anode film resistance on the charge/discharge capacity of a lithium-ion battery" *J. Electrochem. Soc*., 150, A1416-A1420 (2003).

64. J. Christensen and J. Newman, "A mathematical model for the lithium-ion negative electrode solid electrolyte interphase" *J. Electrochem. Soc*., 151, A1977-A1988 (2004).

65. J. Christensen and J. Newman, "Cyclable lithium and capacity loss in Li-ion cells" *J. Electrochem. Soc*., 152, A818-A829 (2005).

66. P. Ramadass, B. Haran, P. M. Gomadam, R. E. White, and B. N. Popov, "Development of first principles capacity fade model for Li-ion cells" *J. Electrochem. Soc.*, 151, A196-A203 (2004).

67. G. Ning and B. N. Popov, "Cycle life modeling of lithium-ion batteries" *J. Electrochem. Society*, 151, A1584-A1591 (2004).

68. G. Ning, R. E. White, and B. N. Popov, "A generalized cycle life model of rechargeable Li-ion batteries" *Electrochim. Acta*, 51, 2012-2022 (2006).

69. R. Spotnitz, "Simulation of capacity fade in lithium-ion batteries" *J. Power Sources*, 113, 72-80 (2003).

70. G. Sikha, B. N. Popov, and R. E. White, "Effect of porosity on the capacity fade of a lithium-ion battery" *J. Electrochem. Soc.*, 151, A1104-A1114 (2004).

71. M. Broussely, S. Herreyre, P. Biensan, P. Kasztejna, K. Nechev, and R. J. Staniewicz, “Aging mechanism in Li ion cells and calendar life predictions” *J. Power Sources*, 97-98, 13-21 (2001).

72. R. G. Jungst, G. Nagasubramanian, H. L. Case, B. Y. Liaw, A. Urbina, T. L. Paez, and D. H. Doughty, "Accelerated calendar and pulse life analysis of lithium-ion cells" *J. Power Sources*. 119–121, 870-873 (2003).

73. B. Y. Liaw, E. P. Roth, R. G. Jungst, G. Nagasubramanian, H. L. Case, and D. H. Doughty, "Correlation of Arrhenius behaviors in power and capacity fades with cell impedance and heat generation in cylindrical lithium-ion cells" *J. Power Sources*. 119–121, 874-886 (2003).

74. P. Ramadass, B. Haran, R. E. White, and B. N. Popov, “Mathematical modeling of the capacity fade of Li-ion cells” *J. Power Sources*, 123, 230-240 (2003).

75. H. J. Ploehn, P. Ramadass, and R. E. White, “Solvent diffusion model for aging of litium-ion battery” *J. Electrochem. Soc.*, 151, A456-A462 (2004).

76. B. Y. Liaw, R. G. Jungst, G. Nagasubramanian, H. L. Case, and D. H. Doughty, “Modeling capacity fade in lithium-ion cells” *J. Power Sources*, 140, 157-161 (2005).

77. T. Yoshida, M. Takahashi, S. Morikawa, D. Ihara, H. Katsukawa, T. Shiratsuchi and J. Yamaki, “Degradation mechamism and life prediction of lithium-ion batteries” *J. Electrochem. Soc*., 153, A576-A582 (2006).

78. R. P. Ramasamy, J.-W Lee, and B. N. Popov, "Simulation of capacity loss in carbon electrode for lithium-ion cells during storage" *J. Power Sources*., 166, 266-272 (2007).

79. T. F. Fuller, M. Doyle, and J. Newman, “Simulation and optimization of the dual lithium ion insertion cell” *J. Electrochem. Soc.*, 141, 1-10 (1994).

80. M. Doyle, T. F. Fuller, and J. Newman, "Modeling of galvanostatic charge and discharge of the lithium/polymer/insertion cell" *J. Electrochem. Soc*., 140, 1526-1533 (1993).

81. C. Y. Wang, W. B. Gu and B. Y. Liaw, "Micro-macroscopic coupled modeling of batteries and fuel cells. Part I: Model development" *J. Electrochem. Soc*., 145, 3407-3417 (1998).

82. W. B. Gu and C. Y. Wang, "Thermal and electrochemical coupled modeling of a lithium-ion cell, in Lithium Batteries" *ECS Proceedings*, 99-25, 748-762, (2000).

83. W. B. Gu and C. Y. Wang, "Thermal-electrochemical modeling of battery systems" *J. Electrochem. Soc*., 147, 2910-2922, (2000).

84. D. Aurbach, M. D. Levi, E. Levi, and A. Schechter, "Failure and stabilization mechanisms of graphite electrodes" *J. Phys. Chem. B*, 101, 2195-2206 (1997).

85. Y. Wang, S. Nakamura, M. Ude, and P. B. Balbuena, "Theoretical studies to understand surface chemistry on carbon anodes for lithium-ion batteries: reduction mechanisms of ethylene carbonate" *J. Am. Chem. Soc*., 123, 11708-11718 (2001).

86. W. B. Gu, C. Y. Wang, and B. Y. Liaw, "Micro-macroscopic coupled modeling of battery and fuel cell systems. Part II: Application to Ni-Cd and Ni-MH cells" *J. Electrochem. Soc*., Vol.145, 3419-3427 (1998).

87. W. B. Gu, C. Y. Wang, J. Weidner, and R. Jungst, "Computational fluid dynamics modeling of a lithium/thionyl chloride battery with electrolyte flow" *J. Electrochem. Soc*., 147, 427-434, (2000).

88. W. B. Gu, G. Q. Wang, and C. Y. Wang, "Modeling the overcharge process of VRLA batteries" *J. Power Sources*, 108, 174-184, (2002).

89. K. Smith and C. Y. Wang, "Solid state diffusion limitations on pulse operation of a lithium ion cell for hybrid electric vehicles" *J. Power Sources*, 161, 628-639, (2006).

90. K. Smith and C. Y. Wang, "Power and thermal characterization of a lithium-ion battery pack for hybrid electric vehicles" *J. Power Sources*, 160, 662-673, (2006).

91. M. Doyle and J. Newman, "Comparison of modeling predictions with experimental data from plastic lithium ion cells" *J. Electrochem. Soc*., 143, 1890-1903 (1996).

92. V. Srinivasan and C.Y. Wang, "Analysis of electrochemical and thermal behavior of Li-ion cells", *J. Electrochem. Soc*., Vol.150, pp.A98-A106 (2003)

93. D. R. Bakera and M. W. Verbruggeb, "Temperature and current distribution in thin-film batteries" *J. Electrochem. Soc*., 146, 2413-2424 (1999).

94. J. Newman, K. E. Thomas, H. Hafezi, D. R. Wheeler, "Modeling of lithium-ion batteries" *J. Power Sources*, 119-121, 838-843 (2003).

95. R. Darling, J. Newman, "Modeling a Porous Intercalation Electrode with Two Characteristic Particle Sizes", *J. Electrochem Soc*., Vol. 144, pp. 4201-4208 (1997)

96. G. G. Botte, B. A. Johnson, and R. E. White, "Influence of some design variables on the thermal behavior of a lithium-ion cell" *J. Electrochem. Soc*., 146, 914-923 (1999).

97. C. Y. Wang, and V. Srinivasan, "Computational battery dynamics (CBD) - electrochemical/thermal coupled modeling and multi-scale modeling" *J. Power Sources*, 110, 364-376 (2002).

98. V. R. Subramanian, J. A. Ritter, and R. E. White, "Approximate solutions for galvanostatic discharge of spherical particles I. Constant diffusion coefficient" *J. Electrochem. Soc*., 148, E444-E449 (2001).

99. Y. Zhang and C.Y. Wang, "Cycle-life characterization of automotive Li-ion batteries with $LiNiO_2$ cathode", *J. Electrochem Soc*., Vol. 156, pp. A527-A535 (2009)

100. W.F. Fang, O.J. Kwon and C.Y. Wang, "Electrochemical-Thermal Modeling of Automotive Li-Ion Batteries and Experimental Validation Using A Three-Electrode Cell", *Int. J. Energy Res.* Vol. 34, pp 107-115 (2010)

101. O.J. Kwon and C.Y. Wang, "Diagnostics of automotive Li-ion batteries", *J. Power Sources*, to be submitted, (2010)

102. J. Fan and S. Tan, "Studies on Charging Lithium-Ion Cells at Low Temperatures", *J. Electrochem Soc*., Vol. 153, pp. A1081-A1092 (2006)

103. M. Jain, G. Nagasubramanian, R. G. Jungst, and J. W. Weidner, "Analysis of a lithium/thionyl chloride battery under moderate-rate discharge" *J. Electrochem. Soc*., 146, 4023-4030 (1999)

104. C. Ho, I.D. Raistrick, and R.A. Huggins, "Application of A-C Techniques to the Study of Lithium Diffusion in Tungsten Trioxide Thin Films", *J. Electrochem Soc*., Vol. 127, pp. 343-350 (1980)

Appendix A

Nomenclature

a_s	active surface area per electrode unit volume, cm^2/cm^3
A	electrode plate area, cm^2
c	concentration of lithium in a phase, mol/cm^3
C_{dl}	double layer capacitance, F/cm^2
D	diffusion coefficient of lithium species, cm^2/s
$E_{act,\Phi}$	activation energy, J/mol
F	Faraday's constant, 96,487 C/mol
I	applied current, A
i	current in solid phase or electrolyte, A/cm^2
$\bar{i}_n$	transfer current density of a reaction at the electrode/electrolyte interface, A/cm^2
i_o	exchange current density of an electrode reaction, A/cm^2
j	reaction current resulting in production or consumption of a species, A/cm^3
L	cell width, cm
l_s	diffusion length of lithium in solid phase, cm
q	heat generation rate, W
R	universal gas constant, 8.3143 J/mol K
R_f	film resistance on an electrode surface, $\Omega\ cm^2$
R_s	radius of solid active material particles, cm
R_{SEI}	solid/electrolyte interfacial flim resistance, $\Omega\ cm^2$
r	radial coordinate, cm
r_s	radius of solid particles, cm
T	absolute temperature, K
t	time, s

t_+^o	transference number of lithium ion with respect to the velocity of solvent
U	open-circuit potential of an electrode reaction, V
x	negative electrode solid phase stoichiometry
y	positive electrode solid phase stoichiometry

Greek symbol

α_a, α_c	anodic (cathodic) transfer coefficients for an electrode reaction
ε	volume fraction or porosity of a phase
η	surface overpotential of an electrode reaction, V
κ	conductivity of an electrolyte, S/cm
κ_D	diffusional conductivity of a species, A/cm
λ	thermal conductivity, W/cm K
ρ	density, Kg/cm^3
σ	conductivity of solid active materials in an electrode, S/cm
τ	Bruggeman tortuosity exponent
ϕ	ϕ volume-averaged electrical potential in a phase, V

Subscript

a, c	anode (cathode)
dl	capacitive double layer at solid/electrolyte interface
e	electrolyte phase
max	maximum value
s	solid phase
s,avg	average, or bulk solid phase
s,e	solid/electrolyte interface
sep	separator region
-, +	negative (positive) electrode region

Superscript

eff	effective value
Li	lithium species
s	side reaction

0	initial value

Appendix B

Acronyms and Abbreviations

BOL	beginning of the life
CC	constant current
CFD	computational fluid dynamics
CV	constant voltage
DEC	diethyl carbonate
DMC	dimethy carbonate
DOD	depth of discharge
EC	ethylene carbonate
EIS	electrochemical impedance spectroscopy
EMC	ethylmethyl carbonate
EOCV	end of charge voltage
GITT	galvanostatic intermittent titration technique
HEV	hybrid electric vehicle
HREM	high resolution electron microscopy
MPC	methyl propylene carbonate
Ni-Cd	nickel cadmium
Ni-MH	nickel/metal-hydride
OCP	open-circuit potential
PC	propylene carbonate
SEI	solid electrolyte interphase
SOC	state of charge
SOH	state of health

VITA

Weifeng Fang

Weifeng Fang received a Bachelor Degree in Mechanical Engineering in 2000 and a Master Degree in Mechanical Engineering in 2003, both at University of Science and Technology of China. He entered graduate school at the Pennsylvania State University in the fall of 2003 to pursue a doctoral degree in Mechanical Engineering.